GRAPHENE-LIKE MATERIALS FOR ELECTRONIC APPLICATIONS

A Thesis Submitted to
the Graduate School of
İzmir Institute of Technology
in Partial Fulfillment of the Requirements for the Degree of

MASTER OF SCIENCE

in Photonics Science and Engineering

by
Mehmet BAŞKURT

December 2020
İZMİR

ACKNOWLEDGMENTS

First of all, I would like to thank my supervisor Prof. Dr. Hasan Şahin for his guidance, support, and patience during my master's study.

I would like to thank my co-supervisor Assoc. Prof. Dr. Sinan Balcı for his support.

I would like to acknowledge and thank to the committee members of my thesis Assoc. Prof. Dr. Ümit Hakan Yıldız and Assoc. Prof. Dr. Engin Durgun for their time and participation.

I would like to thank my advisors and colleagues Fadıl İyikanat, Mehmet Yağmurcukardeş, and Melih Kuş for their guidance and help.

I would like to thank my friends Anılcan Kuş Necip Ayhan Tertemiz, Cansu Akyol, Cenk Omur, Dilce İnanç, Ezgi İnci, İbrahim Kaya, Mehmet Özcan, Meriç Güvenç, Metin Tan, Sema Sarısözen, Sercan Özen, Soner Karabacak, Yiğit Sözen, Tuğçe Arıca, Yenal Yalçınkaya, and Zeynep Kahraman.

I would like to thank my mother, brother, and my father for their support.

I would like to thank my dogs Şirin and Simba for being good dogs.

Most importantly, I would like to thank my wife Paulina Başkurt for her endless love and support.

This research was supported by TUBITAK with 117F095 project number.

ABSTRACT

GRAPHENE-LIKE MATERIALS FOR ELECTRONIC APPLICATIONS

Two-dimensional (2D) materials have gained vast interest in nanotechnology since these materials exhibit extraordinary properties due to electron confinement. Starting with graphene, many other 2D materials with characteristics of metals, semiconductors, insulators, and their magnetic analogues have been studied over the years. Insulators show importance as dielectric layers. Low dimensional metallic materials are used in electrical conduction. Ultra-thin semiconductors have variety of potential applications due to their characteristic band gap. Magnetic analogues of low dimensional materials are used in spintronics, offering high frequency, controllable switching. In addition, defects in these materials alter their physical properties and the concept can be adopted in order to use in different practices. Therefore it is important to study array of such materials and consider the alteration in their lattice theoretically and experimentally. In this thesis, first-principles calculations are used to predict insulating calcium halide single-layers are predicted, determine the effects of strain and V dopant in recently synthesized magnetic semiconducting VI_3 single-layers, propose synthesis of magnetic, semiconducting manganese fluorides from manganese dichalcogenides, investigate the affects of defects and simulate scanning tunneling microscopy images in order to compare with experimental results, and finally to determine rather the detection of volatile organic compounds (VOC) such as methanol and ethanol by graphene-based sensors is feasible or not. Experiments are carried out to construct and further investigate the mechanism of VOC detection and working, highly sensitive alcohol sensors.

ÖZET

ELECTRONİK UYGULAMALARI İÇİN GRAFEN BENZERİ MALZEMELER

İki boyutlu (2B) malzemeler, electronların hapsolması sonucu olağanüstü sonuçlar sergilemesinden dolayı nanoteknolojide büyük ilgi görmüştür. Grafen ile başlayarak, diğer metal, yarı-iletken, yalıtkan ve bunların manyetik analogları olan diğer 2B malzemeler yıllardır çalışılmaktadır. Yalıtkan malzemeler dielektrik tabakalar olarak önem göstermektedir. Düşük boyutlu metalik malzemeler elektrik iletiminde kullanılır. Ultra-ince yarı-iletkenlerin, karakteristik band aralıkları nedeniyle farklı uygulamalarda potansiyel uygulamaları mevcuttur. Düşük boyutlu malzemelerin manyetik analogları spintronikte kullanılır ve yüksek frekanslı, kontrol edilebilir anahtarlama sunar. Bunlara ek olarak, bu malzemelerdeki kusurlar fiziksel özelliklerini değiştirmekte ve bu konsept farklı uygulamalarda kullanılmak benimsenebilmektedir. Bu nedenle, bu tür malzemeler dizisini incelemek ve yapılarındaki değişimi teorik ve deneysel olarak değerlendirmek önemlidir. Bu tezde, ilk-prensip hesaplamaları kullanılarak yalıtkan kalsiyum halojenürlerin tek-tabakalı yapıları öngörülmesi; manyetik yarı-iletken VI_3 tek-tabakalı yapılarında gerilim uygulayarak ve V katkısı yapılarak etkileri incelenmesi; ultra-ince manyetik yarı-iletken mangan florürlerin 2B mangan dikalkojenürler kullanılarak sentezlenmesi; kusurların etkilerini incelemek ve taramalı tünelleme mikroskobu resimlerini simüle ederek deneysel verilerle karşılaştırılması; ve son olarak da metanol ve etanol gibi uçucu organik bileşiklerin (UOB) grafen-bazlı sensörler kullanılarak tayin edilmesi gerçekleştirilmiştir. Deneysel olarak da, UOB tayininde kullanılmak ve tayin mekanızmasını incelemek üzere çalışan, yüksek hassaslıkta cihaz geliştirilmiştir.

... to Paulina Başkurt ...

TABLE OF CONTENTS

LIST OF FIGURES

Figure **Page**

Figure **Page**

Figure **Page**

LIST OF TABLES

Table **Page**

CHAPTER 1

INTRODUCTION

Advancing technology and improvements in the performance of everyday use devices such as smartphones, computers are result of developments in the materials that used in electronic circuit components such as transistors. In the last decade, the reason for the rapid increase in the performance of these devices is the applications of low-dimensional materials in the circuit elements. Thinning down materials to the two-dimensional (2D) limit decreases the dimensions of electron propagation and results in electron confinement which reveals significant physical properties. Remarkable properties of 2D materials became a hot topic with the successful isolation of atomically thin graphene films.[1,2] With its structure constructed of sp^2 hybridized C–C bonds, graphene is a strong, durable material under strong strain and deformation forces with significant mechanical properties.[3] Thermal conductivity is reported to be high as 3000 WmK^{-1}.[4] Graphene has high electron mobility of ∼10000 $cm^2V^{-1}s^{-1}$ at room temperature, which can be induced by gate voltage.[1] Encapsulation by h-BN reveals ballistic transport characteristic of graphene.[5] Due to its extraordinary properties, graphene is used in wide scope of applications. It is reported that graphene has been widely used in photonics, plasmonics and broadband optoelectronic devices due to its unique properties.[6] Enhance responsivity is observed in graphene based photodetectors.[7] Adaptive thermal camouflage is achieved by a graphene based devices.[8,9]

Although graphene shows unique properties and used in numerous applications, having zero band gap limits the possible applications of graphene. In order to overcome this problem, many other 2D materials have been investigated. Few-atom-thick metals,[10] semiconductors,[11,12] insulators,[13,14] and their magnetic analogues[15,16,17,18,19,20] are reported and have been extensively studied. MoS_2 is one of the most common used 2D material other than graphene, first reported by Mak *et al.*.[21] An interesting property of MoS_2 is that having indirect band gap in bulk and few layer form, however becoming a direct band gap semiconductor in single-layer form. In-direct to direct transition of band gap allows strong photoluminescence.[22] Single-layer MoS_2 has been used in various applications. Ultrasensitive photodetectors engineered using MoS_2 single-layers.[23] Employing MoS_2 in transistor architecture is resulted with transistors operating at gigahertz frequencies.[24] Therefore MoS_2 single-layers have high potential in nanotechnological applications. Additionally, MoS_2 is reported to have high yield as a catalytic surface. High performance hydrogen evolution reactions are reported at the grain boundaries engineered in MoS_2 lattice.[25] Nitrogen reduction is accomplished and successful synthesis of ammonia by MoS_2 used as a catalyst.[26] Sensor applications of MoS_2 also gained interest due to performance of MoS_2 single-layers in various fields of studies. MoS_2 field effect transistor (FET) based biosensors allow rapid detection of biomolecules at low concentrations, allowing ultrasensitive, scalable, flexible, low-cost sensors.[27] Farimani *et al.* reported that engineering nanopores in MoS_2 surface allows DNA based detection and sequencing.[28] Vapor sensors of MoS_2 based sensors also show high selectivity and low concentration sensing of volatile organic compounds.[29] NO_2 and NH_3 sensing of MoS_2 sensors are also reported to show excelent selectivity, recovery and ability to be adjusted by applying a bias voltage.[30] In addition to MoS_2 there are many other ultrathin crystals, i.e. $MoSe_2$, WS_2, WSe_2, ReS_2, $TaSe_2$, h-BN, CrI_3, silicene, and germanene. Among these, transition metal chalcogenides have similar properties as MoS_2, and reported to be used as photodetectors, in transistor design, as catalysts, and sensor architectures.[31,32,33,34,35,36,37,38,39,40,41,42,43] Surface functionalization of such ultra-thin materials are reported to gain new capabilities, or enhance the properties of pristine crystals. Xu *et al.* reports that functionalization of MoS_2 with thiols increase the dopamine sensitivity.[44] Ti functionalized ZrP nanosheets are used in photocatalytic applications.[45] Functionalization of h-BN is reported to increase its water solubility, biocompability, increase processibility which increases the potential applications in many areas such as biomedical, electronic, environmental, and green energy sources.[46] Moreover, heterostructures of ultrathin crystals gain adjust the properties of the devices, therefore heterojuctions have been widely studied. Katoch *et al.* reports that in the heterostructures of h-BN and WS_2 single-layers results with renormalizing in spin-orbit splitting which points out to the tunability of electronic, spintronic properties in other TMD/h-BN heterostructures.[47] As a outcome of heterostructures of WS_2 with MoS_2 charge transfer rate and photocurrent generation are increased remarkably.[48] Employing an ultrathin magnetic material CrI_3 in heterostructure with WSe_2, spin valley state of localized holes are prepared using the advantage of spin selectivity of CrI_3.[49] Number of studies increase every passing day in prediction and synthesis of novel ultra-thin materials, functionalized single-layer crystals, and heterostructures of these materials.

2D materials are widely used in sensor applications due to their high surface area to volume ratio which offers high sensitivity. It is reported that ultra-thin materials can sense molecules as low as ppb concentrations. Sensing abilities related structures of graphene-like 2D materials are discussed in the previous paragraph. Additionaly, sensing abilities of graphene are also used number of studies. Pristine graphene is used in molecular sensing applications in order to determine the concentration of NO_2, NH_3, and various volatile organic compounds (VOCs) as well as pH, and temperature sensing applications.[50,51,52,53,54] It is demonstrated that post-processing data collected from graphene response to the analytes is an important part for the selectivity of the sensor. Rumyantsev *et al.* reported selective gas sensing with a graphene based sensor that seperates the signal according to the frequency of noise caused by the analyte.[55] This graphene based sensor is used to differentiate between acetonitrile, chloroform, ethanol, methanol, open air, and tetrahydrofuran species succesfully. Nallon *et al.* reported another pristine graphene based sensor and the response to various compounds are investigated by performing principle component analysis (PCA), and 11 chemically diverse , 9 mono-substituted benzene compounds are selectively detected with the accuracy of 96% and 92%, respectively.[56] Although the data processing is important to discriminate the response between species, sensing mechanism must to be understood. There are different approaches to the mechanism of sensing via graphene based sensors. In many studies it is stated that current or resistance change is due to the charge transfer between the molecules and graphene surface.[57] Some studies aim to increase charge transfer, therefore there are reports of metal functionalized graphene surfaces in sensor applications increasing the response.[58] However, theoretical calculations reveal that analyte molecules interact with graphene surface with low energies. Such low interaction energies are only van der Waals type interactions therefore charge transfer does not occur. Similar study by Bauschlicher *et al.* reports that charge transfer between NH_3 and carbon nanotube structures which are constructed of sp^2 hybridized carbon atoms is negligibly small, therefore current increase cannot be explained by charge transfer as it is one of the widely proposed mechanisms in the literature.[59] Our calculations on graphene and VOCs also show that charge transfer is negligibly small. Another approach is that adsorbed species change the quantum capacitance of the system, therefore, current is modified.[60,61] This approach fits better to the theoretical results. Measurements of quantum capacitance of graphene reveals effects of impurities or density inhomogenities on graphene surfaces and the capacitance.[62] These impurities can be caused by weak interactions between graphene and external molecules, and results in electron/hole puddles.[63] As result, capacitance of graphene is modified according to the interacting specie and postprocess of the response data will enable selectivity of the sensor.

This thesis constructed as follows; in Chapter 2 computational and experimental methodologies are discussed within sections 2.1 and 2.2, respectively. In Chapter 3, stable single-layers of CaF_2 are investigated. Following that, other calcium halide structures are discussed in Chapter 4. In Chapter 5 modulation of magnetic properties of VI_3 single-layers depending on the V dopant and biaxial strain is examined. Formation of non-layered coordination varied MnF_2 and MnF_3 crystals via fluorination of manganese dichalcogenides are given in Chapter 6. Prevalence of different types of defects in ReS_2 lattice and determination of their affects via collaborated scanning tunneling microscopy analysis and simulation is carried out in Chapter 7 In Chapter 8, graphene based gas sensors are investigated both theoretically and experimentally. Finally, results are concluded in Chapter 9.

CHAPTER 2

METHODOLOGY

2.1. Computational Methodology

Quantum mechanical wave function of a physical system contains information of the system dynamics. In order to obtain this information is done simply by solving the Schrödinger equation if it is a non-relativistic system. However, when interacting many-body problems are considered, this is an highly challenging procedure. In order to reduce the computational cost and effort, there are different methods. One of the most common used method is the Density Functional Theory (DFT). DFT offers high efficiency in determining structural, vibrational, electronic, magnetic, mechanical properties of a many-electron systems.

Physical system can be mathematically illustrated by the Schrödinger equation;

$$\hat{H}\Psi = E\Psi \tag{2.1}$$

where $\hat{H}$ is the Hamiltonian operator which is the energy operator, Ψ is the wave function, and E is the energy eigenvalue corresponding to the Hamiltonian operator. The eigenfunctions of the Hamiltonian operator is Ψ, which is the solution to the Schrödinger equation. In hydrogen-like systems solving the Schrödinger equation is easy, however for interacting N-body systems Hamiltonian becomes;

$$\hat{H} = \hat{T_n} + \hat{T_e} + \hat{V_{ne}} + \hat{V_{ee}} + \hat{V_{nn}} \tag{2.2}$$

where $\hat{T_n}$ and $\hat{T_e}$ are the kinetic energies of nuclei and electrons, respectively, $\hat{V_{ne}}$ is the attractive potential between nuclei and electrons,$\hat{V_{ee}}$ repulsive potential between electrons, and $\hat{V_{nn}}$ is the repulsive potential between nuclei. Therefore, the Hamiltonian of such system is;

$$\hat{H} = -\frac{1}{2}\sum_{j}^{M}\frac{1}{m_j}\nabla_j^2 - \frac{1}{2}\sum_{i}^{N}\nabla_i^2 - \sum_{i}^{N}\sum_{I}^{M}\frac{Z_j}{|\mathbf{r_i} - \mathbf{R_j}|} + \sum_{i}^{N}\sum_{j>i}^{N}\frac{1}{|\mathbf{r_i} - \mathbf{r_j}|} + \sum_{i}^{M}\sum_{j>i}^{M}\frac{Z_i Z_j}{|\mathbf{R_i} - \mathbf{R_j}|} \tag{2.3}$$

where m_j and Z_j are the mass and atomic number of nucleus j, ∇ is the Laplacian operator, N and M are the number of electrons and nuclei in the system, r_i and R_j are the coordinates of electron i and nucleus j, respectively. As displayed, N-body system is complex, and computationally expensive. In order to reduce the computational cost in solving such systems, certain approximations are required. Born-Oppenheimer approximation simplifies the system through a simple assumption where nuclei is treated as static with respect to electrons.[64] This assumption eliminates the first and the fifth terms in the Eq. 2.3. Remaining equation is refered as the electronic Hamiltonian;

$$\hat{H} = -\frac{1}{2}\sum_{i}^{N}\nabla_i^2 - \sum_{i}^{N}\sum_{I}^{M}\frac{Z_j}{|\mathbf{r_i} - \mathbf{R_j}|} + \sum_{i}^{N}\sum_{j>i}^{N}\frac{1}{|\mathbf{r_i} - \mathbf{r_j}|}. \tag{2.4}$$

Although the computational effort is greatly reduced, electron-electron interaction term in the Eq. 2.7 brings 3^N variables. This problem was attempted to be solved by Hartree approximation[65] which proposes taking the potential of electron-electron interactions can be taken as density of electrons. However, this approximation does not obey the Pauli exclusion principle. Later on, Hartree-Fock approximation[66] fixes this issue by approximating the electronic wave function by Slater-determinant, therefore reducing many-body problem into single-particle problem. Hartree-Fock approximation fails the include correlation potential, which is the interaction between electrons of like-spin.

Another approximation is Thomas-Fermi approximation[67,68] assumes that kinetic energy of the electrons can be treated as functional of the electron density. Writing the kinetic energy term as a functional of electron density give the equation;

$$T[n] = C_F \int n^{5/3}(r)dr \tag{2.5}$$

where C_F is the Fermi coefficient and $n(r)$ is the electron density. Including electron-nucleus and electron-electron interaction terms makes the total energy of the system;

$$T[n] = C_F \int n^{5/3}(r)dr - Z\int \frac{n(r)}{r}dr + \frac{1}{2}\int\int \frac{n(r_1)n(r_2)dr_1dr_2}{|r_1 - r_2|}. \tag{2.6}$$

Minimizing the Eq. 2.6 gives the ground state energye of the system;

$$N = \int n(r)d^3r. \tag{2.7}$$

Although Thomas-Fermi model simplifies the system in terms of electron density but neglects the exchange and correlation effects, it displays the efficiency of including electron density instead of interacting electrons. This concept is vital in the density functional theory.

2.1.1. Density Functional Theory

Density functional theory is a widely used computational method in order to determine properties of molecules, polymers, crystals, and the intermolecular interactions between these species. It allows one to determine structural, electronic, vibrational and mechanical properties. In addition, thermal and optical properties are reported to be calculated using DFT. In the DFT, functional of non-interacting ground state electron density is considered instead of interacting many-electron systems. Although the accuracy of the system decreases, computational efficiency is greatly increased. DFT is based on the Hohenberg-Kohn theorems.[69]

2.1.1.1. Hohenberg-Kohn Theorems

Hohenberg and Kohn stated that ground state of a quantum many-body system can be expressed in functional of electron density. Hohenberg-Kohn theorems represented in main theorems. In the first theorem external potential, $V_{ext}(r)$ is in correspondence with the functional of the electron density $n(r)$. In the second theorem, energy of the system can be determined employing the electron density functional. The exact ground state density, $n_0(r)$, minimizes the total energy of the system. Expectation value of the Hamiltonian in terms of ground state wave function gives the ground state energy;

$$E_{HK}[n] = \frac{\langle \Psi_0 |H| \Psi_0 \rangle}{\langle \Psi_0 | \Psi_0 \rangle} \equiv \langle H \rangle = \langle T \rangle + \int d^3\mathbf{r} V_{ext}(\mathbf{r}) n_0(\mathbf{r}) + \langle V_{int} \rangle + E_{II} \tag{2.8}$$

where E_{II} is the interaction energy of the nuclei.

2.1.1.2. Hellman-Feynman Theorem

Hellman-Feynman theorem is an essential in DFT. It indicates that charge density of electron exchange and correlation and the kinetic energy can be used to write the force on a nucleus. Structural optimization can be accomplished by this theorem. Force on nucleus is indicated as;

$$\mathbf{F}_I = -\frac{\partial E}{\partial \mathbf{R}_I}. \tag{2.9}$$

Total energy can be obtained from the Eq. 2.8 and the force on nucleus is illustrated as;

$$\mathbf{F}_I = -\int d^3\mathbf{r} n(\mathbf{r}) \frac{\partial V_{ext}(\mathbf{r})}{\partial \mathbf{R}_I} - \frac{\partial E_{II}}{\partial \mathbf{R}_I}. \tag{2.10}$$

2.1.1.3. Kohn-Sham Equations

Kohn-Sham equations are based on the Hohenberg-Kohn theorem. It is stated that varying the charge density over all densities containing N electrons, energy functional can be minimized. The energy functional takes the form;

$$E[n] = \int n(r)V_{ext}(r)dr + F_{HK}[n] = \int n(r)V_{ext}(r)dr + T[n] + E^{Hartree}[n] + E_{xc}[n] \tag{2.11}$$

where F_{HK} is the universal functional, $T[n]$ is the sum of kinetic energy of non-interacting electrons, $E^{Hartree}[n]$ is the Hartree energy, $E_{xc}[n]$ is the exchange and correlation energy. Effective potential is defined as follows;

$$V^{eff} = \frac{\delta\{\int n(r)V_{ext}(r)dr + E^{Hartree}[n] + E_{xc}[n]\}}{\delta n(r)}. \tag{2.12}$$

Effective potential equation can be reduced to;

$$V^{eff} = V_{ext}(r) + \int \frac{n(r')}{|r - r'|} dr' + V_{xc}(r) \tag{2.13}$$

where $V_{xc}(r)$ is the exchange-correlation potential. Using this form of effective potential, Kohn-Sham DFT Schrödinger equation takes the form of one-electron like system which results in the electron density;

$$\left[-\frac{1}{2}\nabla^2 + V^{eff}\right] \phi_i = E_i \phi_i \tag{2.14}$$

where ϕ_i are the Kohn-Sham one-electron orbitals eigenfunctions. Electron density is determined from the Eq. 2.14, given as;

$$n(r) = \sum_{i=1}^{N} |\phi_i|^2. \tag{2.15}$$

The effective potential, V^{eff}, depends on the density $n(r)$. In order to solve the Kohn-Sham equation, initial guess of electron density is taken, the corresponding effective potential (V^{eff}) constructed, the Kohn-Sham orbitals (ϕ_i) are calculated, new electron density is calculated by these orbitals and compared to the initial electron density. Once this self-convergent process reach convergence, final electron density can be used to calculate the total energy. Although the final electron density is determined, exchange-correlation energy is still unknown.

2.1.1.4. Exchange-Correlation Functionals

Kohn-Sham equations are used to determine the final electron density of a system which can be employed to calculate the total energy. However, exchange-correlation energy is absent. In order to complete the Kohn-sham equation, E_{xc} should be known. There are approximations in order to calculate the exchange-correlation energy. These functionals are widely used in DFT.

Local Density Approximation (LDA):

In the local density approximation, the system is divided into volumes that contains constant electron density. Exchange-correlation energy by LDA;

$$E_{xc}^{LDA}[n] = \int n(r)\epsilon_{xc}^{unif}[n]dr \tag{2.16}$$

where ϵ_{xc}^{unif} is the exchange-correlation energy per electron.[70] For systems such as metals where the electron density varies slowly LDA functional is efficient. However, in general, lattice dimensions are underestimated while the cohesive energies are overestimated.

Generalized Gradient Approximation (GGA):

In the generalized gradient approximation, in addition to the electron densities are not constant in each division, in fact vary with a gradient. Mathematical illustration of the exchange-correlation energy by GGA;

$$E_{xc}^{GGA}[n] = \int f^{GGA}(n(r), \nabla n(r))dr \tag{2.17}$$

where $\nabla n(r)$ is the gradient of the electron density.[71] In contrast to LDA, GGA works well with systems that has rapidly varying electron densities. GGA functionals can yield results with higher accuracy in comparison to LDA.

Hybrid Functionals:

In addition to LDA and GGA, hybrid functional are also widely used to obtain exchange-correlation energy. These are constructed as linear combinations of other reported exchange-correlation functionals. Indicated in various studies, obtaining results closer to the experimental results can be achieved by using hybrid functionals. One of the widely used hybrid functionals is HSE,[72] which is illustrated as;

$$E_{xc}^{HSE} = aE_x^{HF,SR}(\omega) + (1-a)E_x^{PBE,SR}(\omega) + E_x^{PBE,LR}(w) + E_c^{PBE} \tag{2.18}$$

where $E_x^{HF,SR}$ is the short range Hartree-Fock exchange, $E_x^{PBE,SR}$ and $E_x^{PBE,LR}$ are the short and long range components of PBE exhange functional, and E_c^{PBE} is the PBE correlation energy. a and ω varies according to the HSE functional. For HSE06, a and ω are reported as 1/4 and 0.2, respectively.[72]

2.1.2. Computing Phonons

Quantum mechanical description of lattice vibration is called phonon. Vibrational properties of materials can be determined by their phonon band dispersions through Brillouin zone. Atoms in matter are theorized to to be vibrating around a certain equilibrium position, obeying the Hooke's law. As in a simple spring, displacements of atoms will result in with restoring forces to the equilibrium position and these oscillations will obey Hooke's law;

$$F = -kx \tag{2.19}$$

where k is the spring constant, and x is the distance between atom and equilibrium position. In this section, methodology of phonon band dispersion calculations in DFT is discussed.

In DFT, calculations are done at absolute zero (0 K), therefore vibrations are not indicated in the solution. However, as mentioned above, displacement of an atom from its equilibrium position will result with a restoring force which can be determined. This method is called the small displacement method. Force constant matrix is gathered by displacement of an atom trace amount in a super cell that is sufficiently large. Number of displaced atoms can vary according to the symmetry of the system. Hellman-Feynman forces are calculated for each displacement. Force matrix is constructed. Potential energy of a crystal in low temperatures is given by equation;

$$U_{harm} = E_{eq} + \frac{1}{2} \sum_{ls\alpha, l't\beta} \Phi_{ls\alpha, l't\beta} u_{ls\alpha} u_{l't\beta}, \tag{2.20}$$

where E_{eq} is the total energy of the crystal at equilibrium positions, u_{ls} is the displacement of atom s in unit cell l, α, and β denotes the direction of the displacement in cartesian coordinates, $\Phi_{ls\alpha,l't\beta}$ is the force constant matrix. Differentiation of the harmonic energy in Eq. 2.20 relation between the forces and the displacements can be deduced. The Relation is linear, as F_{lsa} is found to be;

$$F_{ls\alpha} = -\sum_{l't\beta} \Phi_{ls\alpha, l't\beta} u_{l't\beta}. \tag{2.21}$$

Using the Eq. 2.26 for the force constant matrix, dynamical matrix can be defined as;

$$D_{s\alpha,t\beta} = \frac{1}{\sqrt{M_s M_t}} \sum_{l} e^{i\mathbf{q}(R_{l't\beta}-R_{ls\alpha})} \Phi_{ls\alpha,l't\beta}, \tag{2.22}$$

where M_s is the mass of s^{th} atom, M_t is the mass of t^{th} atom, $R_{l't\beta} - R_{ls\alpha}$ is the distortion of the atoms. Once the dynamical matrix is determined, eigenvalues can be calculated, which give the phonon frequencies of each phonon branch. Total number of phonon branches is given by the total number of degrees or freedom of a crystal, which is $3N$ in a system constructed of N atoms in the primitive cell. Among these, 3 branches are acoustical, and $3N-3$ are optical. Acoustical and optical branches describe in-phase and out-of-phase motions of atoms, respectively. In this thesis, phonon band dispersions are calculated by small displacement method using PHON[73] and phonopy[74] codes. In Figure 2.1 phonon dispersions of h-BN are presented. Additionally, corresponding vibrational modes are displayed.

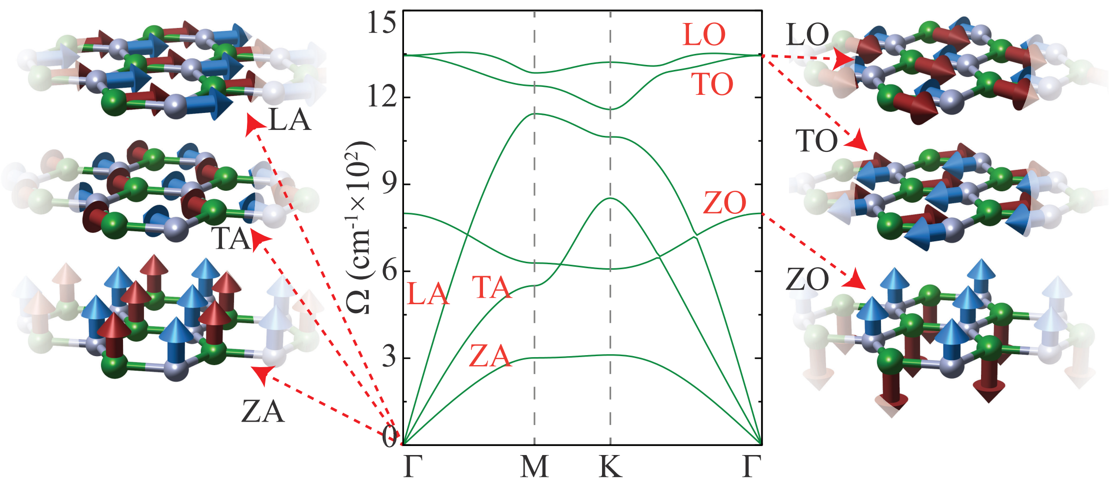

Figure 2.1. Phonon band dispersions and corresponding vibrational modes of h-BN.

2.1.3. Calculating Mechanical Properties

Linear-elastic properties of materials such as in-plane stiffness and Poisson ratio can be calculated using first-principles calculations. In-plane stiffness demonstrates the rigidity of a material, and it is represented as C_x and C_y. While $C_x = C_y$ in isotropic structures, in isotropic structures these values may vary. On the other hand, Poisson ratio gives the ratio of transverse contraction strain to longitudinal extension, and represented as ν_x and ν_y. In order to determine the elastic properties of materials, elastic strain tensor elements C_{ij} are calculated using the equation;

$$C_{x(y)} = \frac{(C_{11}C_{22} - C_{12} \times C_{21})}{C_{22(11)}}, \tag{2.23}$$

$$\nu_{x(y)} = \frac{C_{12}}{C_{22(11)}}. \tag{2.24}$$

2.1.4. Simulating Scanning Tunneling Microscopy Images

Scanning tunneling microscopy (STM) is a method that is used to examine the topology of materials. It is invented in 1981 by the IBM scientists, Gerd Binning and Heinrich Rohrer, which won Nobel Prize in Physics in 1986.[75,76] STM works by collecting information of vacuum tunneling currents for a given bias voltage, for each pixel point in an XY-plane, and postprocessing the collected information afterwards in order to generate an image. STM is widely used to analyze topography of pristine 2D materials, defect formation, edges of ultra-thin crystals.

Simulated STM images can be generated by postprocessing partial charge densities calculated by DFT results (see Figure 2.2). Since the tunneling current is in exponential relation with the vacuum spacing between the tip and the surface, simulated STM images can be generated by equation;

$$E_{total} = \sum_{n}^{h} E_n e^{-kz_n}, \tag{2.25}$$

where E_{total} is the summed charge density matrix, n is the layer number, h is the height of the ReS_2 monolayer, E_n is the nth layer partial charge density matrix, k is a constant, and z_n is the distance from the artificial STM tip in the z direction.

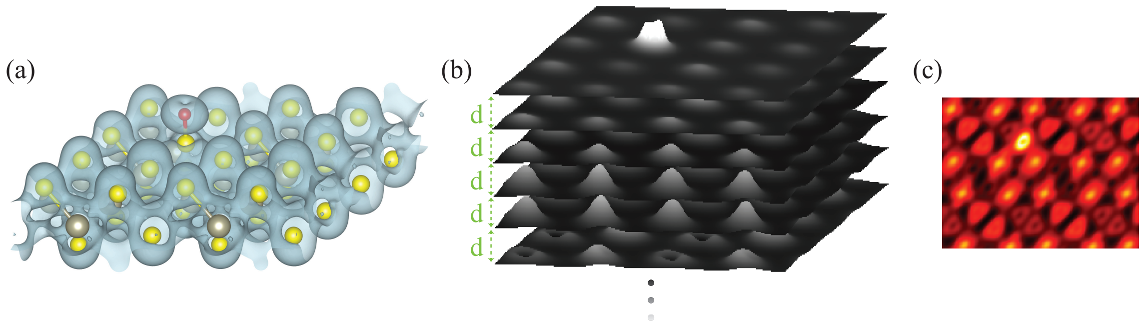

Figure 2.2. (a) Partial charge densities of O adsorbed ReS_2 surface. (b) 3D plotted equally distributed layers of partial charge densities corresponding (a). (c) Simulated STM image of O adsorbed ReS_2 surface, calculated by equation 2.25

2.1.5. Computational Details

First-principles calculations were carried out using Vienna *ab-initio* Simulation Package (VASP).[77,78] Plane-wave basis projector-augmented wave (PAW) potentials were used with the GGA was employed as the exchange-correlation functional in Perdew-Burke-Ernzerhof (PBE).[79,71] In the calculations, van der Waals corrections were supplied by one of the DFT-D2 method, DFT-D3 method with Becke-Jonson damping, and optB86b-vdw functionals.[80,81,82,83] Vibrational properties were calculated using small displacement method within the PHON and phonopy codes.[73,74] In order to get close to the experimental band gap values, Heyd-Scuseria-Ernzerhof (HSE) hybrid functional was employed.[72] Charge transfer analysis was carried out by the Bader technique.[84]

Structural optimizations were performed with the convergence criteria between the consequent electronic and ionic steps were set as 10^{-5} and 10^{-4} eV, respectively. In order to avoid interactions between layers, at least 10 Å of distance in the vacuum were taken between the nearest species. Systems were allowed to relax until the pressure on the unit cell is less than 1 kB in all directions. Cohesive energies of systems are calculated by the formula;

$$E_{coh} = -\left[E_{system} - \sum_i n_i E_i\right]/n_{total} \tag{2.26}$$

where E_{system} is the total energy of the optimized system, n_i is number of i^{th}

atom, E_i is the single atom energy of the i^{th} atom. Density of states, charge densities, and wave eigenvalues of the systems were calculated in a Γ-centered k-point mesh with high enough parameters to increase the accuracy of results.

2.2. Experimental Methodology

2.2.1. Graphene Based Gas Sensors

Brief information about experimental methods regarding the graphene based gas sensors that are used during this thesis study is given in this subsection.

2.2.1.1. Chemical Vapor Deposition of Graphene

Graphene samples were grown on ultra-smooth Cu foils by chemical vapor deposition method in a Proterm Furnaces PC442 split tube furnace. Varying sizes of the Cu foils were prepared and placed on quartz slide which was inserted into a quartz tube. Quartz tube was then sealed, and vacuumed down to 4 Torr. 100 sccm H_2 flow was applied into the quartz tube and the furnace was heated up to 1035°C. Once the temperature was reached to 1035°C, 10 sccm of methane (CH_4) gas flow is given into the system for 60 seconds as carbon precursor. Afterwards, CH_4 flow was stopped, and the furnace was left to cool down to the room temperature. H_2 flow was stopped once the furnace is cooled down below 100°C.

Graphene growth is accomplished on Cu foils. In order to prepare for the transfer, graphene layers on Cu subsrate were covered with photoresist liquid (Shipley 1813) and annealed at 65° overnight.

2.2.1.2. Transfer of Graphene

Graphene transfer process was carried out by firstly etching the Cu substrate with nitric acid solution. After the Cu is etched, surface of graphene was rinsed with deionized water and placed on the glass substrate with Cr/Au electrodes. Sample was heated at 80° for 30 seconds. Photoresist layer was removed by dissolving in acetone.

2.2.1.3. Characterization

Raman Analysis

Raman spectroscopy measurements were conducted with Monovista (Princenton Instruments) and Raman signals were recorded in spectral range of 1100-3000 cm-1 using Ar^+ ion laser 514 nm with a 600 grooves per mm grating. Collection of Raman scattered light to observe all D, G and 2D signals of CVD graphene. Raman analysis revealed that our sensors have bilayer graphene. Although the growth on Cu foils result in single layer graphene, due to the Ni contamination, graphene samples were gathered multilayer.

2.2.1.4. Graphene Based Devices in Gas Sensing Applications

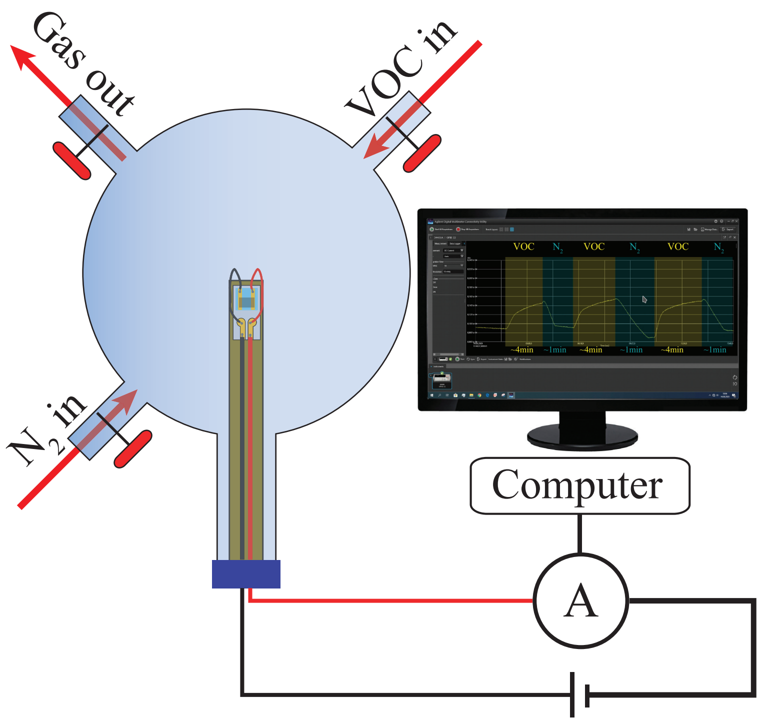

Figure 2.3. Experimental setup for gas sensing application.

Sensor platform was connected to sample holder and placed in 1 L volume chamber. A laboratory power source, HP 34401A Digital Multimeter, and the sensor were serially connected. Gas response of graphene based gas sensors were examined under different volatile organic compounds (VOCs) by measuring the changes in their current. Experimental setup is illustrated in Figure 2.3.

Relative response between VOCs are examined by simplifying the response to the form $I - I_{min}$. For selective selection of certain gas species, voltage dependent and concentration dependent measurements were carried out. Additionally, selectivity is investigated in mixed gas systems.

CHAPTER 3

OCTAHEDRALLY COORDINATED SINGLE LAYER CaF_2: ROBUST INSULATING BEHAVIOUR

CaF_2 is a material with wide range of applications owing to its significant properties. In dentistry, CaF_2 is used as an effective agent for preventing dental decay and increasing microbial resistance.[85,86,87,88] Due to the transparency in the infrared region, CaF_2 is found in useful in infrared spectroscopy.[89,90,91] In addition, CaF_2 is widely used to build lasers.[92,93,94,95,96,97] With the increasing demand in new two-dimensional (2D) materials thin films have been grown by numerous methods. Thin films of CaF_2 started gaining attention in nanoelectronic applications.[98] Although number of studies relating to growth of thin CaF_2 films increase, ultrathin form of CaF_2 is not reported to the best of our knowledge. With the increasing demand in nanoelectronics, insulating materials in nanoscale are required.

Most of the applications in nanoscale that have been demonstrated so far, have used h-BN as an insulating layer. It is reported to have band gap of 5.765 eV.[99] It is shown to lower the work function of the covered material. Utilizing its insulating characteristic, h-BN is reported to be sandwiched between two semiconductors, MoS_2 and GaN, a new diode is fabricated.[100] A method called “patterned regrowth" is reported by Levendorf *et al.*,[101] which allows spatial control over graphene and h-BN which provides a new approach for new low dimensional electronics. Reports indicate that h-BN have significant properties other than its insulating character. One of the important properties of h-BN is its thermal stability. h-BN is reported to remain stable up to 850°C.[102] Thermal stability at high temperatures makes h-BN a beneficial material in nanodevices which tend to operate at high temperatures. In addition to that, being an inert crystal, coating a surface with h-BN prevents surface degradation.[103]

Low dimensional crystals of CaF_2 is grown epitaxially even before the discovery of graphene.[104] However, in our best knowledge, studies about 2D CaF_2 in 1T structure are limited. Ultrathin CaF_2 recently epitaxially grown on bilayer MoS_2 to be used in building a field effect transistor (FET) as it is reported by Illarionov *et al.*.[105] This FET is found to have low subthreshold swings of 90mV dec^{-1} and up to 10^7 on/off current ratios.

Based on these results, CaF_2 is believed to have particular potential in 2D electronics. In this study, motivated by the potential hold by CaF_2 in nanotechnology, properties of 2D and 1D CaF_2 structures are predicted by performing *ab* initio calculations. Phonon and electronic band structures are presented for the dynamically stable CaF_2 monolayer. Results are compared with the well-known 2D insulator h-BN.

Here, using first-principles calculations, structural, vibrational, and electronic properties of single-layer calcium fluoride (CaF_2) are investigated. Dynamical stability of 1T-CaF_2 is confirmed by the phonon dispersions. Raman active vibrational modes of 1T-CaF_2 enable its characterization via Raman spectroscopy. In addition, the calculated electronic properties of 1T-CaF_2 confirmed insulating behavior with an indirect wide band gap which is larger than that of well-known single-layer insulator, h-BN. Moreover, one-dimensional nanoribbons of CaF_2 are investigated for two main edge orientations, namely zigzag and armchair, and it is revealed that both structures maintain the 1T nature of CaF_2 without any structural edge reconstructions. Electronically, both types of CaF_2 nanoribbons display robust insulating behavior with respect to the nanoribbon width. Results show that both 2D and 1D form of 1T-CaF_2 show potential in nanoelectronics as an alternative to the widely-used insulator h-BN with its similar properties and wider electronic band gap.

3.1. Structural, Vibrational, and Electronic Properties of Pristine 1T-CaF_2

Truncation of the bulk, face-centered-cubic (FCC) fluorite structured CaF_2, or epitaxial growth of calcium fluorite crystal in (111) direction as a single layer leads to the formation of CaF_2 in 1T structure. Crystal structure of 1T-CaF_2, consisting of one Ca atom sandwiched between two trigonally arranged F atoms in its primitive cell, is shown in Figure 3.1(a). The primitive cell of the 1T-CaF_2 has a hexagonal symmetry, with the optimized lattice parameters of 3.58 Å. Bond legth between Ca and F atoms is 2.29 Å. The Bader analysis results reveal that each Ca atom in unit cell donates 1.6 e while each F atom receives 0.8 e. Cohesive energy per atom in the unit cell of single layer CaF_2 is calculated to be 5.42 eV. In comparison with other 2D materials, cohesive energy of CaF_2 is higher than MoS_2, which is reported as 5.05 eV per atom,[106] lower than graphene and h-BN, which are reported to be 10.04 eV[107] and 7.01 eV[108] per atom, respectively.

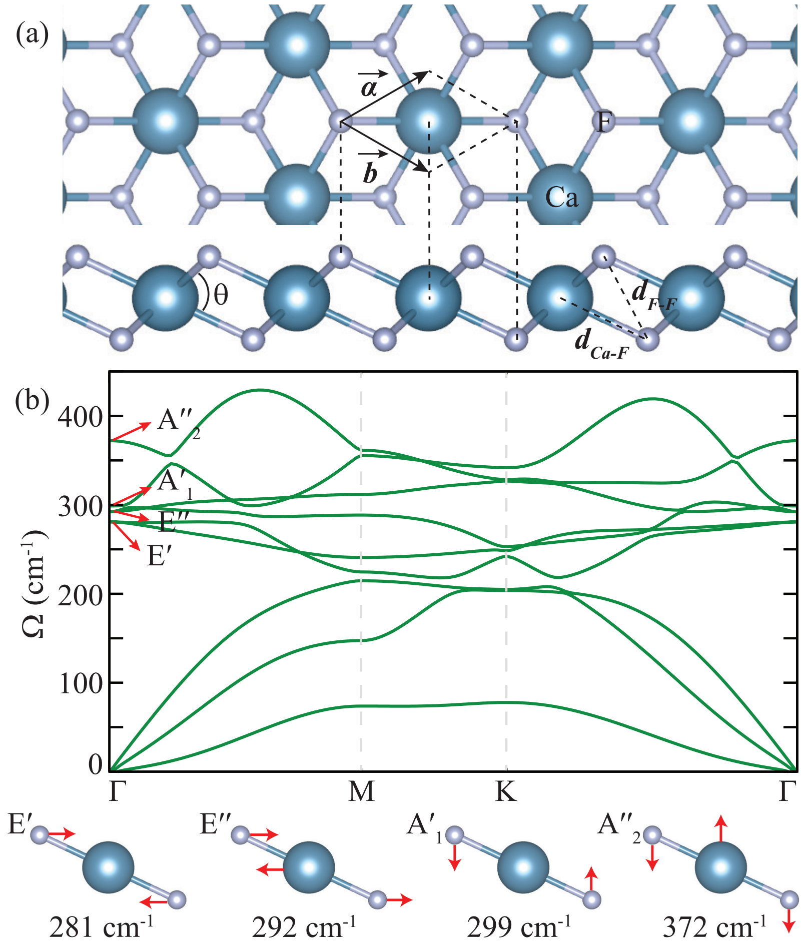

Figure 3.1. (a) Top and side views of 1T-CaF_2. (b) Phonon dispersion of 1T-CaF_2. Modes with corresponding frequencies are shown in the inset. Reproduced from Ref.[14] with permission from the PCCP Owner Societies.

Vibrational properties of CaF_2 crystal in 1T phase are studied through their phonon dispersions. Dynamical stability is confirmed by all real eigenvalues in the phonon band diagram. Phonon bands and characteristics of each optical mode are presented in Figure 3.1(b). Unit cell of 1T-CaF_2 has one Ca and two F atoms, which displays 9 phonon modes in total; 3 acoustical and 6 optical. In optical modes there are 2 single degenerate modes, at 299 and 372 cm^1, and 2 double degenerate modes, at 281 and 292 cm^1. Due to hexagonal symmetry of the unit cell, phonon band crossing appears at K point in the Brillouin zone. Decomposition of optical modes at Γ point gives $\Gamma = 2E' + 2E'' + A_1' + A_2''$, where E', E'', A_1', and A_2'' are Raman active modes and have frequency of 281, 292, 299, and 372 cm^{-1}, respectively. In comparison with h-BN, the phonon bands of 1T-CaF_2 have lower frequency. Highest phonon band frequency at Γ point of h-BN is reported to be at 1345 cm^{-1}, which is 973 cm^{-1} higher than the highest phonon band frequency of CaF_2

Table 3.1. Properties of 2D CaF_2 and h-BN are as follows: lattice constant of primitive unit cell, (a); bond length between adjacent atoms, (d); bond angle, (θ); donated electron by per Ca/B, (ρ); cohesive energy per atom in the unit cell, (E_c); energy band gap calculated within GGA-PBE, (E^{PBE}); energy band gap calculated within GGA-PBE+HSE06, ($E^{PBE+HSE}$); experimentally observed band gap, (E^{exp}); work function, (Φ). Reproduced from Ref.[14] with permission from the PCCP Owner Societies.

	a (Å)	d (Å)	θ (°)	ρ (e^-)	E_c (eV/$_{atom}$)	E^{PBE} (eV)	$E^{PBE+HSE}$ (eV)	E^{exp} (eV)	Φ (eV)
1T-CaF_2	3.58	2.29	76.88	1.64	5.42	7.17	9.49	-	8.67
h-BN	2.51[107]	1.45	120	2.13	7.01[108]	4.65	5.77	5.5[109]	5.62

Table 3.2. Mechanical properties and Raman-active modes of 2D CaF_2 and h-BN are as follows: in-plane stiffness, (C); Poisson ratio, (ν); Raman active modes. Reproduced from Ref.[14] with permission from the PCCP Owner Societies.

	C (N/m)	ν	R-active modes (cm^{-1})
1T-CaF_2	44	0.24	281, 292, 299, 372
h-BN	273[110]	0.22[110]	1365

that is observed to be at 372 cm^{-1}. This difference indicates that 1T-CaF_2 is a softer 2D structure than h-BN. In addition, mechanical properties such as in-plane stiffness and Poisson ratio are calculated as 44 N/m and 0.24, respectively. In order to determine the thermal stability of 1T-CaF_2, *ab-initio* Molecular Dynamics simulations are carried out. For the MD simulations NVE ensemble is used. K-point sampling is taken $2\times2\times1$ for $5\times5\times1$ supercell. The temperature is increased from 0 K to 1000 K in 10 ps with 2 fs between consequent steps. Results of the simulations reveal that CaF_2 monolayer is able to withstand such high temperatures.

Electronic band dispersions clearly indicate that 1T-CaF_2 is a wide band gap insulator as it is presented in Figure 3.2 (a). Band gap of the single layer CaF_2 is calculated to be 7.17 eV. Major contributions to the valence and conduction bands arise from the F-*p* and Ca-*d* orbitals, respectively. However, near conduction band minimum, the Ca-*s* orbitals exhibit higher density. In addition to GGA-PBE calculations, GGA-PBA + HSE06 functional is used in order to increase the accuracy of the electronic band calculations. As result monolayer CaF_2 retains its insulating behavior. PBE+HSE bands around Fermi level completely match the PBE bands however, PBE+HSE and PBE bands near conduction band do not match. Band gap of the 2D insulator widens to 9.49 eV. Wide band gap of 1T-CaF_2 is estimated to be higher than well-known insulator h-BN with band gap about $\approx$5.5 eV,[109] which makes 1T-CaF_2 an appealing insulator.

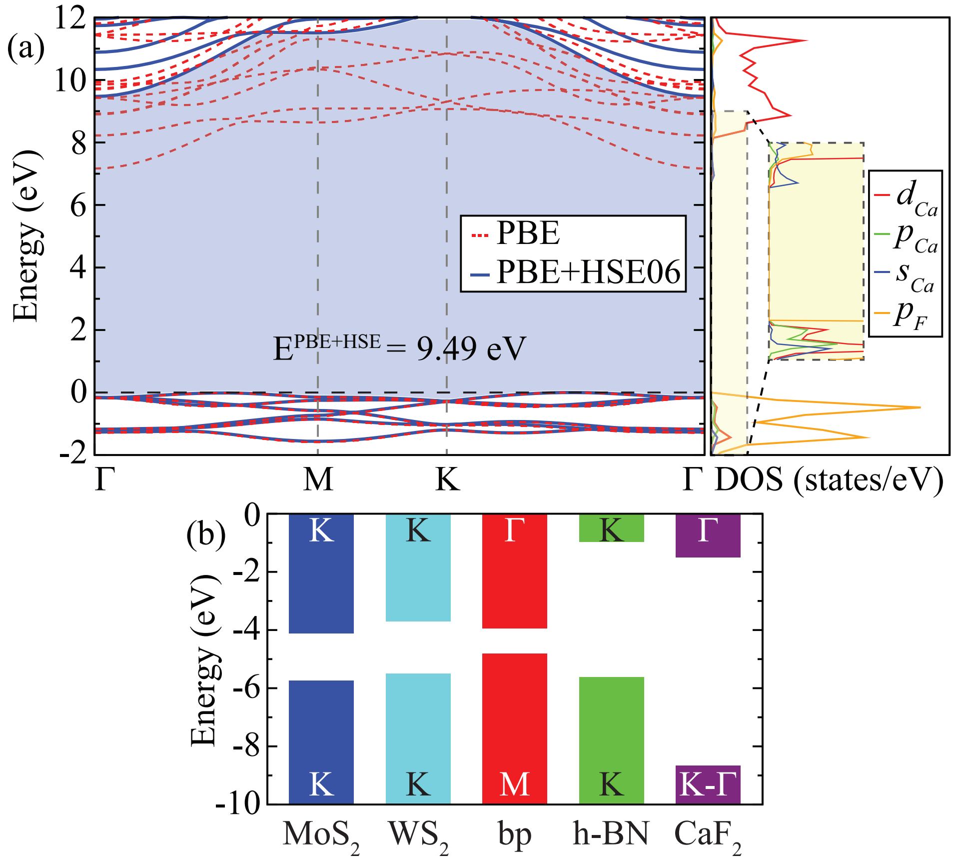

Figure 3.2. (a) Electronic band structure and PDOS of 1T-CaF_2, (b) comparative band alignment of MoS_2, h-BN, black phosphorous (bp), WS_2, and 1T-CaF_2 where vacuum energies are set to zero. Reproduced from Ref.[14] with permission from the PCCP Owner Societies.

Band alignment comparison is an important method that is used to predict band modification in a heterostructure in various studies.[111,112,113,114,115] There are three types of heterojunctions; type I (straddling gap), type II (staggered gap), and type III (broken gap) heterojunction.[116] Band alignment of 1T-CaF_2 is compared with well-known monolayers such as semiconducting MoS_2, black phosphorous (bp), WS_2, and insulating h-BN by setting their vacuum energies to zero, presented in the Figure 3.2 (b). Valence band maximum (VBM) and conduction band minimum (CBM) are shown in the corresponding bars. 1T-CaF_2 has high lattice mismatch value with the given crystals. However, band gap alignment gives information about which type of heterojunction 1T-CaF_2 can form. In case of a heterostructure of 1T-CaF_2 and a semiconducting material such as

MoS_2, black phosphorous, or WS_2 with suitable lattice constant, type I heterojunction is predicted to be formed. Contrarily, in case of a heterostructure of 1T-CaF_2 and h-BN like crystal with suitable lattice constant, type II heterojunction is predicted to be formed. Thus, stable ultra-thin CaF_2 with its wide electronic band gap is a suitable material for nanoscale heterojunction and substrate applications.

3.2. Nanoribbons of CaF_2: Width-Independent Band Gap

Nanoribbons of 2D materials have been drawing attention due to the unique properties and potential nanoscale applications they present.[117] In this section, nanoribbons (NRs) of CaF_2 are studied. Depending on the edge orientation of CaF_2 NRs, two different types are investigated, zigzag NRs and armchair NRs. An illustration of the NR structure is given in Figure 3.3a. The width of the NRs is indicated by the number N of Ca atoms in the unit cell. Note that for both types of NRs, the ratio between Ca and F atoms is stoichiometric, i.e., there are N Ca atoms and $2N$ F atoms in the unit cell. To study the width dependence of the electronic structure, for zigzag NRs,the NR width ranging from 4 to 10 and for armchair NRs, the NR width ranging from 5 to 15 are considered. It is found that for both type of NRs, there is no remarkable structural reconstruction, and the 1T structure is well maintained, as shown in Figure 3.3a. The edge energy of different NRs is shown in Figure 3.3b. For a NR with width N, the edge energy is defined as $(E_{NR} - NE_{2D})/(2L)$, where E_{NR} is the total energy of the NR unit cell, E_{2D} is the total energy of the unit cell of monolayer CaF_2, and L is the lattice constant of the NR. It describes how much extra energy is needed to create a new edge from the 2D layer. According to Figure 3.3b, for both zigzag and armchair NRs, the edge energy decreases as the width increases. Moreover, it is seen that the edge energy of zigzag CaF_2 NRs is smaller than that of armchair CaF_2 NRs when their widths are comparable (e.g., N=6 for zigzag NR and N=10 for armchair NR). A possible origin is that there are more dangling bonds at the armchair edge than at the zigzag edge. Overall, the magnitude of the edge energy is 0.2-0.4 eV/Å. In contrast, for NRs of typical transition-metal dichalcogenides like MoS_2 and WS_2, the edge energy is about 0.6 eV/Å.[118] Thus, the formation of CaF_2 NRs is relatively easier.

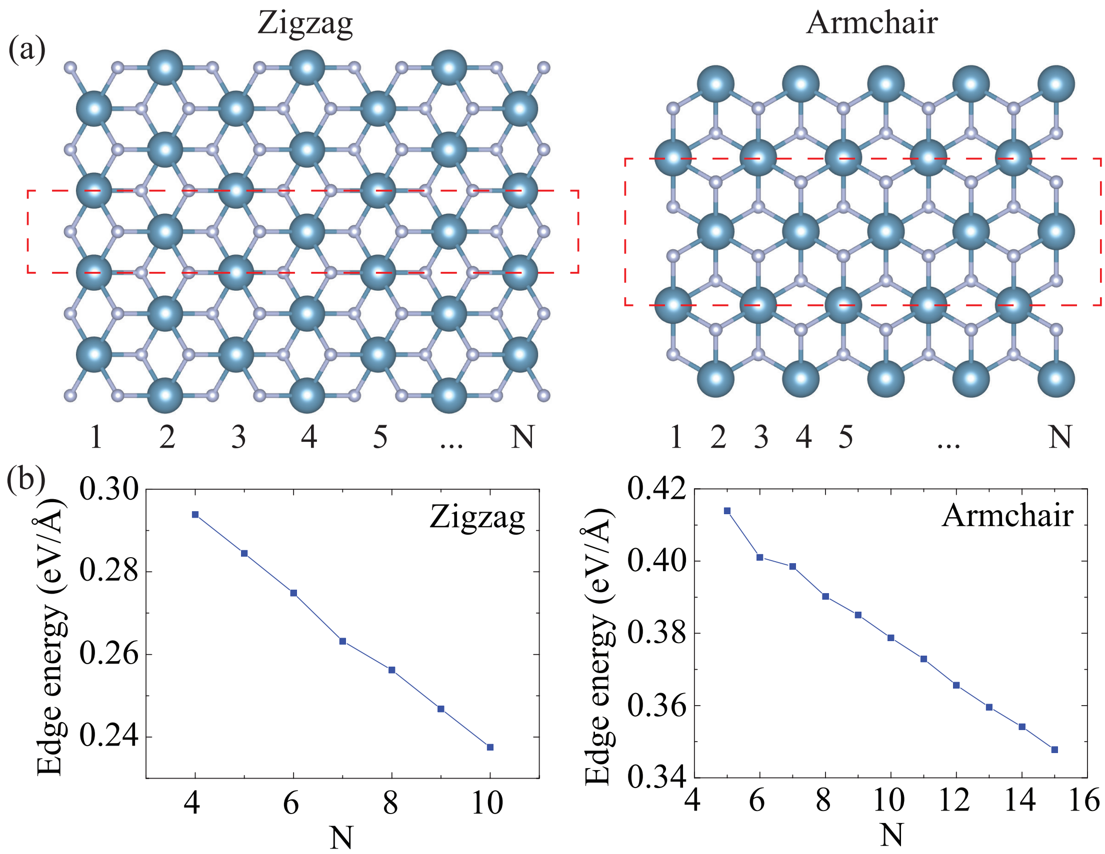

Figure 3.3. (a) Structure of zigzag and armchair CaF_2 NRs. The dashed lines indicate the unit cells. (b) Edge energy of the NRs as a function of ribbon width. Reproduced from Ref.[14] with permission from the PCCP Owner Societies.

Next, the electronic properties of the NRs in terms of their width-dependent electronic band structures are investigated. Due to the quantum confinement effect, usually the band gap of a NR is larger than that in a 2D layer, and decreases as the width increases. In Figure 3.4a the band gap of different CaF_2 NRs is presented. It is interesting to see that the band gap is smaller than the monolayer, and almost independent to the ribbon width. For zigzag NRs, the band gap is about 6.5 eV, and for armchair NRs, the gap is about 6.3 eV. In Figure 3.4b-c the band structures of selected NRs are given. For zigzag NRs, the CBM is located at the Γ point, whereas the VBM is at $\sim 2/3$ between Γ and X. On the other hand, both CBM and VBM are at the Γ point for armchair NRs. To further understand the width-independent band gap, one can analyze the character of the VBM and CBM states, as shown in Figure 3.4d. It appears that, all these states are mainly localized at the edge of the NRs, indicating strong edge effects in CaF_2 NRs. Because of the highly localized character, the transverse confinement effect to the CBM and VBM is quite small, leading to the width-independent band gap. Although the band gap is insensitive to the NR width, it can be more sensitive to the number of layers because the edge states can be affected by the out-of-plane confinement.

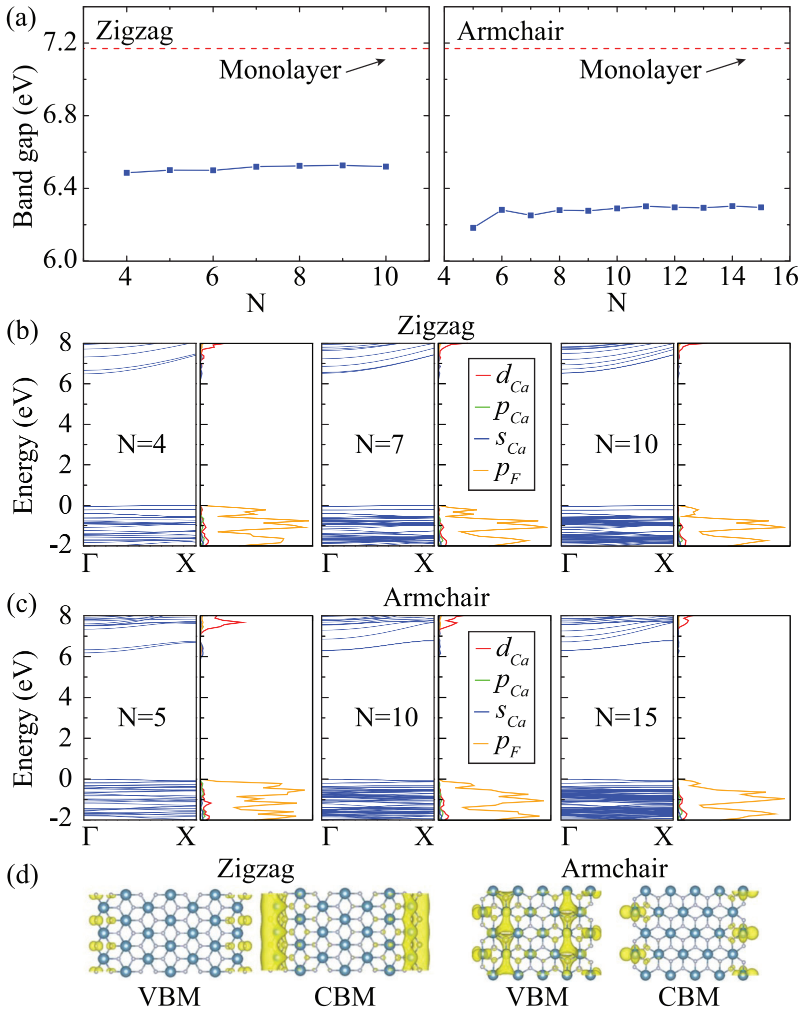

Figure 3.4. (a) Band gap of the NRs as a function of ribbon width. (b) Band structure and PDOS of selected zigzag NRs. (c) Band structure and PDOS of selected armchair NRs. (d) The CBM and VBM states for the 7-zigzag NR and the 10-armchair NR. Reproduced from Ref.[14] with permission from the PCCP Owner Societies.

3.3. Conclusions

In this study, investigation on 1T-CaF_2 and its nanoribbons are carried out. Structural, vibrational, electronic properties are presented. Vibrational calculations revealed that monolayer CaF_2 has four Raman active modes. Having lower frequency phonon bands compare to h-BN revealed that 1T-CaF_2 is relatively softer material. In spite of having softer structure than h-BN, it is predicted to possess wider band gap of 7.17 eV by PBE and 9.49 eV by PBE+HSE06 functionals. Additionally, work function of 1T-CaF_2 is calculated to be much higher than h-BN while having lower cohesion between atoms in the unit cell by 1.58 eV/atom. In addition to the 2D structure of 1T-CaF_2, nanoribbons of CaF_2 are studied. Both in zigzag NRs and armchair NRs of CaF_2, 1T structure is maintained without reconstructions. Width dependent edge energy calculations revealed that edge energy decreases in both zigzag and armchair NRs with increasing width. With comparable widths, zigzag NRs of CaF_2 are found to have less edge energy than armchair NRs of CaF_2. Calculated edge energy showed that formation of CaF_2 NRs is easier compared to typical TMDs. In the electronic band structures of NRs, band gap of NRs is found almost-independent to the width, and interestingly smaller than the monolayer CaF_2. Band decomposed charge densities of valence and conduction bands are examined and it is seen that states are localized at the edges of NRs. In conclusion, 1T-CaF_2 shows great potential in nanoelectronic applications in 2D and 1D form as a wide band gap insulator.

CHAPTER 4

STABLE SINGLE-LAYERS OF CALCIUM HALIDES (CaX_2, X = F, Cl, Br, I)

Following graphene, many novel 2D materials are investigated. Among these materials, h-BN is a well-known insulator which have been widely used as a separator in van der Waals heterostructures.[99] As a heterojunction diode was fabricated using h-BN as the insulating layer, its performance was reported to be comparable to the classical $p-n$ junction diodes.[100] In addition, the use of h-BN in the development of atomically thin integrated circuits has brought a new approach for novel low dimensional electronics.[101] Moreover, using h-BN as an encapsulating agent was reported to efficiently enhance stability of TMDs.[103]

Calcium halides are inorganic materials possessing great potential in various applications. Among calcium halides, CaF_2 is known as the fundamental source for the synthesis of hydrofluoric acid.[119] CaF_2 has been widely used in dental practice in order to cover dental cavities[85,86,87,120,88] and also have been used in high-power diode pump and ceramic lasers.[92,93,94,95,96] On the other hand, due to its insulating property, CaF_2 has been an appealing material in micro- and nano-electronics. In our previous study single-layer CaF_2 in 1T structure was investigated, substantial properties are presented and compared to the well-known single-layer insulator h-BN.[14] $CaCl_2$, is another important member of Ca-halides which has been extensively used in electrolyte solutions.[121] In addition, $CaCl_2$ was reported to increase the capture performance of CO_2 making it an important candidate for reducing the energy consumption and increasing the capture capacity.[122,123] Moreover, $CaCl_2$ plays an important role in extending shelf life of fruits and vegetables making it suitable for applications in agricultural and food chemistry.[124,125,126] Furthermore, mixing of $CaCl_2$ with another calcium halide, $CaBr_2$, was shown to be a good process for ammonia storage.[127,128] $CaBr_2$ was used in alteration of vapor-liquid equilibrium of acetone and methanol system, resulting with elimination of azeotropic point of the system completely and granting it for obtaining ideal gas behavior.[129] Moreover, $CaBr_2$ was reported as an instant and renewable brominating agent for substituted aromatics which increases the demand in industrial and pharmaceutical fields.[130] Likewise the other calcium halides,

CaI_2 was shown to have applications in numerous areas such as to be an excellent catalytic agent for the synthesis of carbonates from epoxides.[131,132,133] Additionally, laser excitation of CaI_2 in ethanol solution revealed to form cluster ions in mass spectrometric analysis. Due to the layered structure, CaI_2 is reported as a material that can be exfoliated into single-layer with relatively low cleavage energy.[134,135] Apparently, bulk calcium halides have various important application fields. However, investigation of ultra-thin structures of calcium halides is quite important for their nanodevice applications which have been mainly ignored in previous studies.

In this study, structural, vibrational, electronic, and mechanical properties of single-layer calcium halide (CaX_2) structures are investigated using first principles calculations. CaX_2s in 1T and 1H structures are found to be dynamically stable. Raman active modes are predicted by the characteristics of the vibrational modes in phonon calculations. Raman spectra are shown to exhibit rich information for the characterization of structural phases of a single-layer CaX_2 and even for the distinguishing of the structures having the same phase. In addition, insulating behavior of all single-layer CaX_2 is shown to make them alternative materials to well-known ultra-thin insulator, h-BN. Moreover, the trends between calcium halide structures and their charge transfer, in-plane stiffness, cohesive energy, and work function are discussed.

4.1. Structural, Vibrational, and Elastic Properties

Single-layer CaX_2 structures can be formed either in 1H or 1T phases by truncation from their bulk or by growing in different orientation on a substance. In this study, 1H and 1T phases of CaX_2 single-layers are investigated and their dynamical stabilities are examined via phonon band dispersions through the whole Brillouin zone (BZ). The 1T-phase structure (see Fig. 4.1(a)) is composed of a Ca layer sandwiched between two halogen atom layers leading to the P$\overline{3}$m2 space-group-symmetry. On the other hand, the 1H-phase (see Fig. 4.1(b)), in which Ca atom is sandwiched between two halogen atom layers, which are separated symmetrically with respect to the Ca layer, exhibits P$\overline{6}$/m$\overline{2}$ space-group-symmetry. For all CaX_2 structures, 1T-phase is found to be energetically more favorable as compared to the 1H-phase. The total energy differences per primitive unit cell are calculated to be 0.73, 0.43, 0.35, and 0.28 eV for structures of F, Cl, Br, and I, respectively. As listed in Table 4.2, the optimized in-plane lattice parameters of 1T-CaX_2 vary between 3.58 and 4.47 Å as the halogen atom changes from F to I. On the other hand, those for 1H-phase are quite smaller from those of 1T-phase and are found to vary between 3.40 and 4.32 Å. Notably, as the atomic radius of the halogen atom increases, the corresponding in-plane lattice parameters increase in both phases accordingly. The Bader charge analysis reveals that in 1T-CaX_2 structures, each Ca donates its 1.6 e to halogens. Similarly, in 1H structures each Ca atom donates its 1.5 e to halogen atoms in 1H-CaX_2. Moreover, as listed in Table 4.2, the cohesive energies per atom decrease as the atomic radius increases in both phases of CaX_2 structures. In addition, cohesive energies of the bulk CaX_2 structures are calculated. Bulk CaF_2 which has Fm$\overline{3}$m space-group-symmetry has cohesive energy of 5.62 eV/atom. Bulk $CaCl_2$ and $CaBr_2$ structures with Pnnm and P4_2/mnm space-group-symmetries have cohesive energies per atom of 4.20 eV/atom, 3.79 eV/atom. Bulk CaI_2 with layered structure (P$\overline{3}$m1 space-group) has 3.42 eV/atom cohesive energy per atom in unit cell.

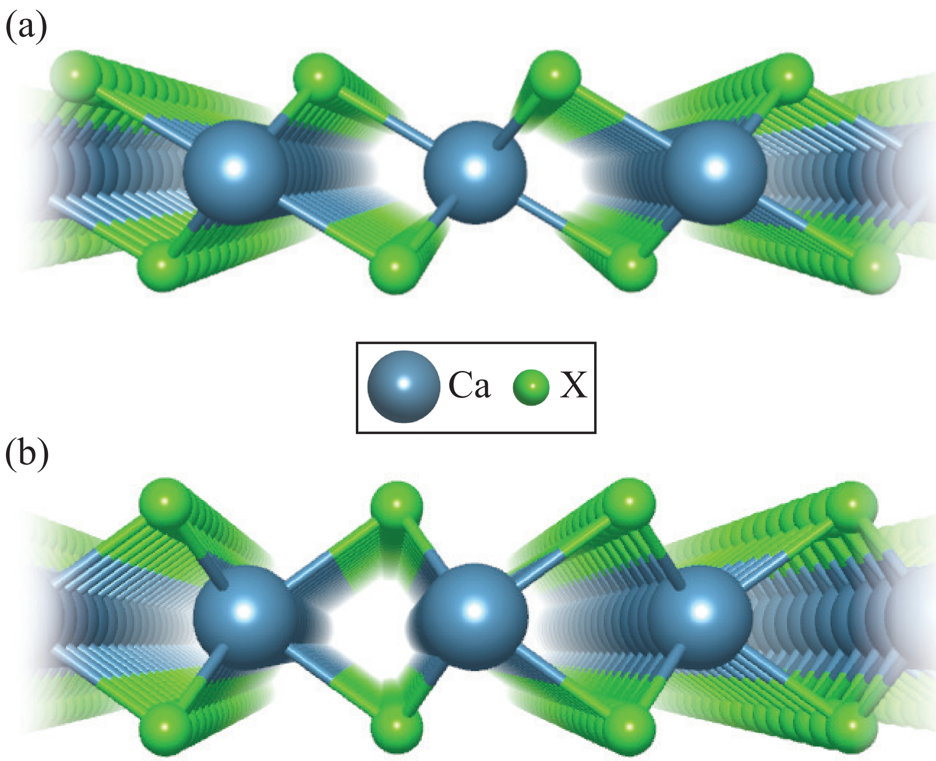

Figure 4.1. Crystal structures of (a) 1T-CaX_2, (b) 1H-CaX_2, (X = F, Cl, Br, I). Adapted from Ref.[136] with permission from AIP Publishing LLC.

The dynamical stabilities of the 1T and 1H phases are also verified by calculating

Table 4.1. Calculated parameters for single-layer CaX_2s: optimized in-plane lattice constants, ($a = b$); bond length between a Ca and the halogen, (d_{Ca-X}); distance between X atoms, (d_{X-X}); the X-Ca-X bond angle, (θ); donated electron by per Ca, (ρ_{Ca}); cohesive energy per atom in the unit cell, (E_c); work function, (Φ). Adapted from Ref.[136] with permission from AIP Publishing LLC.

	Phase	a (Å)	d_{Ca-X} (Å)	d_{X-X} (Å)	θ (°)	ρ_{Ca} (e^-)	E_c (eV/$_{atom}$)	Φ (eV)
CaF_2	1T	3.58	2.29	2.84	76.88	1.6	5.42	8.67
	1H	3.40	2.31	2.43	63.56	1.6	5.17	10.13
$CaCl_2$	1T	4.10	2.76	3.70	84.09	1.6	4.17	7.98
	1H	3.90	2.78	3.27	72.03	1.5	4.03	8.10
$CaBr_2$	1T	4.24	2.92	4.02	86.92	1.5	3.77	7.39
	1H	4.06	2.95	3.58	74.67	1.5	3.65	7.46
CaI_2	1T	4.47	3.15	4.45	89.71	1.5	3.36	6.46
	1H	4.32	3.19	3.97	77.07	1.5	3.26	6.42

their phonon band dispersions through the whole BZ. As presented in Fig. 4.2, both 1T and 1H phases of single-layer CaX_2 are free from imaginary frequencies in the whole BZ, indicating their dynamical stability. In both phases, there are six optical phonon branches whose vibrational characteristics are shown on the right panel of the phonon band dispersions in Fig. 4.2. As a result of the in-plane isotropy of the structures, there exist two doubly-degenerate in-plane and two non-degenerate out-of-plane phonon modes in both phases of single-layer CaX_2 structures. 1T-CaX_2 crystals possess C_{3v} symmetry and the corresponding Raman active modes are denoted as A_{1g} and E_g. In both phonon modes, Ca atom has no contribution to the vibration while the halogen atoms vibrate out-of-phase against each other in the out-of-plane and in-plane directions, respectively. In all single-layer 1T-CaX_2, the frequency of A_{1g} is calculated to be higher than that of E_g and both phonon modes display phonon softening as the atomic mass of halogen increases. For the 1H-CaX_2 structures, there are two doubly-degenerate in-plane (E' and E'') and a non-degenerate out-of-plane (A_1) Raman active modes. The E'' is attributed to the in-plane vibration of halogens against each other and it has the lowest frequency in each single-layer structure. In E' phonon mode, Ca atom and the two halogen atoms vibrate out-of-phase in lateral directions. The other Raman active mode, A_1, is originated from the out-of-plane vibration of two halogen atoms against each other. In 1H-phases of CaF_2 and $CaCl_2$, A_1 has higher frequency than the E' mode indicating that the vertical component of the force

Table 4.2. Calculated parameters for single-layer CaX_2s: energy band gaps calculated within GGA, (E_{gap}^{GGA}); and within HSE06 on top of GGA, (E_{gap}^{HSE06}); in plane stiffness, (C); Poisson ratio, (ν); and the frequencies of the Raman active modes. Adapted from Ref.[136] with permission from AIP Publishing LLC.

	Phase	E_{gap}^{GGA} (eV)	E_{gap}^{HSE06} (eV)	C (N/m)	ν	R-active modes (cm^{-1})
CaF_2	1T	7.17	9.49	44	0.24	281, 299
	1H	6.34	8.73	38	0.49	134, 268, 414
$CaCl_2$	1T	5.79	7.57	22	0.21	149, 183
	1H	4.82	6.46	24	0.42	86, 180, 233
$CaBr_2$	1T	4.95	6.55	18	0.22	87, 114
	1H	4.19	5.65	22	0.40	52, 143, 147
CaI_2	1T	3.79	5.11	16	0.24	62, 84
	1H	3.19	4.38	21	0.37	40, 105, 132

constant between Ca-F and Ca-Cl is larger than the lateral component. However, as the atomic mass increases, the lateral component of the force constant between Ca-Br and Ca-I becomes dominant to that of vertical component. Therefore, in $CaBr_2$ and CaI_2 the E' phonon mode has higher frequency than that of the A_1 mode.

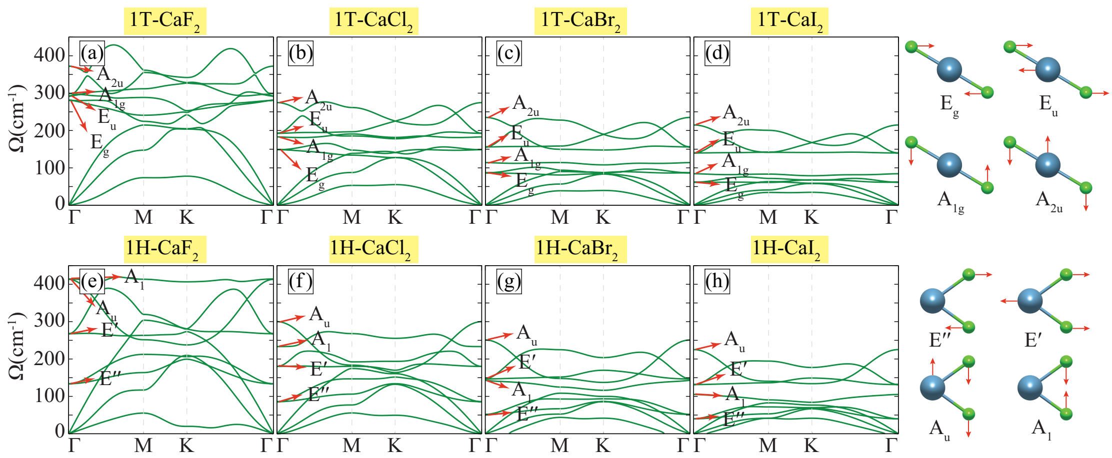

Figure 4.2. Phonon dispersions of (a) 1T-CaF_2, (b) 1T-$CaCl_2$, (c) 1T-$CaBr_2$, (d) 1T-CaI_2, (e) 1H-CaF_2, (f) 1H-$CaCl_2$, (g) 1H-$CaBr_2$, (h) 1H-CaI_2. Corresponding vibrational modes are presented in the inset. Adapted from Ref.[136] with permission from AIP Publishing LLC.

The in-plane stiffness, C, which is a measure of the rigidity of a material and the Poisson ratio, ν, which is the ratio of the transverse contraction strain to the longitudinal extension, describe the linear elastic properties of 2D materials. In order to determine the linear-elastic constants, the elastic strain tensor elements, C_{ij}, are calculated and the corresponding C and ν, values which are isotropic for all directions in the structures, are calculated and the results are listed in Table 4.2. The in-plane stiffness and the Poisson ratio are calculated using the formula;

$$C = \frac{(C_{11}C_{22} - C_{12}^2)}{C_{22}}, \tag{4.1}$$

$$\nu = \frac{C_{12}}{C_{22}} \tag{4.2}$$

As listed in Table 4.2, the calculated in-plane stiffness values indicate the ultra-soft nature of the CaX_2 structures in both phases. As compared to planar single-layers of graphene (330 N/m)[137,110] and h-BN (273 N/m),[110] single-layers of both 1T- and 1H-CaX_2 structures are very soft materials. Among the non-planar single-layers such as MoS_2 (122 N/m)[137,110] and WS_2 (122 N/m),[110] the Ca-X bonds are weak due to much smaller in-plane stiffness of the CaX_2 structures. In contrast, single-layers of CaX_2 have in-plane stiffness which are comparable to those for silicene (54 N/m)[110] and germanene (34 N/m).[110] Moreover, the calculated in-plane stiffness values are almost close to each other for the 1T- and 1H-phases of each CaX_2 indicating similar bonding characteristics in both phases. On the other hand, the Poisson ratios are calculated to be much larger for 1H-CaX_2 structures as compared to their values for 1T-phases. Such relatively large Poisson ratios of 1H-CaX_2 single-layers suggest more sensitive structural response to external loads, which can be beneficial for nanoelastic applications.

Properties of 1T and 1H phases of CaX_2 single-layers are compared by means of the charge transfer between Ca-X atoms, in-plane stiffness, cohesive energy, and work function as shown in Fig. 4.3. The charge donated by a Ca atom in both phases of all single-layers exhibits decreasing trend as the atomic radius increases (see Fig. 4.3(a)). In-plane stiffness of 1H and 1T phases shows decreasing trend from F to I structures however, relation between 1H and 1T phases for in-plane stiffness changes for CaF_2 arising from slightly smaller charge donation in 1H-CaF_2. Cohesive energies of the halide structures show decreasing trend with increasing atomic radius, and in all structures 1T phase is found to be energetically favorable. A decreasing trend for the work functions of CaX_2 single-layers is shown in accordance with electronegativity of the halogen atoms that is related to atom positions in the periodic table. Related to the slightly different charge transfer to F atom in its 1T and 1H phases, the differences between their work functions is the higher for CaF_2 structures.

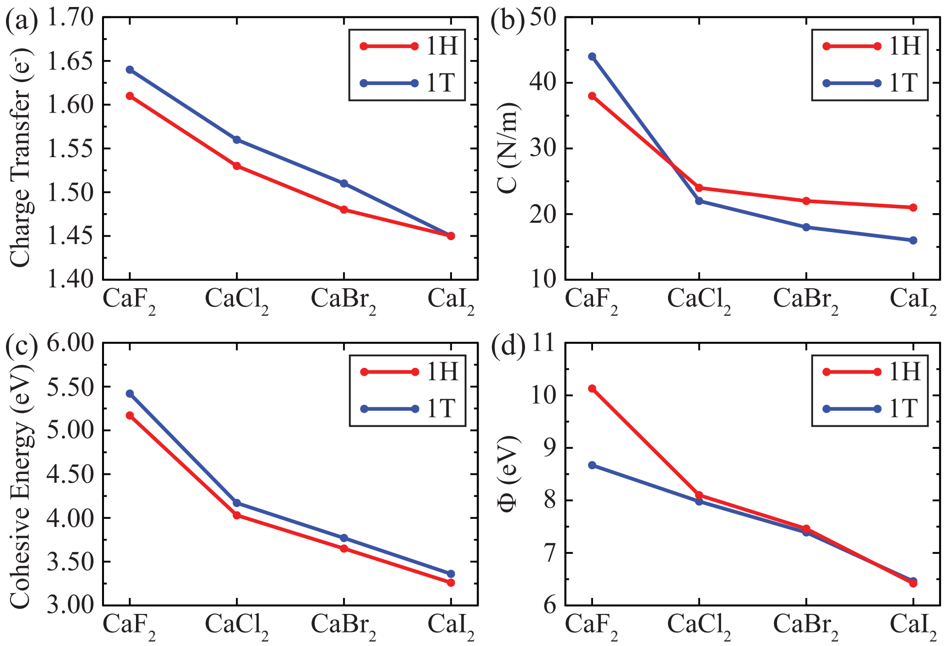

Figure 4.3. Graph of (a) CaX_2s versus charge transfer, (b) CaX_2 versus in-plane stiffness, (c) CaX_2 versus cohesive energy, (d) CaX_2 versus workfunction. Adapted from Ref.[136] with permission from AIP Publishing LLC.

4.2. Electronic Properties

Electronic properties of single-layer CaX2 phases are investigated in terms of their electronic band dispersions and they are presented in Fig. 4.4. Bare-GGA and HSE06 approximations reveal that both 1T- or 1H-CaX_2 structures are insulators. The calculated band gap values are found to be 9.49, 7.57, 6.55, and 5.11 eV for 1T-CaX_2 that a decreasing trend is found as the halogen atom changes from F to I. A similar trend is found for the single-layers of 1H-CaX_2 such that the band gap is 8.73 eV for CaF_2 and decreases to 4.38 eV for CaI_2.

The location of valence and conduction band edges indicates that all eight single-layer structures of CaX_2 are indirect band gap insulators. For the single-layers of 1H-CaF_2 and 1H-$CaCl_2$, the valence band maximum (VBM) is located in between the M and the K points while it shifts to the Γ point as the halogen atom changes to Br and I. On the other hand, the conduction band minimum (CBM), is found to reside at the Γ point for 1H-CaF_2

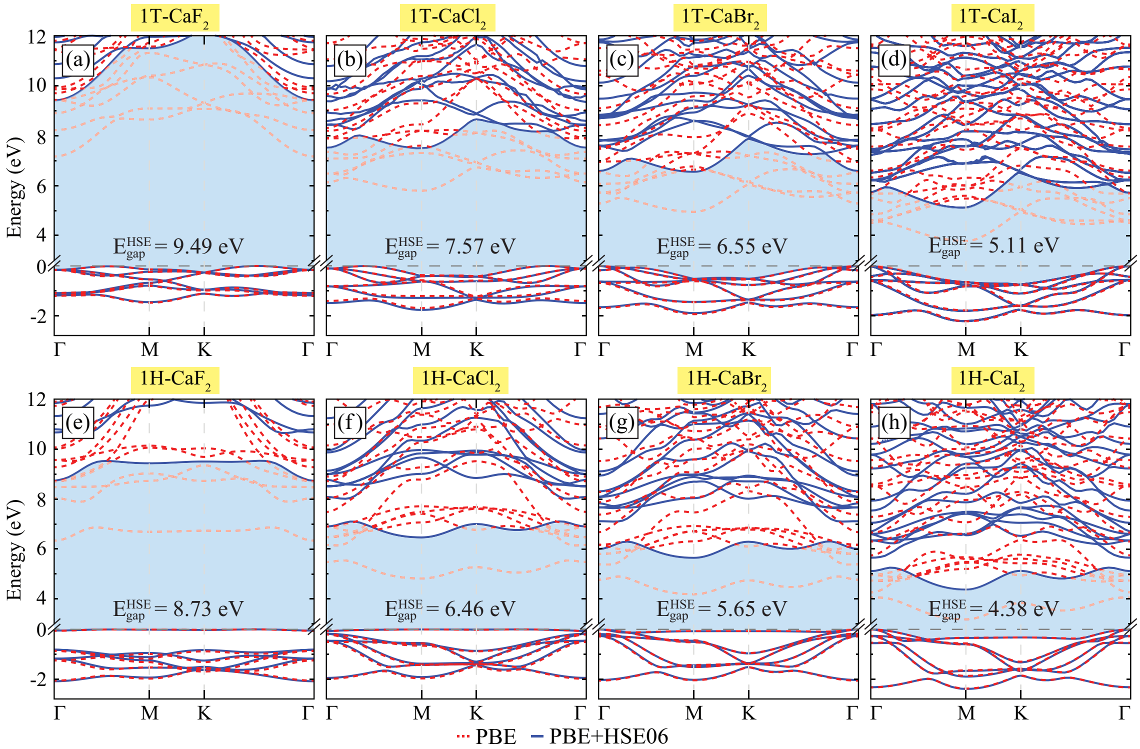

Figure 4.4. Electronic band structure of (a) 1T-CaF_2, (b) 1T-$CaCl_2$, (c) 1T-$CaBr_2$, (d) 1T-CaI_2, (e) 1H-CaF_2, (f) 1H-$CaCl_2$, (g) 1H-$CaBr_2$, (h) 1H-CaI_2. Adapted from Ref.[136] with permission from AIP Publishing LLC.

and it resides at the M point in the other three 1H-phase single-layers. Note that the top valence band is more dispersive in 1H-$CaBr_2$ and 1H-CaI_2 single-layers. In the case of 1T-CaX_2 single-layers, the CBM resides at the same points as 1H structures. However, for 1T-CaF_2 and 1T-$CaCl_2$ the VBM is found to reside in between the K and the Γ points while it is located at the Γ point for the other two 1T single-layers.

For the modification of the electronic properties ultra-thin materials, construction of heterostructures is quite important. In a typical vdW heterostructures, the band alignment comparison was shown to be an important method.[111,112,113,114,115] Three types of band alignments exist in heterojunctions; straddling gap, staggered gap, and broken gap heterojunctions are referred as type-I, type-II, and type-III, respectively.[116] Band alignment of CaX_2 in 1T and 1H structures along with well-known semiconducting single-layer materials MoS_2, WS_2, and single-layer insulator h-BN are presented in Fig. 4.5 (a), and the heterojunction types of these crystals are displayed in Fig. 4.5 (b). Results show that all the 1T- and 1H- CaX_2 structures reported in this study form type-I heterojunction with the semiconducting materials such as MoS_2 and WS_2 while they form type-II heterojunction with h-BN. In addition, HSE06 approximation is also used to determine the types of band alignments. Calculations reveal that alignment between WS_2/1H-CaF_2 and h-BN/1T-CaF_2 structures switches to type-I. Rest of the band alignments remain the same alignment type.

4.3. Conclusions

In this study, the structural, vibrational, and electronic properties of 1H- and 1T-phases of single-layer CaX_2 (X=F, Cl, Br, or I) structures were investigated. Our results revealed that the 1T-phase of CaX_2 is energetically favorable for all halogen atoms and both 1T and 1H-phases are found to be dynamically stable in terms of their phonon band dispersions. Either in 1H or in 1T-phase, significant phonon softening was found as the atomic radius increases from F to I structure in agreement with the increasing atomic radii. In addition, 1T-CaX_2 exhibits one doubly-degenerate in-plane and one non-degenerate out-of-plane Raman active modes while for 1H structures there are three Raman active modes (two doubly-degenerate and one non-degenerate) arising from the different symmetries in the structures. Moreover, the electronic band dispersions of single-layer CaX_2 structures indicated the indirect band gap insulating nature of all single-layers with decreasing band gaps from F to I crystals. Furthermore, the calculated linear elastic constants, in-plane stiffness and Poisson ratio, showed the ultra-soft nature of CaX_2 single-layers which is quite important for their nanoelastic applications. Overall, our study revealed that with their dynamically stable 1T- and 1H-phases, single-layers of CaX_2 crystals can be alternative insulators to the well-known single-layer h-BN.

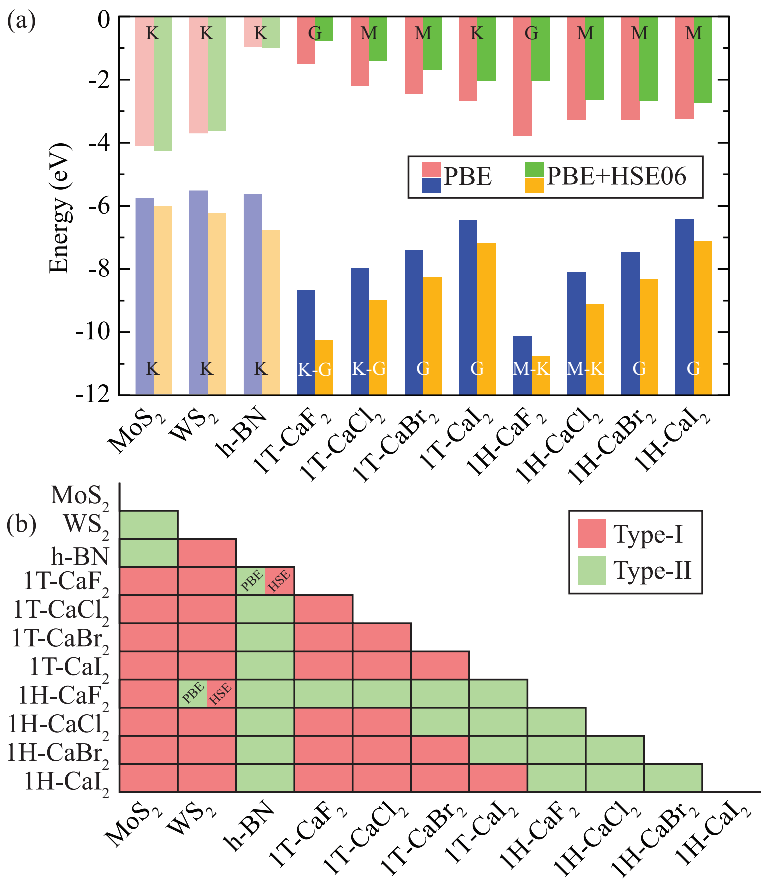

Figure 4.5. (a) Comparative band alignment of MoS_2, WS_2, h-BN, 1T-CaF_2, 1T-$CaCl_2$, 1T-$CaBr_2$, 1T-CaI_2, 1H-CaF_2, 1H-$CaCl_2$, 1H-$CaBr_2$, 1H-CaI_2 where vacuum energies are set to zero. (b) Table for the type of hetero-junctions. Blue and red bars represent the valance and conduction bands of GGA results, while orange and green bars represent the valance and conduction bands of HSE06 approximation. Crystals investigated in this article are displayed with darker color. On each bar, the location of VBM and CBM are also given. Red and green boxes in the table are for type-I and type-II, respectively. Adapted from Ref.[136] with permission from AIP Publishing LLC.

CHAPTER 5

VANADIUM DOPANT-AND STRAIN-DEPENDENT MAGNETIC PROPERTIES OF SINGLE LAYER VI_3

Searching for magnetism at two-dimensional (2D) limit has been the focus of interest over the past two decades since the discovery of graphene. Although, graphene and other synthesized 2D materials were announced to be non-magnetic, magnetism was shown to exist in case of introducing edges by cutting the material to a nanoribbon,[138,139,140] by adatoms,[141,142] or by the presence of vacancies.[143]

Even though layered magnetic van der Waals (vdW) crystals have been known for a long time,[144,145,146] recent experimental achievements on their exfoliation to monolayer limit made 2D magnetic materials important candidates for nanoscale spintronic applications.[147,148,149] Recently synthesized monolayers of semiconducting ferromagnets, CrI_3[15] and $Cr_2Ge_2Te_6$,[16] have increased the attention on 2D magnetic materials.[150] In addition, monolayer CrI_3 was reported to exhibit tunable magnetism between FM and AFM phases by either application of an external electric field[151] or magnetic field.[39,152] Moreover, recently other novel 2D magnetic monolayers such as $RuCl_3$,[17,153] VSe_2,[154,155] $MnSe_2$,[18] $FeCl_2$,,[156] and VCl_3,[157] have been added to library of 2D magnetic materials.

Magnetic layered vdW crystal of VI_3 was discovered long before the 2D magnetic materials were discovered.[158,159] In recent studies, VI_3 was reported to exhibit promising structural, magnetic and electronic properties similar to CrI_3.[160,161] Very recently, 2D form of VI_3 was successfully isolated as a FM semiconductor.[19] It was demonstrated that VI_3 undergoes structural and magnetic phase transitions at 78 and 49 K, respectively. In addition, it was observed that through the synthesis process, VI_3 forms with excessive doping of V atoms. It has been investigated in many 2D materials that dopants or vacancies can alter the electronic and magnetic properties of 2D crystals[162] and may lead to anisotropy in the structure.[163]

Motivated by the recent results on 2D VI_3,[19] in this study, we investigate and clarify the effect of experimentally observed excessive V atoms on the electronic and magnetic properties of dynamically stable monolayer VI_3. Our results reveal that FM ground state and AFM states of VI_3 exhibit distinctive features in their Raman spectra which allows one to distinguish the magnetic state. In addition, we show that increasing the V dopant level in VI_3 leads to the magnetic phase transition from FM-to-AFM as the structure is fully-doped. Furthermore, the pristine and fully-doped VI_3 structures are shown to display phononic stability in the range of $\pm 5\%$ biaxial strain with tunable electronic or magnetic properties.

5.1. Structural, Vibrational, and Electronic Properties of FM and AFM Phases of VI_3

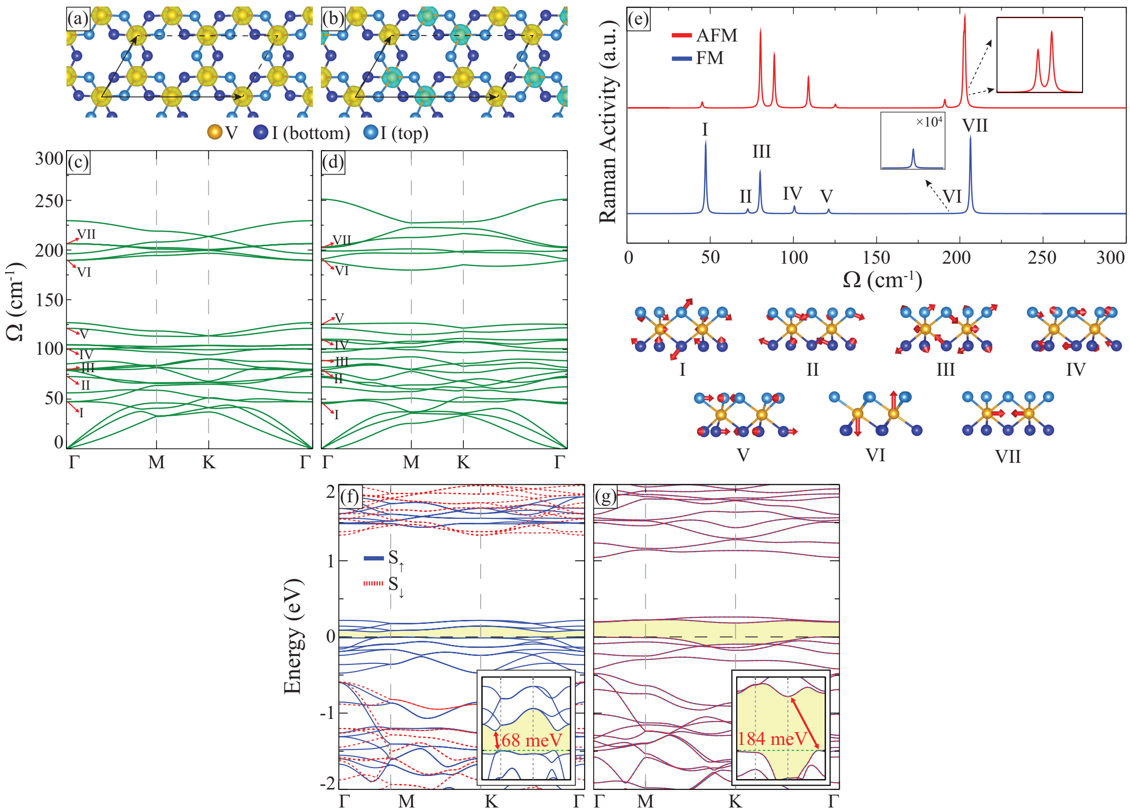

Figure 5.1. For the FM and AFM states of monolayer VI_3; (a, b) top view of the 2×1 supercell structure with charge density differences, (c, d) the phonon band dispersions, (e) corresponding Raman spectra with the vibrational character of prominent Raman active modes, and (f, g) electronic band dispersions. The insets show the band dispersions around the Fermi level which is set to zero. Up and down spin components are denoted by blue and red lines, respectively. Yellow and blue colors represent up and down magnetic moment, respectively. The isosurface level of charge density difference is set to 0.02 eV/Å^3. Adapted with permission from Ref.[20] Copyright 2019 Elsevier B. V .

In its primitive unitcell, monolayer VI_3 consists of 2-V and 6-I atoms where each V atom forms VI_6 octahedron with I atoms. As shown in Figs. 5.1(a) and (b), the edge-shared VI_6 octahedrons form a honeycomb network of V atoms with the space group of R$\overline{3}$ similar to the crystal structure of monolayer CrI_3.[164,165] Crystal structure of VI_3 displays slight structural differences in FM and AFM phases. As listed in Table 5.1, the lattice parameters are calculated to be 6.85 Å and 6.75 Å for the FM and AFM phases, respectively. V-I bond length is found to be 2.74 Å in FM phase, however, it is found to have three different values (2.69 Å, 2.74 Å, and 2.78 Å) in AFM state. Similarly, V-V atomic distance in FM phase is found to be 3.96 Å while in AFM phase two values are found, 3.60 Å between the V atoms with the same spin orientation and 4.05 Å for those having opposite spin orientations. According to the Bader charge analysis, each V atom donates 1.1 e^- to six I atoms in both magnetic phases. Total energy differences are calculated for both magnetic phases and FM phase is found to be energetically favorable. Cohesive energies of FM and AFM phases are calculated to be 3.08 eV and 3.07 eV per atom, respectively. In addition, work function of FM and AFM phases are found to be 5.23 eV and 5.18 eV, respectively. Compare to the work function of 2D magnetic semiconductor CrI_3, which is reported to be 5.35 eV,[166] VI_3 has lower work function.

Dynamical stability of monolayer VI_3 for two different magnetic states is investigated by calculating their phonon band dispersions through the whole BZ and are shown in Figs. 5.1(c) and (d). The phonon branches are found to be free from any imaginary frequencies indicating the dynamical stability of monolayer VI_3 at both FM and AFM states, respectively. Apparently, magnetic state of the structure can also be monitored via phonon band dispersions. Phonon frequencies and corresponding eigenfunctions are obtained at the Γ point in order to calculate the first-order off-resonant Raman spectrum for both magnetic states. The Raman spectrum calculations reveal that both FM and AFM monolayer VI_3 exhibit seven prominent Raman active modes which are shown below Fig. 5.1(e).

In order to compare the Raman active modes of both magnetic phases, phonon modes are labeled from I-to-VII as given in the inset of Fig. 5.1(e). The highest frequency optical modes, labeled as VI and VII, arise from the pure opposite out-of-plane and in-plane vibrations of V atoms, respectively. The phonon mode-VII is doubly-degenerate for FM state while a small splitting of 0.8 cm^{-1} is found in AFM state due to different

Table 5.1. Calculated parameters for AFM and FM phases of VI_3: magnetic state, optimized lattice constants, a=b; distance between V-I, d_{V-I}; and V-V atoms, d_{V-V}; total magnetic moment per primitive cell, μ; total amount of electron received per I atom, ρ_I; cohesive energy per atom, E_{Coh}; total energy difference per atom with respect to the ground state energy, ΔE; work function, Φ; and the energy band gap calculated within GGA, E_{gap}^{GGA}. Adapted with permission from Ref.[20] Copyright 2019 Elsevier B. V.

Magnetic state	a=b (Å)	d_{V-I} (Å)	d_{V-V} (Å)	μ (μ_B)	ρ_I (e^-)	E_{Coh} (eV)	ΔE (meV)	Φ (eV)	E_{gap}^{GGA} (meV)
FM	6.85	2.74	3.96	4	0.4	3.084	0	5.23	68
AFM	6.75	2.69-2.74-2.78	3.60-4.06	0	0.4	3.073	11	5.18	184

V-V distances. In both magnetic phases, mode-VII is found to be prominent, however, it displays a phonon softening as the magnetic phase is switched to AFM state (206.4 cm^{-1} for FM and 203.2-202.4 cm^{-1} for AFM state). Both the phonon shift and the phonon splittings can be observed in a Raman measurement in order to distinguish the magnetic state of the structure. In contrast, the phonon mode-VI is non-degenerate for both magnetic states and it is shown to be prominent only at AFM state. In addition, its frequency hardens from 189.7 cm^{-1} at FM state to 191.1 cm^{-1} at AFM state. Apparently, the change in the frequency of in-plane mode (mode-VII) is more significant than mode-VI due to the variation of V-V distance between two magnetic phases.

Another distinctive feature of Raman spectra can be seen for the modes labeled as IV and V. In both of the phonon modes, the vibrations are dominated by I atoms while V atoms have negligible contribution. The relative frequency shift of the two modes is found to be 20.6 and 16.2 cm^{-1} for FM and AFM states, respectively which is significant for their observation in a Raman measurement. In addition, the Raman activity ratio of mode-IV to that of mode-V is much greater for AFM state. In the low-frequency regime ($<$ 100 cm^{-1}), there are three prominent peaks labeled as I, II, and III. The modes I and III are attributed to the coupled in-plane and out-plane vibrations of I atoms while V atoms have small in-plane vibrations against each other. In contrast, in mode II only I atoms have coupled motion. The frequency of mode I is found to be 47.3 cm^{-1} at FM and 45.3 cm^{-1} at AFM states that the frequency difference is still observable. Moreover, the relative frequencies of the modes II and III are calculated to be 7.4 and 8.3 cm^{-1} for FM and AFM states, respectively. Apart from the phonon frequencies, the high Raman activities of the modes II and III in AFM state are distinctive features of AFM monolayer

VI_3. Overall, the calculated Raman activities and the frequencies of the phonon modes are found to be valuable for the identification of the magnetic state in monolayer VI_3.

The electronic properties of FM and AFM magnetic states in monolayer VI_3 are found to display semiconducting features with relatively different band gaps. As presented in Figs. 5.1(f) and (g), in the AFM state, monolayer VI_3 exhibits semiconducting behavior with a band gap of 184 meV for both spin components while the FM state is found to possess semiconducting character with band gap of 68 meV for one spin channel. In addition, in FM state the valence band maximum (VBM) and conduction band minimum (CBM) for one spin channel are located at different points in the BZ. The VBM and CBM are located in between the Γ and the M points resulting in an indirect band gap nature. In the case of AFM phase, VBM and CBM reside near the Γ and the K points, respectively in between the Γ-K path. Notably, the two magnetic states of monolayer VI_3 display semiconducting characteristic with 116 meV difference between their energy band gaps which may be useful for optically distinguishing the magnetic state of the structure.

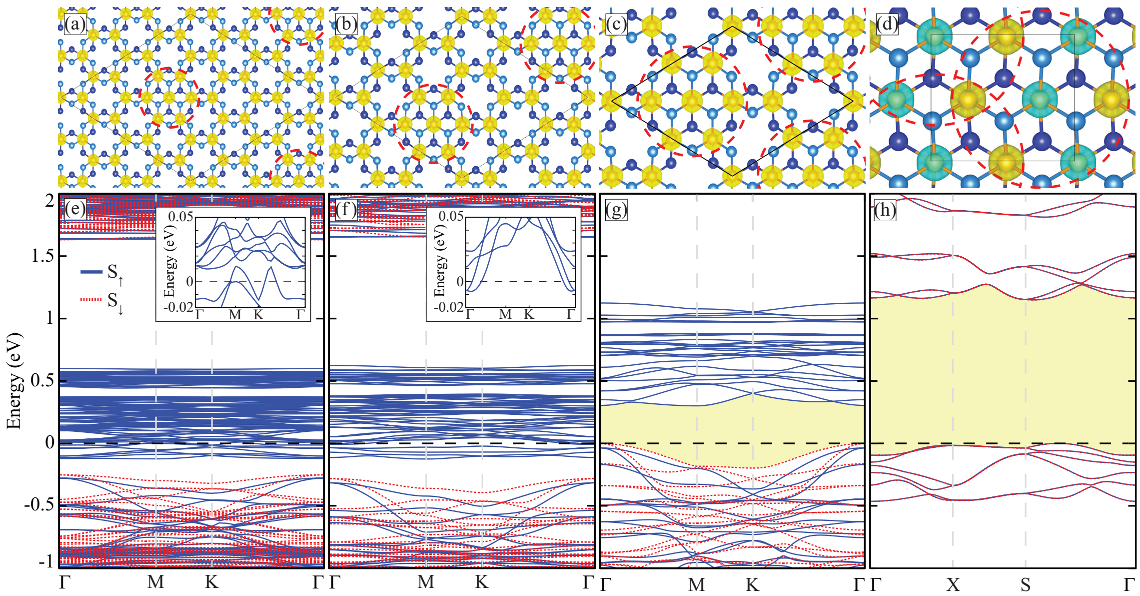

Figure 5.2. (Color online) (a,b,c,d) The spin polarized charge density differences (isosurface level is set to 0.02 eV/Å^3) for 1/16, 1/9, 1/4 , and fully-doped VI_3, respectively.(e,f,g,h) The corresponding electronic band dispersions, respectively. V doped regions are highlighted by red-dashed circles. Adapted with permission from Ref.[20] Copyright 2019 Elsevier B. V.

In a recent experimental study concerning 2D form of VI_3, it was reported that holes in the center of honeycomb networks of V atoms have tendency to be occuppied by excessive V atoms.[19] In order to clarify the effect of excessive V atoms on the properties of monolayer VI_3, 1/16, 1/9, 1/4, and fully-doped VI_3 structures are formed (see Figs. 5.2 (a), (b), (e), and (f)). Depending on the dopant level in monolayer VI_3, the atomic bond distances between V-I and V-V are found to vary due to structural changes.

As shown in Fig. 5.2, FM ground state of VI_3 is robust in partially-doped VI_3 structures, however, AFM state is found to be more favorable as the monolayer VI_3 is fully-doped. The structural transition from VI_3 to VI_2 has a significant effect on the magnetic ground state of the structure. The electronic band dispersions for each doped-VI_3 structures are presented in Figs. 5.2 (c), (d), (g), and (h). For the low dopant concentrations, i.e. for 1/16 and 1/9, structure exhibits half-metallic behavior in its ground state. As shown in Figs. 5.2(c) and (d), the direct and indirect energy band gaps for the semiconducting spin channels are calculated to be 1.98 and 1.92 eV for 1/16 and 1/9 doping levels, respectively. As the doping concentration increases to 1/4, structure turns into a semiconductor for both spin-channels (see Fig. 5.2(g)). The calculated band gaps are 0.34 and 2.01 eV for different spin components. In addition, the global band gap, 0.34 eV, is found to possess indirect nature. In the case of fully-doped structure (monolayer VI_2), the electronic bands are degenerate due to AFM ground state and the structure is an indirect band gap semiconductor with a band gap of 1.16 eV. It is seen that electronically monolayer VI_3 is found to exhibit semiconducting behavior at least for one spin-channel for different doping levels. In addition, the electronic band gap tunability via V doping (in a wide range of 0.34-1.98 eV) of monolayer VI_3 increases its importance in optoelectronic device applications.

5.2. Strain Engineering in Monolayer VI_3

Strain is a common effect which can occur in 2D materials either naturally or externally as a controllable tool for altering the electronic and magnetic properties of the material.[110,163] In addition, strain was reported to be a useful tool for switching the magnetic state of a material.[167,153] As in the case of doping, application of strain may affect magnetic and electronic properties of the magnetic monolayer materials. Here, the effect of biaxial strain on dynamical, electronic, and magnetic properties of VI_3 are investigated in accordance with V doping.

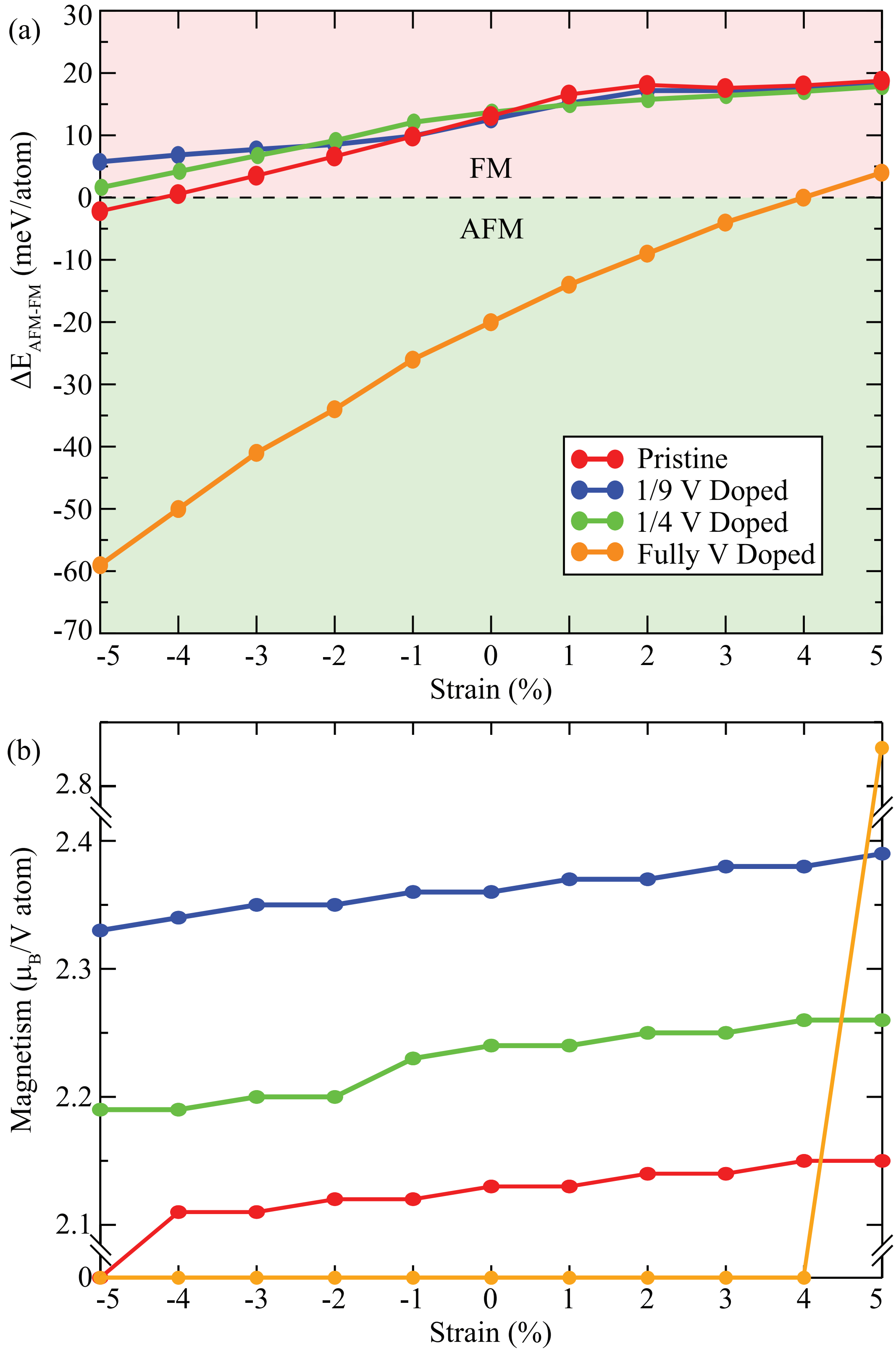

Figure 5.3. The effect of biaxial strain on the (a) total energy differences of FM and AFM states in pristine, 1/9 V doped, 1/4 V doped, and fully-doped VI_3. (b) magnetic moment per V atom in pristine, 1/9 V doped, 1/4 V doped, and fully-doped VI_3. Adapted with permission from Ref.[20] Copyright 2019 Elsevier B. V.

In the case of pristine, 1/9 doped, and 1/4 doped monolayer VI_3, the total energy differences per atom between FM and AFM states increase as the structures are biaxially stretched (see in Fig. 5.3 (a)), however, magnetic ground state remains as FM except for the pristine monolayer as the structure is biaxially compressed with strain strengths larger than 4%. At 5% of compressive strain, pristine monolayer VI_3 undergoes a FM-to-AFM magnetic phase transition. For the 1/4 and 1/9 doped structures, compressive biaxial strain results in decreasing of the energy difference between two magnetic states. Decreasing energy difference between FM and AFM phases indicates that under adequate compressive strain magnetic phase transition may occur, however, under such compression dynamical stability of doped VI_3 crystal is crucial. On the other hand, for the fully-doped monolayer VI_3, a magnetic phase transition from AFM-to-FM state occurs over 4% of tensile strain which is quite important for the control of magnetic state in doped-VI_3 structures with mechanical strain. In addition, effect of strain on magnetism of V atoms in pristine and doped structures are examined. Pristine, 1/4 and 1/9 doped structures are found to have lower magnetic moment under compressive strain and higher magnetic moment under tensile strain, as it is presented in Fig. 5.3 (b).

In order to investigate the dynamical stability of the structures under applied strain, the phonon band dispersions are calculated for pristine and fully-doped monolayer VI_3, at 5% of compressive and tensile strains and the results are presented in Supplementary Information. The phononic stability is found to be retained in both structures for FM and AFM magnetic states.

The effect of biaxial strain on electronic band dispersions of pristine, 1/9 V doped, 1/4 V doped, and fully-doped monolayer VI_3 are investigated and the results are presented in Figs. 5.4(a-h). In AFM phase of pristine VI_3 semiconducting behavior is found to be robust for both compressive and tensile strains while in FM phase transforms from semiconductor to half-metal under compressive strain. Under tensile strain, FM phase of pristine VI_3 retains its semiconducting property. 1/9 V doped VI_3 is found to be semiconductor in its AFM phase at strain-free structure and its band gap increases with increasing compressive strain while it decreases with increasing tensile strain. Importantly, FM 1/9 V doped structure undergoes half-metallic-to-semiconducting behavior with increasing tensile strain. The 1/4 doped monolayer VI_3 is found to display robust metallic nature via applied strain in its AFM state. Moreover, its FM structure exhibits robust semiconducting behavior with varying electronic band gap which increases with increasing tensile strain. However, its electronic band structure at 5% of compressive strain (see Fig. 5.4(e)) shows that the structure has tendency to possess transition to a metallic state over 5% of compressive strain. In the case of fully-doped monolayer VI_3, the band gap and semiconducting nature of AFM state are preserved while the magnetic state switches to FM over 4% of tensile strain with robust semiconducting behavior. Apparently, partially-doped VI_3 structures display robust magnetic phases under applied biaxial strain while pristine and fully-doped structures undergo magnetic phase transitions with robust semiconducting natures.

5.3. Conclusions

In this study, the dopant- and strain-dependent structural, magnetic, electronic, and vibrational properties of recently synthesized monolayer VI_3 were investigated in order to clarify the observations in the recent experiment. Total energy optimizations indicated that in its dynamically stable structure, monolayer VI_3 possesses FM, semiconducting ground state. The FM and AFM states of VI_3 were found to display distinctive vibrational features in their Raman spectra which is useful for distinguishing the magnetic phase. Our analysis on magnetic and electronic properties of the V-doped VI_3 structures revealed that as monolayer VI_3 is fully-doped by V atoms, it displays a structural phase transition to VI_2 which exhibits AFM semiconducting behavior with a relatively larger band gap in its ground state. Contrarily, for the doping levels in lower concentrations (1/16, 1/9, and 1/4) the FM state remains as the ground state with tunable electronic band gap depending on the doping level. Moreover, it was revealed that both pristine and fully-doped-VI_3 display phononic stability under applied tensile and compressive biaxial strains which is quite important for nanoelastic applications of monolayer VI_3. Notably, pristine and fully-doped VI_3 structures were shown to exhibit magnetic phase transitions under compressive and tensile strains, respectively. Further analysis on strain-dependent electronic band dispersions revealed that pristine and fully-doped VI_3 have robust electronic properties while partially-doped structures exhibit robust magnetic states with varying electronic properties.

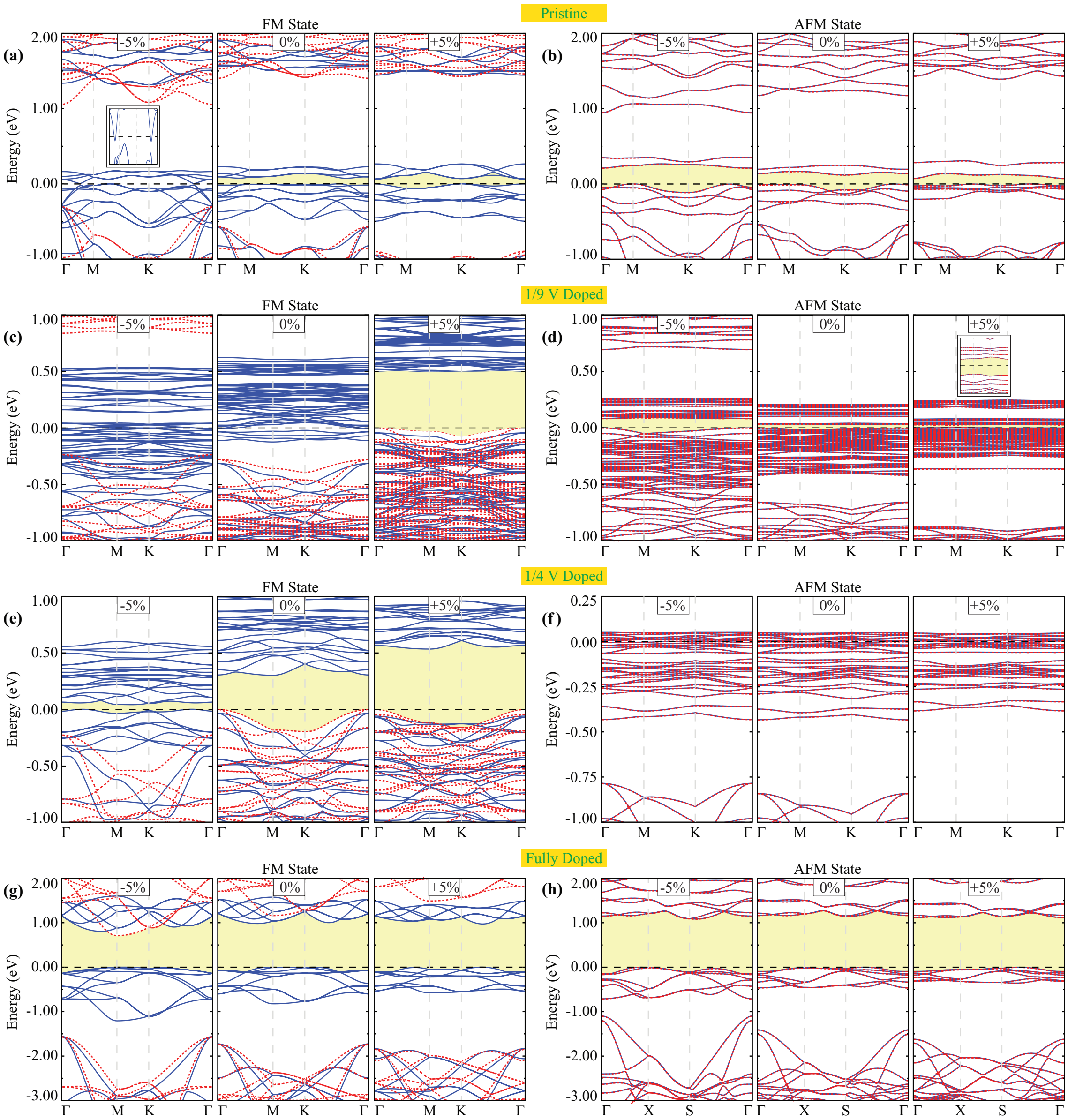

Figure 5.4. The strain-dependent electronic band dispersions of monolayer VI_3 for; (a) FM and (b) AFM pristine, (c) FM and (d) AFM 1/9 V doped, (e) FM and (f) AFM 1/4 V doped, (g) FM, and (h) AFM fully-doped structures. The insets show the strain dependent electronic band structures of 5% compressed FM pristine and 5% stretched AFM 1/9 doped VI_3 structures. Adapted with permission from Ref.[20] Copyright 2019 Elsevier B. V.

CHAPTER 6

ULTRA THIN STRUCTURES OF MANGANESE FLUORIDES: CONVERSION FROM MANGANESE DICHALCOGENIDES BY FLUORINATION

Various experimental methods have been used in the last two decades in order to synthesize two-dimensional (2D) ultra-thin materials. Among those methods, micromechanical cleavage has been reported to be a simple and effective method for obtaining monolayers of layered bulk crystals via exfoliation using an adhesive tape.[168,169,170] In addition, chemical vapor deposition (CVD) and molecular beam epitaxy (MBE) techniques have often been used in order to produce large-scale, high-quality ultra-thin structures. However, these procedures are much less cost-effective, often intricate, and expensive.[171,172,173,174,175] Therefore, due to its simplicity micromechanical cleavage has been still widely used with the required improvements made for obtaining large-scale flakes.[176] Although it is a widely-used method, application of cleavage technique has been limited to crystal structures composed of van der Waals (vdW) coupled layers, and therefore, synthesis of 2D crystals from non-layered bulk structures is an important issue. Very recently, we demonstrated a novel method for the synthesis of 2D ultra-thin structures from non-layered bulk materials using the chemical conversion process.[177] It was demonstrated that for sufficiently long fluorination time, layered InSe can be turned into a thin InF_3 crystal in which all Se atoms are chemically exchanged with F atoms. Studies on chemically converted ultra-thin crystal structures are still continuing.

Among the fluoride crystals, manganese fluorides having diverse phases have been widely used in various applications. MnF_4 is known as a powerful oxidizing agent with blue-violet color and is synthesized via the reaction of MnF_3 with HF.[178] It was demonstrated that MnF_3 is an effective fluorination agent which is used to convert hydrocarbons into fluorocarbons.[179] It was also reported that MnF_3 is a spin-polarized Dirac material[180] exhibiting the Jahn-Teller type distortion.[181] On the other hand, MnF_2 has also been used as an anode material in lithium-ion battery[182,183] and glass applications.[184,185] Short luminescence[186] and two-color photoluminescense[187] features of MnF_2 were also reported.

Although, thin-films of manganese fluoride crystals have been studied, their ultra-thin two-dimensional structures have not been reported yet.

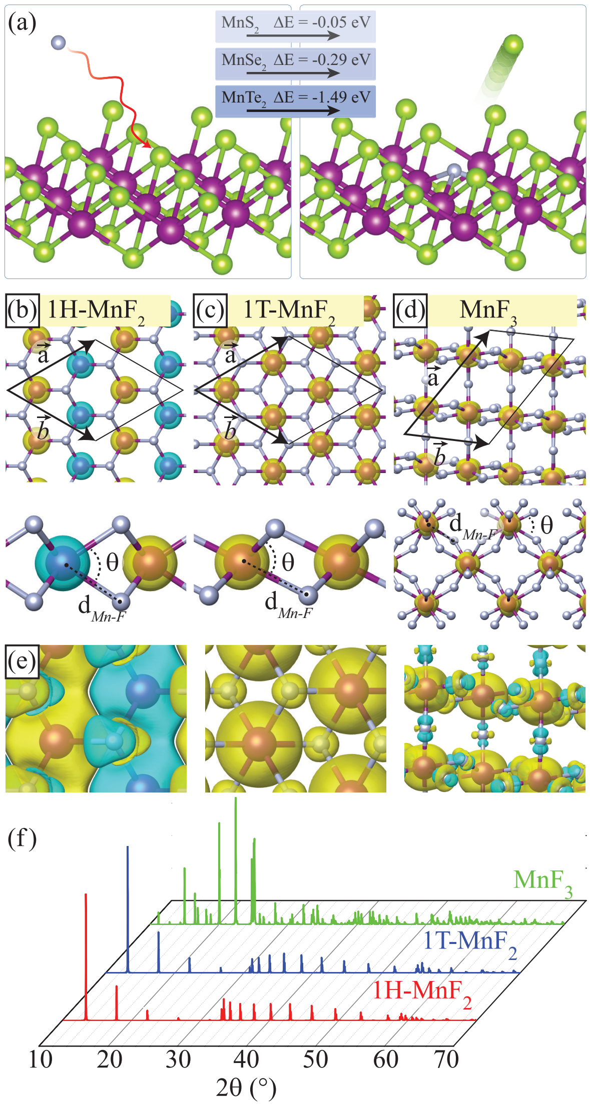

Figure 6.1. (a) Schematic of the fluorination process of $MnSe_2$ monolayer with the energy difference of corresponding states given in the inset. Crystal structures with difference charge densities of (b) 1H-MnF_2, (c) 1T-MnF_2, and (d) MnF_3. (e) Superexchange interactions and (f) corresponding XRD spectra of single-layer MnF_x structures represented by red, blue and green lines, respectively. Purple, green, and violet colored atoms represent Mn, chalchogen (S, Se, Te), and F atoms, respectively.

In this study, we propose the formation of different MnF_x single-layers that can be obtained through fluorination of manganese dichalcogenide structures. Our first-principles calculations reveal that the chemical exchange of F-chalcogen is energetically favorable and 1H and 1T phases of MnF_2 are formed as dynamically stable, magnetic semicon-

Table 6.1. Calculated parameters for single-layer MnF_xs: optimized in-plane lattice constants (a and b), bond length between Mn and F (d_{Mn-F}), the F-Mn-F bond angle (θ), magnetic ground state of the structure, in-plane stiffness (C_x and C_y), the Poisson ratio (ν_x and ν_y), donated electron per Mn (ρ_{Mn}), cohesive energy per atom (E_c), workfunction (Φ), energy band gaps calculated within GGA (E_{gap}^{GGA}), Raman active modes.

	a (Å)	b (Å)	θ (°)	Mag. State	C_x , C_y (N/m)	ν_x , ν_y	ρ_{Mn} (e^-)	E_c (eV)	Φ (eV)	E_{gap}^{GGA} (eV)	R-Active Modes (cm^{-1})
1H-MnF_2	6.26	6.26	67	AFM	57 , 57	0.24 , 0.24	1.5	4.31	8.54	3.82	245, 418, 447
1T-MnF_2	6.71	6.71	79	FM	47 , 47	0.34 , 0.34	1.6	4.52	6.96	3.67	253, 325
MnF_3	8.53	5.38	84-92	FM	40 , 49	-0.46 , -0.57	2.0	3.86	9.48	0.47	437, 482, 674, 1221

ductors. In addition, ultra-thin MnF_3 is shown to be a stable magnetic semiconductor exhibiting different atomic compositions. Electronic band structure calculations indicate the formation of semiconducting MnF_xs which also exhibit distinctive vibrational properties. Thus, the chemical conversion of layered materials through fluorination can be an efficient way to obtain 2D forms of non-layered materials.

6.1. Fluorination and Atomic Structure

Manganese dichalcogenides, MnX_2 (X=S, Se, or Te) are known to be dynamically stable, with magnetic single-layers which exhibit layered crystal structure in their bulk forms. However, the metallic nature of MnS_2, $MnSe_2$, and $MnTe_2$ limits their use in optoelectronic device applications.[188,18,189] As previously achieved in InSe,[177] one can expect that the chemical conversion of these ultra-thin crystals can lead to the formation of manganese-based novel structures with new functionalities.

The schematic representation of fluorination of MnX_2 by single fluorine atoms is shown in Figure 6.1(a). Our results show that the chemical substitution of a chalcogenide atom by a F atom is energetically feasible with calculated exchange energies of -0.05, -0.29, and -1.49 eV for S, Se, and Te, respectively. Following the investigation of the energetics of single F exchange in single-layer MnX_2 structures, formation of possible MnF_2 phases with different compositions, namely 1H-MnF_2, 1T-MnF_2, and MnF_3, are examined.

Total energy optimization calculations show that single-layer MnF_2 structures can be crystallized either in 1H or 1T phases. In both phases, the Mn layer is sandwiched between two F layers, exhibiting P6/m2 and P3/m2 space-group symmetries, respectively. On the other hand, single-layer MnF_3 is formed such that the Mn atoms are surrounded by bi-pyramidal tetrahedrally oriented F atoms in an accordion-like confirmation. It is calculated that in these crystal structures each Mn atom has 5 μ_B net magnetic moment. While antiferromagnetic (AFM) order is favorable for 1H phase, 1T phase favors ferromagnetic (FM) order. In addition, FM ordered state is also ground state for MnF_3 (with 4 and 3 μ_B net magnetic moment per inner and outer Mn atoms, respectively). As shown in Figure 6.1 AFM (FM) order of Mn atoms in 1H-MnF_2 phase (in 1T-MnF_2 and MnF_3 phases) is stabilized by superexchange interaction provided by fluorine atoms. In addition, cohesive energies of 1H-MnF_2, 1T-MnF_2 and MnF_3 are calculated to be 4.31, 4.52 and 3.86 eV/atom, respectively. It appears that though cohesive energies of predicted single-layers are less energetically favorable than their bulk forms (4.93 and 4.56 for MnF_2 and MnF_3, respectively), their synthesis is feasible through fluorination of ultra-thin manganese dichalcogenides.

6.2. Mechanical and Vibrational Properties

Linear-elastic properties of MnF_x single-layers are also determined in terms of the in-plane stiffness, and Poisson ratio. In-plane stiffness, $C_{x(y)}$, is the rigidity of a material while Poisson ratio, $\nu_{x(y)}$, is the ratio of transverse contraction strain to longitudinal extension. In order to determine the elastic properties of the MnF_x single-layers, elastic strain tensor elements, C_{ij} are calculated. In-plane stiffness and Poisson ratio are calculated by using the formula;

$$C_{x(y)} = \frac{(C_{11}C_{22} - C_{12} \times C_{21})}{C_{22(11)}}, \tag{6.1}$$

$$\nu_{x(y)} = \frac{C_{12}}{C_{22(11)}} \tag{6.2}$$

In-plane stiffness values are calculated as 57 N/m for 1H-MnF_2, and 47 N/m for 1T-MnF_2. In the case of MnF_3, an in-plane anisotropy in x and y directions is predicted where the C_x and C_y values are found to be 40 and 49 N/m, respectively. As compared to the elastic constants of well-known single-layers such as graphene (330 N/m),[137,110]

MoS_2 (122 N/m),[137,110] h-BN (273 N/m),[137,110] and WS_2 (122 N/m),[110] in-plane stiffness values of MnF_x single-layers indicate their ultra-soft nature. On the other hand, negative Poisson ratio values of the MnF_3 (ν_x= -0.46, ν_x= -0.57) single-layer indicate its the auxetic nature. Therefore, differing from 1H and 1T structures, single-layer of MnF_3 is expected to undergo lateral expansion when stretched longitudinally and become thinner when compressed laterally.

Dynamical stability and vibrational properties of the predicted MnF_x structures are investigated in terms of their phonon band dispersions and Raman activity spectra. As presented in Figure 6.2, 1H-MnF_2, 1T-MnF_2, and MnF_3 single-layers have phonon branches all having positive eigenfrequencies in the whole Brillouin zone and therefore, they are dynamically stable in free-standing form. 1H and 1T MnF_2 are found to exhibit six optical phonon branches two of which arise from the non-degenerate out-of-plane vibration of the atoms. The remaining four branches stand for in-plane vibrational motions. In the case of 1H-MnF_2, three existing Raman active modes which are named as A_1, E', and E'' are shown in Figure 6.2. The A_1 mode represents the vibration of only F atoms against each other in the out-of-plane direction while the E' mode stands for the in-plane vibration of Mn and F atoms against each other. In addition, E'' mode arises from the opposite in-plane vibration of F atoms. On the other hand, 1T-MnF_2 exhibits two Raman active modes, namely A_{1g} and E_g. A_{1g} denotes the opposite vibration of F atoms in the out-of-plane direction while E_g represents the vibrations of F atoms against each other in the lateral directions. In the case of single-layer MnF_3, the prominent peaks in the Raman spectrum are located at 437, 482, 674, and 1221 cm^{-1} in its magnetic ground state. The most intense peak at frequency 437 cm^{-1} is attributed to the coupled in-plane and out-of-plane vibration of F atoms in the inner MnF_6 units while the other three Raman modes are dominated by the F vibrations in the outer MnF_6. While the modes at 482 and 674 cm^{-1} arise from the coupled in-plane and out-of-plane vibrations, the mode having frequency 1221 cm^{-1} is dominated by the out-of-plane vibration of the F atoms in outer MnF_6 units. Raman activity calculations, shown in lower panel of Figure 6.2, reveal that for each predicted MnF_x single layer structure there are distinctive Raman-active phonon peaks and therefore, these crystal structures can be distinguished by Raman spectroscopy.

In addition to the dynamical stability, thermal stability of manganese fluoride single-layers at room temperature are investigated by molecular dynamics simulations.

Simulations are carried out for $\sim$2ps with 2fs difference between consequent steps. It is revealed that, while 1T-MnF_2 and MnF_3 retain their stable phase, deformation occurs in the 1H-MnF_3 lattice.

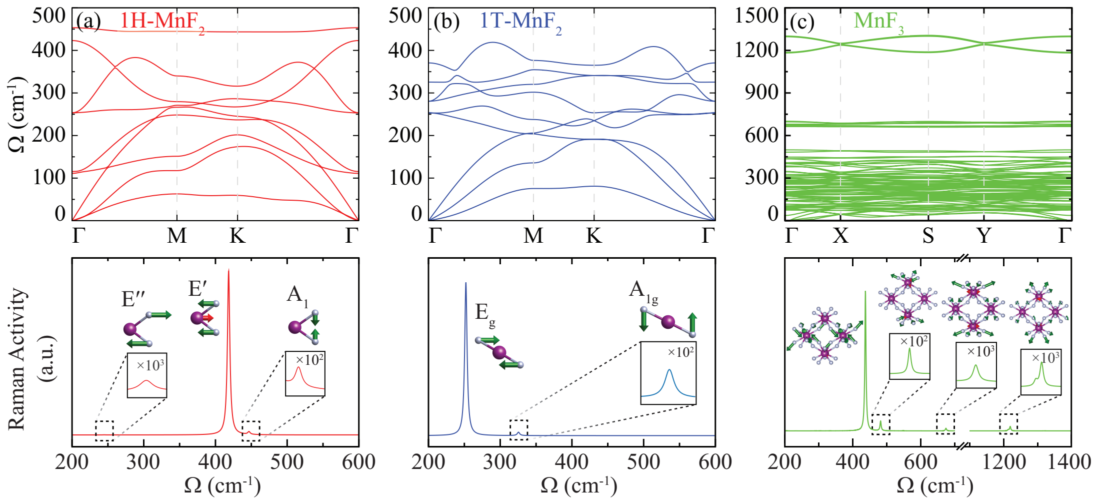

Figure 6.2. Phonon dispersions and corresponding Raman spectrum of (a) 1H-MnF_2, (b) 1T-MnF_2, and (c) MnF_3.

In addition to the dynamical stability, thermal stability of manganese fluoride single-layers at room temperature are investigated by molecular dynamics simulations. Simulations are carried out for $\sim$2ps with 2fs difference between consequent steps. It is revealed that, while 1T-MnF_2 and MnF_3 retain their stable phase, deformation in the 1H-MnF_3 lattice are determined.

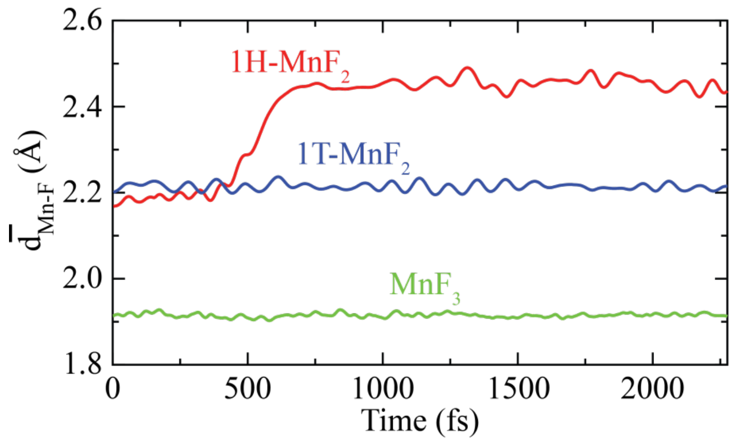

Figure 6.3. Average bond lengths of 1H-MnF_2, 1T-MnF_2, and MnF_3 during the molecular dynamics simulation.

6.3. Electronic Band Structure and Possible van der Waals Heterostructures

Electronic properties of the 2D MnF_x crystals are investigated through their electronic band structures. In contrast to manganese based dicalcogenide single-layers having metallic character, MnF_x single-layers are semiconductors with varying band gaps (see Figure 6.4). 1H-MnF_2 is found to be an indirect band gap semiconductor with a band gap of 3.15 eV. The valence band maximum (VBM) and the conduction band minimum (CBM) are located at the Γ-M interval and the Γ points, respectively. In contrast, 1T-MnF_2 has a direct band gap character whose VBM and CBM are located at the Γ point with a band gap of 3.67 eV. In addition, single-layer MnF_3 is an indirect band gap semiconductor that has a band gap (0.47 eV) much smaller than those of the MnF_2 structures. Its VBM and CBM reside at the Γ and X-S points, respectively. In all three single-layers, the edge of the VBM states is composed of Mn-*d* and F-*p* orbitals while the CBM state are dominated by the Mn-*d* orbitals.

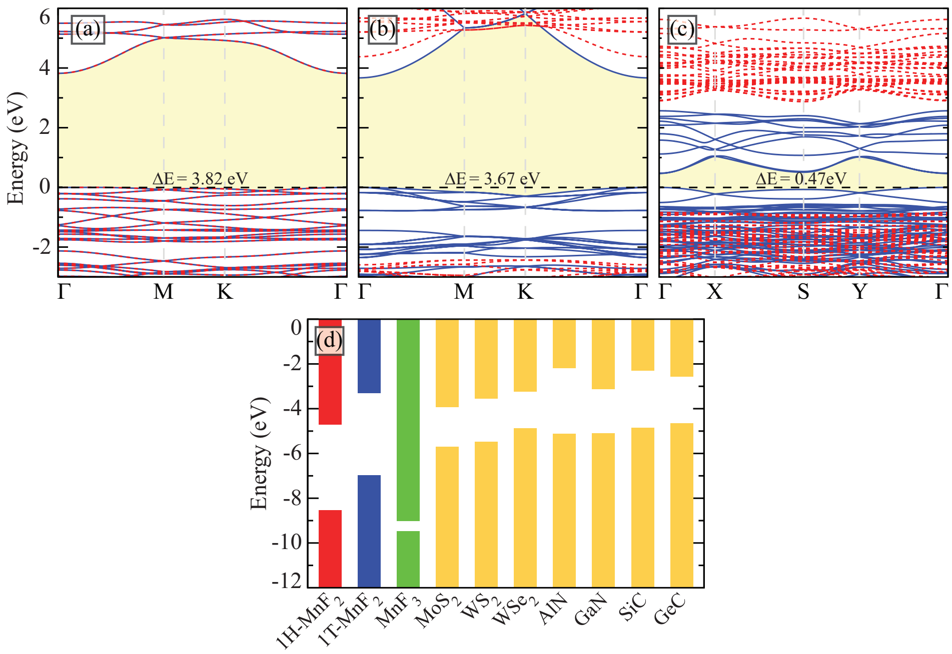

Figure 6.4. Electronic band structure of (a) 1H-MnF_2, (b) 1T-MnF_2, and (c) MnF_3. Major and minor spin components are represented by solid blue and red lines, respectively. (d) Band alignments of ultra-thin MnF_x structures and other reported single-layers. HSE06 bands are presented by dashed green and cyan lines for major and minor spin components, respectively.

Here, we also investigate the possible heterojunctions of the ultra-thin manganese fluorides with reported single-layers such as MoS_2, WS_2, WSe_2, AlN, GaN, SiC, and GeC.[188,107] Our results show that 1H-MnF_2 has lattice-mismatch of less than 1% with MoS_2, WS_2, and AlN while mismatch of 4% is calculated for GaN and GeC, and 5% for WSe_2. 1T-MnF_2 has lattice-mismatch of 5%, 5%, 2%, 6%, 3%, 7%, and 2% with MoS_2, WS_2, WSe_2, AlN, GaN, SiC, GeC, respectively. Comparative band alignments of these heterojunctions are presented in Figure 6.4(d). According to the results, 1H-MnF_2 forms type-I heterojunction with MoS_2, WS_2, WSe_2, AlN, GaN, and SiC while it forms type-III heterojunction with GeC. Type-II heterojunction is also predicted between 1T-MnF_2 and WSe_2, AlN, GaN, SiC. Additionally, 1T-MnF_2 forms type-II heterojunction with GeC and type-I heterojunction with MoS_2 and WS_2 single-layers. Apparently, formation of all three types of heterojunctions are possible with magnetic MnF_2 single layers, therefore these materials are expected to be used in various optoelectronic device applications. In the case of MnF_3, type-III heterojuction with the given materials is predicted. However, due to high lattice mismatch between these single-layers and ultra-thin MnF_3, heterojunction formation is not feasible.

6.4. Conclusions

In this study, we have investigated possible manganese fluoride crystals that can be obtained by fluorination of manganese dichalcogenides. Firstly, it is predicted that, similar to that recently performed for conversion of InSe crystals,[177] it is quite possible for the chalcogen atoms of the host lattice to be replaced by fluorine atoms. Total energy optimization and dynamic stability calculations have shown that formation of three novel ultra-thin crystalline manganese fluoride structures is feasible by chemical conversion. It is also revealed by *ab-initio* calculations that these stable ultra-thin crystal structures can form type-I, type-II, and type-III heterojunctions with other ultra-thin materials that have been studied in the literature. Notably, manganese fluorides which do not have ultra-thin phases can be obtained indirectly by fluorination of manganese chalcogenides and this appears to be an effective alternative method for synthesis of new materials needed in rapidly advancing nanotechnology studies.

CHAPTER 7

PREVALENCE OF OXYGEN DEFECTS IN AN IN-PLANE ANISOTROPIC TRANSITION METAL DICHALCOGENIDE

ReS_2 is a valuable member of transition metal dichalcogenides. Ultrathin form of ReS_2 previously investigated.[190] In addition, ReS_2 is experimentally obtained and reported to be stable under ambient conditions, with distorted 1T structure that corresponds to P1 space group,[191,192] which allows tunability in its electronic,[35,193] optical,[194,195,196,197] andmechanical[198] properties. Re atoms advocates the existence of metallic Re-Re bonds with the additional d electron, results in Re-Re chains within the lattice, as displayed in Figure 7.1(a). Re-Re chains in ReS_2 are reported to be observed by visualized by X-ray spectroscopy,[191,199] electron microscopy,[200] and early scanning probe microscopies.[201,202,203] Rhenium chains are reported to be useful in order to determine the orientation of crystal in device applications.[35,204] Although ReS_2 is widely studied, the number of studies concerning the visualization of defects present in the lattice is low. As in other 2D materials, defects in ReS_2 lattice occurs, and it is important to examine.

Synthesis of 2D materials are carried out various methods. Although some offer better quality results, still defect formation is inevitable. Defects such as vacancies, adsorption or absorption of impurities are reported in 2D materials such as graphene and TMDs.[205,206,207,208] Defects can alter the electronic properties of materials which may result in various effects.[209,210,211,212,213] Therefore, in order to increase the performance of optoelectronic devices constructed of TMDs, it is important to understand the nature and effects of these defects. Surface defects of bulk TMDs are visualized via various imaging techniques.[214,215,200] However, not being able to correlate the properties of impurities is still a drawback. Scanning tunnel microscopy and spectroscopy (STM/STS) is a valuable method in investigation of TMDs such as ReS_2. In addition to the STM/STS imaging, examining the correlation with the density functional theory results can be beneficial in order to determine the properties of defects.

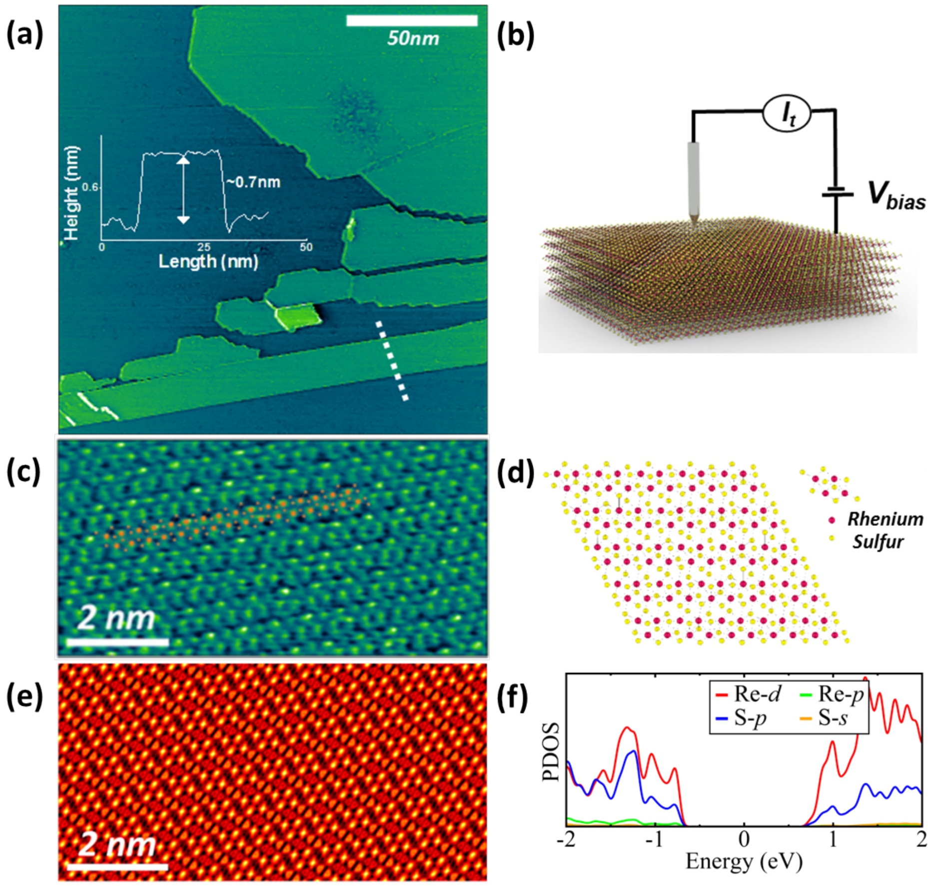

Figure 7.1. (a) STM topographic map of step edges on the surface of a ReS_2 crystal (V_b = −1.60V; I_T = 450pA). Inset: Height profile along the white dotted line. (b) Schematic of the STM experiment. (c) STM topographic image highlighting the Re chains with a spheres model as a guide to the eye. (d) Top and side view of the ReS_2 structure. (e) Simulated STM image of the ReS_2 lattice. (f) Calculated PDOS of monolayer ReS_2. Adapted with permission from Ref.[216] Copyright 2020 by the American Physical Society.

Here, combination of STM/STS images and first-principles calculations are used to determine the structural, and electronic properties of pristine and defected structures of ReS_2. In Figure 7.1 (a) STM/STS setup is illustrated. High resolution images of ReS_2 crystals are obtained from STM analysis, presented in Figure 7.1 (c). For accurate interpretation of STM analysis, local density of states (LDOS) must be taken into account. Therefore the partial density of states (PDOS) at the surface layer must be considered. The PDOS is calculated using ab-inito theory and presented in Figure 7.1(f). Re atoms dominate the PDOS with their *d* orbitals. Although, *p* orbitals of S atoms show effect in the PDOS, brighter atoms seen in STM images are Re atoms due to their *d* orbitals involving in the tunneling process. The simulated STM image of the pristine structure further confirms this concept (see Figure 7.1(e))

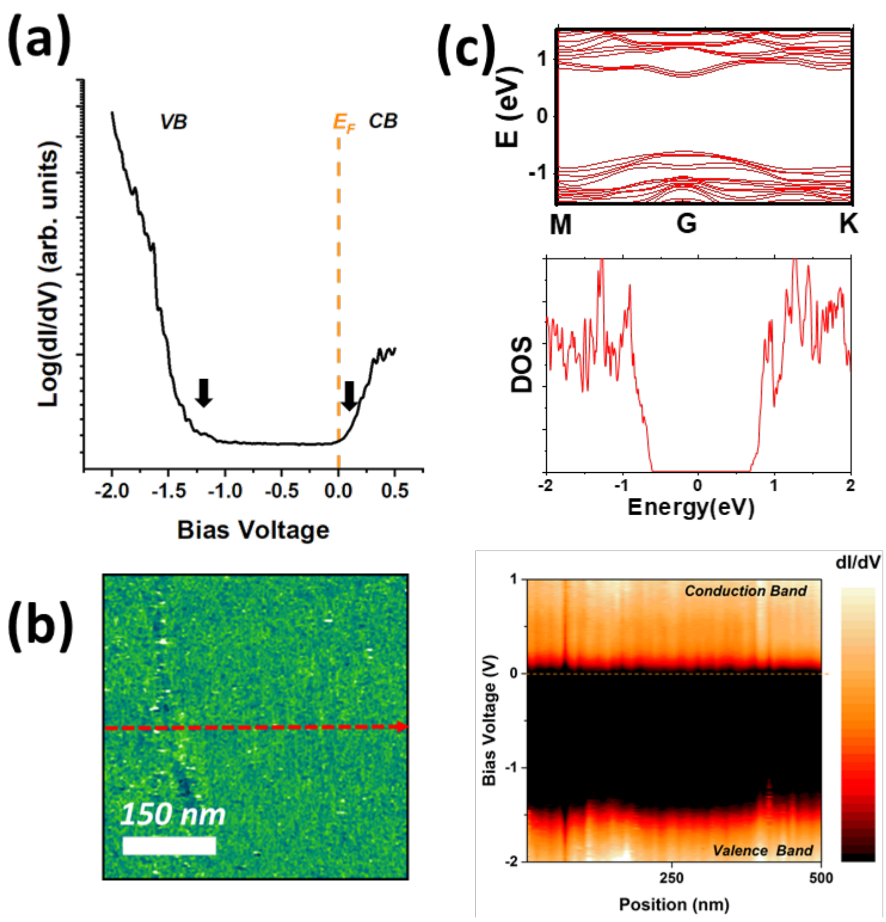

Figure 7.2. (a) Scanning tunneling spectroscopy averaged on the surface of ReS_2 . The logarithmic scale was used to highlight valence band (VB) and conduction band (CB) whose band edges relative to the Fermi level (E_F) are also indicated by arrows. (b) Right: line map of the scanning tunneling spectrum across the dashed line indicated in the topographic image in the left (V_b = -1.00 V; I_T = 65 pA. (c) Band structure of three-layer ReS_2 and the corresponding DOS. Adapted with permission from Ref.[216] Copyright 2020 by the American Physical Society.

Electronically, ReS_2 is a semiconductor, however, the nature of the semiconducting gap (direct or indirect) in the bulk versus monolayers remains a subject of discussion both experimentally and theoretically.[200,217,218,219,220,221,222,223,224] A number of experimental techniques including optical spectroscopies and electronic transport found the bulk band gap to be in the range of 1.40 ± 0.07 eV,[200,225,190,35,226] in agreement with results of theoretical calculations which reported the band gap to be in the range of 1.4 $\pm$ 0.1 eV.[200,227,228,193,194,219,220,221,222,223,224] However, transport and optical spectroscopy are macroscopic measurements which average over large areas of a crystal. Here, we use a local probe, scanning tunneling microscopy, and spectroscopy to measure the density of states on the surface of ReS_2 crystals. We find that the differential conductance, in Figure 7.2(a), shows the presence of an energy gap confirming the semiconducting nature of ReS_2. The extracted value of the energy gap is 1.35 ± 0.1 eV, agreeing with previous experiments. We note that this spectrum, Figure 7.2(a), represents averages over different samples, areas, and tips as detailed in the Supplemental Material,[216] and it is plotted on a logarithmic scale[229] for clarity. In Figure 7.2(b) we show the spatial variation of the spectrum across the device-size area, topographically presented in the left panel by plotting the scanning tunneling spectra across the dashed line (right panel). Within our resolution, the variation of the energy gap is less than 0.1 eV. These experimental findings are now compared with our theoretical calculations. In Figure 7.2(c) we show the band structure and corresponding DOS of a slab of ReS_2 consisting of three layers with details of calculations in the Supplemental Material.[216] The calculations show a gap at the Γ point, and from the corresponding DOS we can estimate the energy gap around E_{gap} = 1.3 eV, in good agreement with the measured semiconducting energy gap. While the density functional theory (DFT) gap appears to be in good agreement with the measured semiconducting energy gap, we note that DFT underestimates the energy gap. Inclusion of many-body corrections at the G_0W_0 quasiparticle level increases the band gap to 2.3 eV. However, we note that the blueshift of quasiparticle transition energies is partially compensated by excitonic effects which reduces the optical gaps to values often consistent with DFT band gaps. In a STS measurement, the zero bias corresponds to the Fermi level (E_F) as indicated by the dashed line in Figure 7.2(a). In an electrically neutral ReS_2, we expect the position of E_F to be in the middle of the semiconducting gap. However, in our samples we find the position of E_F to be close to the bottom of the conduction band (E_C), indicating the crystal is n doped.

We now turn to the analysis of dopants and defects. When imaging the surface of the ReS_2 crystal, we encounter "bright" or "dark" regions representing the presence of a dopant or defect that will electrostatically interact with its environment. Such features have been previously reported on surfaces of doped III-V semiconductors,[230] topological insulators [44], transition metal dichalcogenides,[231,232] BP,[233,234] or BN[235] Figure 7.3(b). The most common type of defects are shown in the STM topographic image of Figure

7.3(a). They have a characteristic bright center with a dark halo when imaged at negative bias voltages [Figure 7.3(b)]. As we vary the scanning parameters, we observe that the apparent height of the defects changes, so that they appear bright at negative bias voltages and dark at positive bias voltages. This is demonstrated in Figure 7.3(c) where we present STM topographic images taken at different bias voltages: -0.80 and +0.80 V respectively. The spectroscopic data acquired on the center of the defects, presented in Figure 7.3(d) as an average over 22 defects and in the Supplemental Material[216] on only one defect, closely resemble the one on a defect-free area, and reveal the absence of in-gap states. The slight increase in DOS within the gap in Figure 7.3(d) could be due to buried defects under the surface, as previously seen in other TMDs.[236]

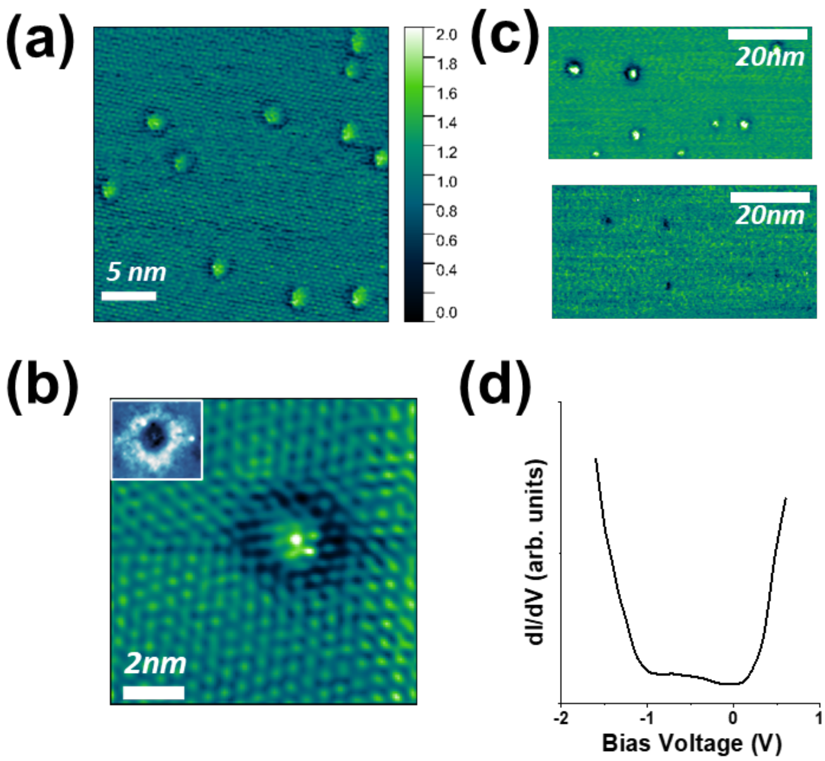

Figure 7.3. (a) STM topographic image (V_b = -1.20 V; I_T = 80 pA) showing lattice defects. (b) Topographic high-resolution image across a defect. Inset: LDOS map across a defect at VB = -1.2 V and I_T = 35 pA. (c) STM topographic images (I_T = 50 pA) of an area at different bias voltages. Top: V_{bias} = -0.80 V; bottom: V_{bias} = +0.80V. (d) Averaged STS measured on 22 defects such as the one in (b). Adapted with permission from Ref.[216] Copyright 2020 by the American Physical Society.

To complement our STM/STS data, we performed X-ray Photoelectron Spectroscopy (XPS) analysis of the crystal and, in addition to the expected Re and S,[237,238] we also find the presence of oxygen (see Figure 7.4).

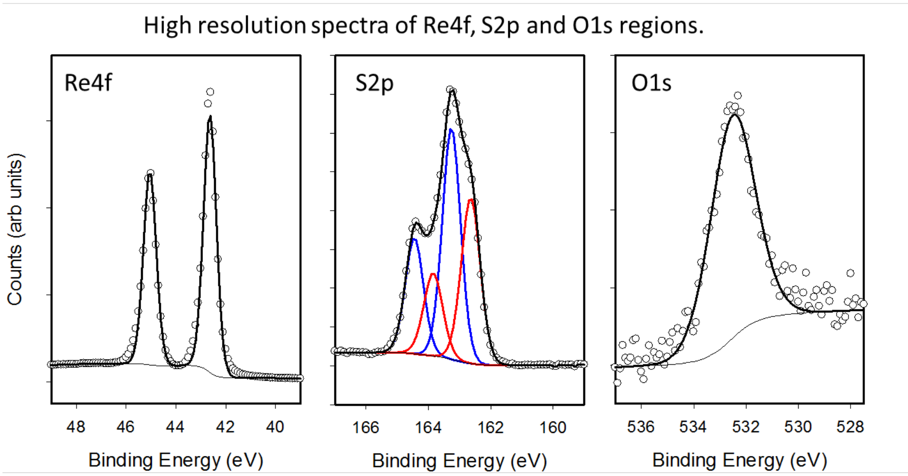

Figure 7.4. XPS results confirming that oxygen is contained in defected ReS_2 lattice. Adapted with permission from Ref.[216] Copyright 2020 by the American Physical Society.

Different possible atomic scale defects in the lattice of ReS_2 can have signatures in an STM experiment. For example, defects, such as a single atom vacancy, single atom adsorption, antisite formation where the S atom is substituted by the Re atom or vice versa, can be formed during the growth of two-dimensional (2D) ReS_2 sheets. To elucidate the possible origins of the most common defects observed in our STM experiments on the surface of ReS_2 we used DFT calculations. Simulated STM images of pristine ReS_2 and defected structures, together with their characteristic density of states, are presented in Figure 7.5. The formation of such defects results in dangling bonds within the lattice, which are readily oxygenated under atmospheric conditions, leading to O atom absorption by vacancies within the lattice. In fact, our theoretical results show that oxygen absorption by an S vacancy, as presented in 7.5(b), will create signatures in the density-of-states maps that closely resemble the measured defects, with a distinctive halo structure. Moreover, when we examine the density of states, a S vacancy results in midgap states [red curve in 7.5(c)], while when an O atom is bound to the S vacancy, the semiconducting band gap changes only slightly, in agreement with our experimental finding from STS presented in 7.3(e), strengthening the case for oxygen being a common defect in the ReS_2 layers. These results are also consistent with the reports that oxygen is a source of atomicscale defects in MoS_2.[214,215]

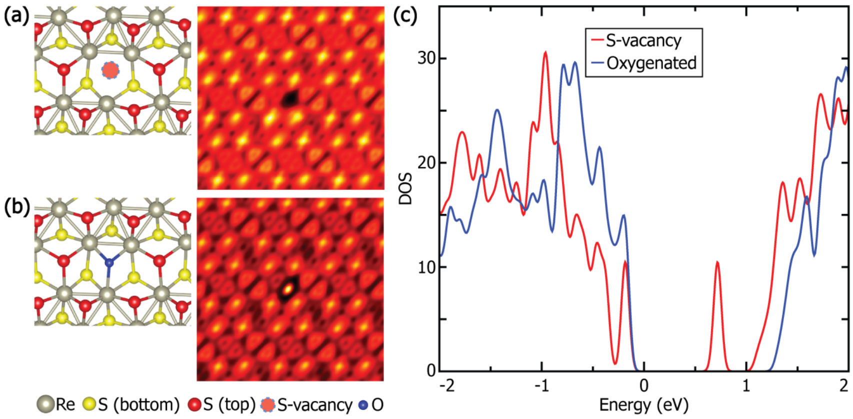

Figure 7.5. Crystal structure and simulated STM images of (a) S vacancy and (b) O absorbed by S vacancy. (c) LDOS of S vacancy and O absorbed by S vacancy. Adapted with permission from Ref.[216] Copyright 2020 by the American Physical Society.

In addition to the defects presented in 7.3, less frequent types of defects are also investigated and presented in Figure 7.6.

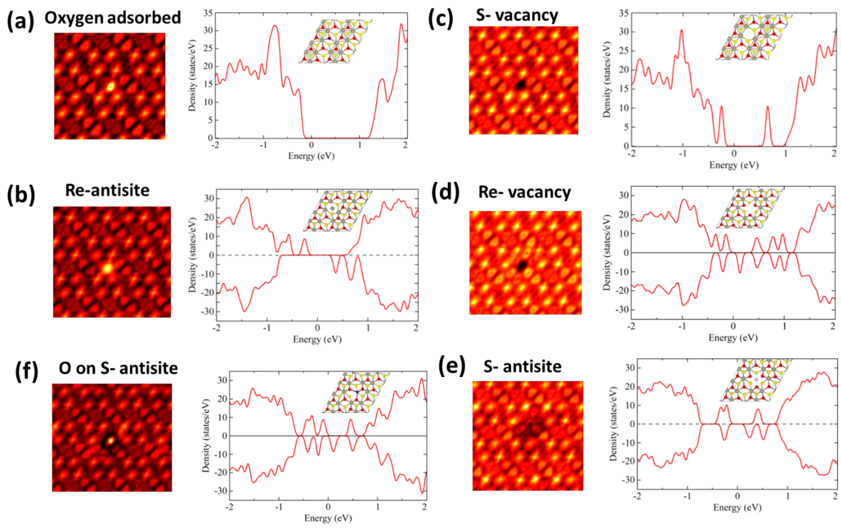

Figure 7.6. Simulated STM images and density of states of (a) O adsorbed, (b) S-vacancy, (c) Re-antisite, (d) Re-vacancy, (e) S-antisite, (f) O adsorption on S-antisite. Adapted with permission from Ref.[216] Copyright 2020 by the American Physical Society.

In conclusion, STM/STS measurements and first-principles calculations were carried out to examine the lattice structure, electronic band gap, and defects of ReS_2. It is shown that Re atoms form diamond-shaped chains in ReS_2 ultrathin crystals. Semiconducting bad gap is confirmed by both experimental measurements and DFT calculations.Additionally, presence of local lattice defects and their properties are explored. Comparison of the experimental STM/STS images with simulated STM images reveal frequent oxygen absorption by the defect sites. Results bring explanation towards understanding and engineering properties of in-plane anisotropic 2D semiconductors

CHAPTER 8

CHEMICAL VAPOR DEPOSITED GRAPHENE BASED SELECTIVE GAS SENSOR FOR DETECTION OF METHANOL IN ETHANOL-METHANOL GAS MIXTURE

Selective detection of volatile organic compounds (VOCs) such as methanol over ethanol has crucial importance in the sensor studies since methanol poisoning may cause blindness, permanent neurologic dysfunction, and even death depending on the concentration.[239] There are various sensor designs in order to detect methanol, however relatively a small part of these studies are focused on selective detection of methanol in a solution.[240,241,242] Since sensing is a concept mainly based on surface adsorption, it is important to have high surface to volume ratio, therefore two-dimensional (2D) materials gained interest in sensor applications.[243]

There are several studies for detection ethanol and methanol with using graphene based sensors. For instance, RGO-SnO_2 nanocomposite exhibited an enhanced ethanol sensing performance (43 to 100ppm) in dry and humid atmosphere.[244] In addition to this, Phasuksom *et al.* reported that methanol sensing with graphene oxide/polyindole composites with high relative conductivity response (81.90$\pm$2.12) and sensitivity (7.37 ppm^{-1}).[245] However, the challenge is that when ethanol and methanol are mixed, it becomes almost impossible to distinguish between the two gases. There are very few studies in the literature to distinguish these two gases that are chemically similar in low concentrations.

The adsorption of gas molecules on graphene have been the focus of various experimental studies such as charge transfer doping,[246,57] chemical doping,[50] physisorption,[247] and quantum capacitance effect.[62] Wehling *et al.*[248] proved that density of states of graphene is suitable for chemical sensing and Schedin *et al.* explained with experimentally with single molecule NO_2 detection by graphene in high vacuum environment.[50] It is demonstrated that micro-meter sized sensor made from mechanically exfoliated graphene was capable of single molecule with changing charge carrier density of graphene. Electron acceptor (such as NO_2, H_2O) and electron donor gas molecules (CO, NH_3) effect on the graphene resistivity due to increase the hole concentrations by electron acceptors or vice versa. For instance, Yavari *et al.* manufactured a device which was distinctly superior to commercially available NO_2 and NH_3 sensors.[249] It is found CVD grown graphene films had an ultra-sensitive detection of NO_2 and NH_3 gases at room temperature. The detection limits of both gases reach the sub-ppm levels. In a different approach, change in conductivity or resistivity of the sensing material based on the charge transfer mechanism between graphene and adsorbed molecules. Yuan *et al.*[246] demonstrate that high sensitive simple chemoresistive type NO_2 gas sensor with the low limit of detection which mechanism based on charge transfer. In contrast to charge transfer mechanism, Pourasl *et al.* report that the adsorption effects of the CO, NO and NH_3 gases notably change on graphene band structure and quantum capacitance therefore it is indicated conductance decrement after gas adsorption.[61]

Theoretical investigation of molecule adsorption on 2D materials is important in order to understand the sensing mechanism of sensors. First-principles calculations is an important tool in determining the properties of the interactions between the analyte and the surface. Gas sensing abilities of various 2D materials are predicted in relative studies by the theoretical results.[250,251,21,252,253,254,255,256] Among these 2D materials, graphene and graphene derivatives are the most extensively studied materials with unique properties. Graphene derivatives such as graphene oxide, and transition metal functionalized graphene sheets are predicted to have reversible, operate in room temperature, and highly sensitive gas sensors.[257,258,259] On the other hand, pristine graphene is also an effective sensing material for molecules such as H_2O, NH_3, CO, NO_2, and NO.[57] interactions between the analyte and graphene is effected by the substrate. Caffrey *et al.* reported that SiC substrate increases the workfunction, which increases the results of charge transfer between graphene and NO_2 molecule, and increase the sensitivity.[260] In the experiments, graphene is expected to have defects and grain boundaries, therefore inspecting their effects are important in order to estimate the response. Increasing the defects on graphene surface vastly improves the sensitivity of NH_3 and NO_2 molecules.[261,262] Similar increase in sensitivity is also reported in the graphene grain boundaries.[263] Although the grain boundaries have distinct influence on the transport characteristics of graphene, electrons are able to propagate through, following the ballistic transport approximation.[264] Similar transport characteristics across the graphene sheets and adsorption of molecules with van der Waals interactions eliminates charge transfer based sensing mechanism. In contrast to the charge transfer approach between graphene and analyte, Pourasl *et al.* reported that quantum capacitance model better explains the gas sensing mechanism of graphene based gas sensors.[61]

Here, we investigate the sensing mechanism and selective sensing of methanol vapor in ethanol-methanol gas mixture in room temperature by using graphene-based gas sensor. Our devices are constructed of bilayer graphene, bridged between two gold electrodes. First-principles calculations are carried out to better understand the interactions between the analyte and graphene surface. Measurements are done under different bias voltages and methanol concentrations. Our results show that quantum capacitance of methanol and ethanol on graphene are quite different, therefore can be used to differentiate these molecules in ppm level.

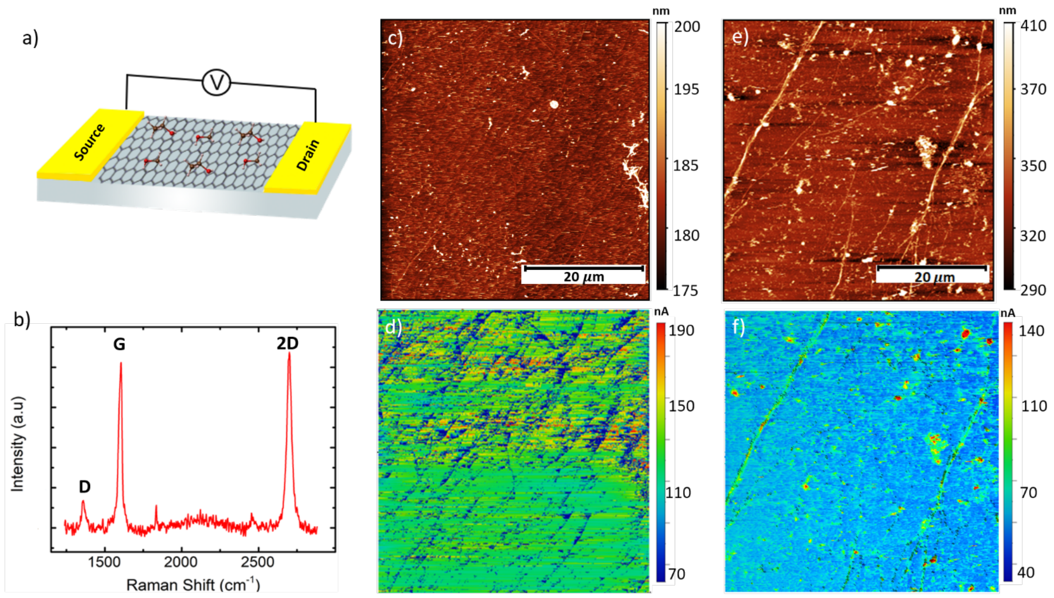

Figure 8.1. (a) Schematic representation of two terminal CVD-G sensor after adsorption ethanol and methanol molecules. (b) Raman spectrum with a 514 nm laser wavelength of bilayer graphene after transferred onto glass substrate (c) the enlarged 2D band regions of bilayer graphene with curves fitted by Lorentzian functions. (d) 50 $\times$ 50 sized AFM topography measurements of CVD-G sensor (scale bars represent 20) (e) Conductive AFM (c-AFM) current mapping with a Pt-coated tip of CVD-G sensor before adsorption of ethanol and methanol molecules

We designed a two-terminal sensor platform which CVD grown graphene lies in the middle of the substrate. The schematic representation of the sensor platform was depicted as in Figure 8.1(a). Raman spectroscopy measurements were carried out on the structural properties of transferred CVD graphene. The D, G (~1595 cm^{-1}) and 2D (~2700 cm^{-1}) bands are the predominant peaks in the spectrum of pristine graphene. Specifically, the G band corresponds to the doubly degenerate E_{2g} phonons at the Brillouin zone. The 2D and D bands are all induced by the second-order, double-resonance process and related to zone-boundary phonons. Besides, the full width at half maximum (FWM) of 2D peak and I_{2D}/I_G peak intensity ratio of CVD grown graphene is significantly different from single layer and few layer graphene. The FWHM of 2D peak is about 45 cm^{-1} and fitted with 4 components. Therefore, as shown in Figure 8.1(b), Raman spectrum of transferred CVD-graphene constitutes the spectroscopic signature of the bilayer graphene. To investigate the surface topography and local conductivity changes of CVD-G sensor measurements were carried out with AFM and c-AFM. The surface roughness of the CVD-G sensor was measured as 122,52 nm from topography measurement (Figure 8.1(c)). In c-AFM mapping measurements under 1V tip voltage taken from an area of 50 $\times$ 50 sized while the surface conductivity was measured as 135 nA, at wrinkled surface this value was determined as 80 nA which occurred during CVD graphene transferring process (Figure 8.1(d)). This analysis showed that the surface of CVD-G sensor surface was homogenous conductivity under bias.

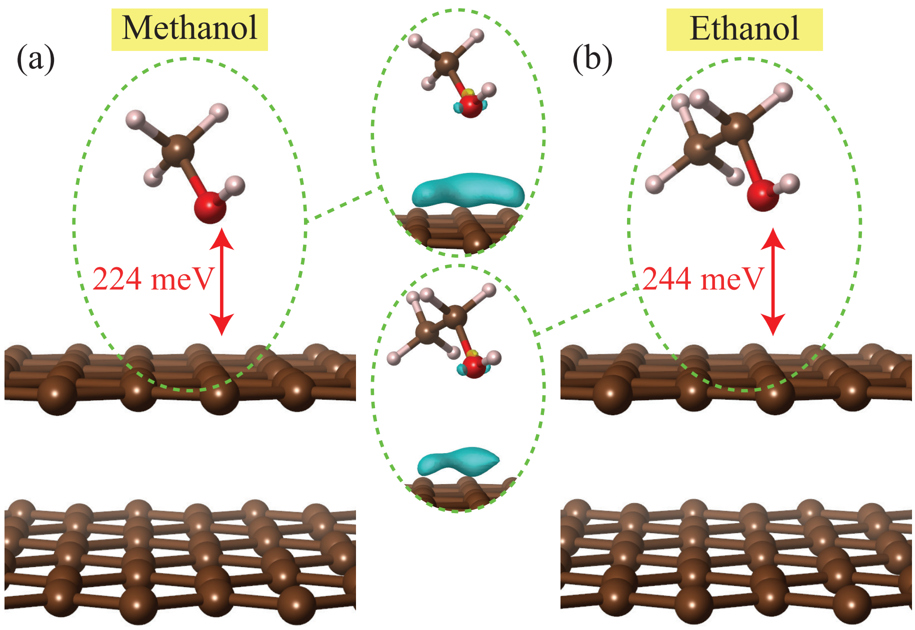

Figure 8.2. DFT results of the interaction between bilayer graphene and (a) methanol, (b) ethanol with the interaction energies. Charge density differences of methanol/graphene and ethanol/graphene systems are presented in the corresponding insets.

For investigation of the interactions between bilayer graphene and volatile organic compounds such as methanol and ethanol, we carry out state-of-the-art first principles calculations. Our results show that methanol and ethanol interact with the surface with binding energy of 224 and 244 meV as presented in Figure 8.2, respectively. In addition, charge transfer between graphene/methanol and graphene/ethanol systems are calculated by Bader technique. Charge transfer analysis shows that charge transfer from the molecules to the surface, or vice versa is negligibly small. Therefore, sensing mechanism of the systems cannot be simply explained by charge depletion between graphene and molecules. Therefore, further investigation of methanol and ethanol on graphene surface is carried out by calculating the charge density differences of the two systems. Results show that adsorption of molecules disrupts the local charge density at the adsorption sites, which results in hole puddles. It is reported previously that electron/hole puddles on graphene adjusts the transport properties of the system and at these density inhomogeneities on the graphene surface results with readings of finite conductivity even without applying gate voltage.[62,63] Therefore it is expected to electrically measure the adsorption of methanol and ethanol on graphene, and differentiating methanol from ethanol in gas mixture since the size of hole puddles are varying.

For sensing measurements we apply constant voltage of 1V to the two terminal sensor configuration and monitor the changes in their relative current upon exposure to different ethanol and methanol concentrations of gas species. Consistent with the density of states calculations, we observed that as the ethanol and methanol gas concentration increases 1 ppm to 30 ppm, the relative current change increases for both ethanol and methanol adsorption of CVD-G sensor (Figure 8.3). However, it was observed that this increase was 3 times higher when compared the concentration-dependent current change of ethanol compared to methanol, and this difference increased as the concentration increased. In addition, response and recovery times of methanol and ethanol are examined. It is found that 90% response times of methanol and ethanol are 109s and 112s while the 10% recovery times are 82s, and 93s, respectively.

Further investigation on the sensing properties of graphene-based methanol-ethanol sensors are carried out. Voltage dependent response of these gas sensors for methanol and ethanol are measured with DC 0.3, 0.8, 1.3, 1.8, and 2.3V potential difference between electrodes. Baseline extraction carried out in the postprocessing. In addition, since

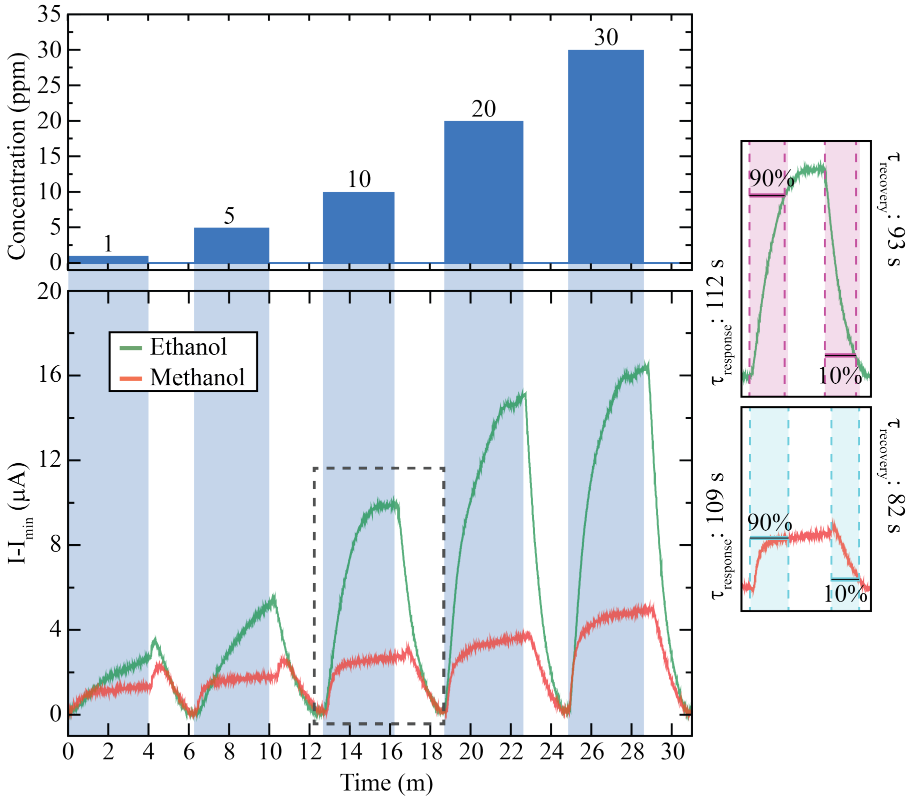

Figure 8.3. (a) Concentration dependent response to methanol and ethanol, displayed with red and green lines, respectively (b) response and recovery times of the methanol and ethanol measurements.

the interactions modify the capacitance of the system, results are employed in calculation of capacitance in methanol/graphene and ethanol/graphene systems. Results are displayed in Figure 8.4. It is demonstrated that capacitance of methanol/graphene and ethanol/graphene systems are different, therefore can be used to identify the concentration of the compound.

8.1. Conclusion

In this study, sensing capability of graphene-based sensors were investigated for detection of volatile organic compounds such as methanol and ethanol. Results showed that although the interactions between the molecules and graphene surface are weak, van der Waals type with negligibly small charge transfer, detection of these molecules are still possible. DFT results show that interaction of molecules with graphene surface results in local hole puddles. Capacitance of the system is effected by these interactions and

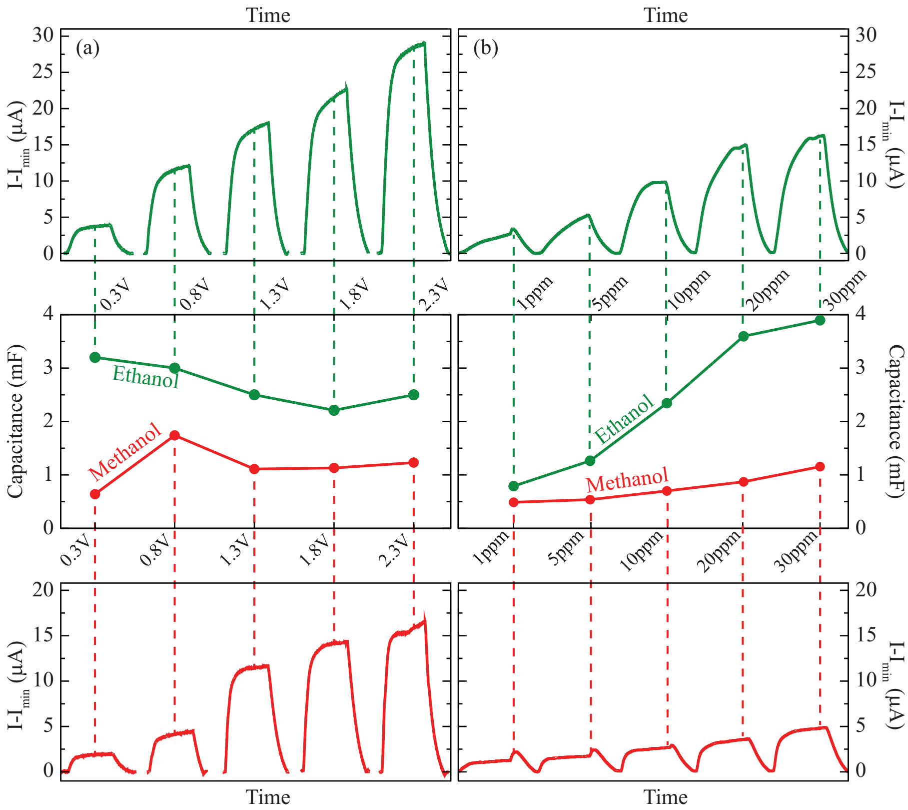

Figure 8.4. Voltage and concentration dependent capacitance of the methanol/graphene and ethanol/graphene systems with corresponding response readout.

change in the current occurs. In the methanol/graphene and ethanol/graphene systems, it is determined that current increases due to the increasing hole puddles. In addition, concentration dependent and voltage dependent measurements are carried out in order to examine the performance of the graphene-based sensors. Results show that these sensing devices are able to sense low concentrations such as 1ppm of VOCs. In both case, differences in the capacitance of methanol/graphene and ethanol/graphene systems are found to be different, which enables selective, repeatable sensing.

CHAPTER 9

CONCLUSION

2D materials offer great potential in various application areas due to their extraordinary physical properties. Therefore, it is important to determine these properties in order to precisely understand their mechanism. In the present thesis, materials are examined using both theoretical and experimental methods. In the theoretical part, density functional theory is used. In Chapter 3, structural, vibrational, mechanical, and electronic properties are determined. It is shown that 1T structures of calcium fluoride single-layers are dynamically stable. Analysis of the vibrational properties revealed that 1T-CaF_2 has Raman active modes, which would be useful in its detection. Electronic properties revealed that 1T-CaF_2 crystals have insulating property. Therefore, results are compared with widely used single-layer insulator h-BN. According to the results, CaF_2 is softer in comparison to h-BN, however with its wider band gap, it offers larger insulating property. Band alignments of CaF_2 and widely used single-layer crystals such as MoS_2, WS_2 and black phosphorene are found to form type-I heterojunction just as h-BN, however offering higher potential barrier. Investigation of nanoribbons of CaF_2 revealed that insulating property is not affected by ribbon-width, and rather remain as robust insulator. Therefore it is predicted that 1T-CaF_2 offers high potential in nanoscale device structures. Following 1T-CaF_2, other calcium halides structures are investigated in Chapter 4. In addition to 1T phase, examination of 1H phase which is another common phase is carried out. CaX_2 structures where X refers to F, Cl, Br, and I atoms are found dynamically stable. Electronic band structures calculated using HSE06 functional revealed that band gap in 1T phase is in range of 9.49–5.11 eV meanwhile in 1H phase it is between 8.73–4.38 eV. It is given that, in case of successful synthesis of these single-layers, Raman active modes with different frequencies can be used in characterization. Band alingments show that these crystals mainly form type-I and type-II heterojunctions. In conclusion, CaX_2 single-layers are predicted to be alternative candidates as insulating single-layers in nanoscale applications.

In Chapher 5, recently synthesized magnetic single-layers, and alteration of electronic properties via strain and V doping are investigated. Dynamical stability of FM and

AFM phases of VI_3 crystals are confirm via absence of imaginary phonon bands. Raman activities are calculated and results revealed that magnetic phases of VI_3 can be distinguished via their Raman spectra. Electronic band dispersions revealed that both FM and AFM phases are semiconductors. Moreover, in FM phase, wide difference in between major and minor spin band gaps shows that spin selective applications would result in different electronic response. Following the analysis in its pristine structure, V doped structures of ground state (FM) VI_3 single-layers are also investigated. V doping in different concentrations shows that these crystals vary in electronic structure, in different concentrations, half-metallic and semiconducting characteristics are expected to occur. In fully V doped structures, 1T-VI_2 forms, and the ground state switches to AFM phase. In addition to the V doping, applying strain alters the electronic and magnetic properties of VI_3 single-layers while retaining their dynamical stability. In closure, V dopant and strain dependent characteristics of VI_3 increases the capability of being used in spintronic applications.

Magnetism in 2D materials are employed in spintronics to achieve constructing devices with outstanding performance as it is stated in Chapher 5. Although there are high demands regarding magnetic monolayers, the number of these materials is considerably small. Therefore, studies regarding synthesis of novel magnetic monolayers are carried. In Chapter 6, synthesis of novel magnetic single-layers of manganese fluorides is proposed by recently reported method which involves fluorination of thinned down layered analogue. Occuring ion exchange results with fluorinated ultra-thin crystals. In this study, it is revealed that formation of manganese fluorides are energetically more favorable from manganese dichalcogenides. As result, there phases of manganese fluorides are predicted to occur; 1H-MnF_2, 1T-MnF_2, and MnF_3. Magnetic ground states of these crystals are found to be AFM for 1H-MnF_2 and FM for 1T-MnF_2 and MnF_3. Superexchange interactions are illustrated within these materials. It is revealed that these dynamically stable ultra-thin structures of manganese fluorides can be characterized via XRD, and Raman spectroscopy. Corresponding spectra are calculated and presented. Mechanical properties of these crystals are calculated. Due to its accordion-like structure, Poisson ratios (ν_x, ν_y)of MnF_3 are found to be negative. While these crystals are revealed to be semiconductors, band gap in MnF_3 is calculated extremely lower in comparison to MnF_2 phases. Band alignments of these ultra-thin crystals with known single-layers with low lattice mismatch values are presented. Results show that type-I,and type-II heterojuctions are predicted to occur between these magnetic MnF_2 crystals. However the predicted heterojunctions with type-III are displayed, due to unisotropic lattice therefore the relatively high lattice mismatch values, ultrathin MnF_3 are not feasible to form heterojunctions with these single-layers.

Defect formation in 2D materials is not a surprising phenomenon. It is known that defects alter the properties of materials, and it can be both beneficial or disadvantageous. Therefore it is important to understand the mechanism and affects of defects. In Chapter 7, collabration between experimental and theoretical approach is carried out. It is shown that there are three types of defect occuring in the STM images of ultrathin ReS_2 crystals. These defects are grouped as type A (bright spot in hallow), type B (bright spot), type C (hallow), and it is reported that majority of these defects are type A. In addition, by applying forward or reverse bias voltage, resulting STM images are adjusted. In order to understand the defect formation, S and Re defects; S and Re antisite defects, S and Re point defects are formed. In addition, oxygen adsorption and absorption are examined. Partial charge densities of these structures are calculated in range of [-2,0] eV, and [-2, 2] eV in order to simulate reverse bias and forward bias STM images. After the postprocessing of calculated partial charge densities, STM images are simulated. Results show that type B and type A defects are caused by S vacancies and oxygen absorption by S-vacancies, respectively. Although additional mechanism are proposed, those scenarios are found energetically less favorable. Following the theoretical results, XPS analysis revealed existence of O defects.

In Chapter 8, adsorption of volatile organic compounds such as methanol and ethanol on bilayer graphene surface is investigated. Results show that interaction energies in graphene/methanol and graphene/ethanol systems are van der Waals type. Charge density differences reveal formation of hole puddles while the charge transfer analysis reveals that charge transfer between methanol and ethanol molecules and graphene surface is negligibly small. However, when CVD grown graphene-based sensor is constructured, sensing device responds to methanol and ethanol gas. In addition, responses to these alcohols is show difference. Sensor response is examined in concentration dependent, and voltage dependent scenarios with more than one device. Capacitance of the response for methanol and ethanol is calculated seperately, and clear distinction is reported. Results show that graphene-based sensing device is capable of selective sensing of ethanol and methanol species.

In summary, graphene-like materials show great potential in optoelectronic applications. It is important to investigate their properties and mechanisms in different systems both theoretically and experimentally. Different groups of graphene-like materials can be employed in various applications. In order to predict the outcome, propose a working mechanism and/or improve the capabilities of graphene-like 2D materials in optoelectronic devices, it carries vital importance to carry out theoretical and experimental approach.

REFERENCES

[1] Kostya S Novoselov, Andre K Geim, Sergei V Morozov, D Jiang, Y_ Zhang, Sergey V Dubonos, Irina V Grigorieva, and Alexandr A Firsov. Electric field effect in atomically thin carbon films. *Science*, 306(5696):666–669, 2004.

[2] Andre K Geim and Konstantin S Novoselov. The rise of graphene. In *Nanoscience and Technology: A Collection of Reviews from Nature Journals*, pages 11–19. World Scientific, 2010.

[3] Changgu Lee, Xiaoding Wei, Jeffrey W Kysar, and James Hone. Measurement of the elastic properties and intrinsic strength of monolayer graphene. *Science*, 321(5887):385–388, 2008.

[4] Jian-Hao Chen, Chaun Jang, Shudong Xiao, Masa Ishigami, and Michael S Fuhrer. Intrinsic and extrinsic performance limits of graphene devices on SiO_2. *Nat. Nanotechnol.*, 3(4):206–209, 2008.

[5] Alexander S Mayorov, Roman V Gorbachev, Sergey V Morozov, Liam Britnell, Rashid Jalil, Leonid A Ponomarenko, Peter Blake, Kostya S Novoselov, Kenji Watanabe, Takashi Taniguchi, et al. Micrometer-scale ballistic transport in encapsulated graphene at room temperature. *Nano Lett.*, 11(6):2396–2399, 2011.

[6] Qiaoliang Bao and Kian Ping Loh. Graphene photonics, plasmonics, and broadband optoelectronic devices. *ACS Nano*, 6(5):3677–3694, 2012.

[7] TJ Echtermeyer, S Milana, U Sassi, A Eiden, M Wu, E Lidorikis, and AC Ferrari. Surface plasmon polariton graphene photodetectors. *Nano Lett.*, 16(1):8–20, 2016.

[8] Omer Salihoglu, Hasan Burkay Uzlu, Ozan Yakar, Shahnaz Aas, Osman Balci, Nurbek Kakenov, Sinan Balci, Selim Olcum, Sefik Suzer, and Coskun Kocabas. Graphene-based adaptive thermal camouflage. *Nano Lett.*, 18(7):4541–4548, 2018.

[9] M. Said Ergoktas, Gokhan Bakan, Pietro Steiner, Cian Bartlam, Yury Malevich, Elif Ozden-Yenigun, Guanliang He, Nazmul Karim, Pietro Cataldi, Mark A. Bissett, Ian A. Kinloch, Kostya S. Novoselov, and Coskun Kocabas. Graphene-enabled adaptive infrared textiles. *Nano Lett.*, 20(7):5346–5352, 2020. PMID: 32551694.

[10] Andres Castellanos-Gomez, Efrén Navarro-Moratalla, Guillermo Mokry, Jorge Quereda, Elena Pinilla-Cienfuegos, Nicolás Agraït, Herre SJ Van Der Zant, Eugenio Coronado, Gary A Steele, and Gabino Rubio-Bollinger. Fast and reliable identification of atomically thin layers of $TaSe_2$ crystals. *Nano Res.*, 6(3):191–199, 2013.

[11] Qing Hua Wang, Kourosh Kalantar-Zadeh, Andras Kis, Jonathan N Coleman, and Michael S Strano. Electronics and optoelectronics of two-dimensional transition metal dichalcogenides. *Nat. Nanotechnol.*, 7(11):699, 2012.

[12] Manish Chhowalla, Hyeon Suk Shin, Goki Eda, Lain-Jong Li, Kian Ping Loh, and Hua Zhang. The chemistry of two-dimensional layered transition metal dichalcogenide nanosheets. *Nat. Chem.*, 5(4):263, 2013.

[13] Chuanhong Jin, Fang Lin, Kazu Suenaga, and Sumio Iijima. Fabrication of a free-standing boron nitride single layer and its defect assignments. *Phys. Rev. Lett.*, 102:195505, May 2009.

[14] Mehmet Baskurt, Jun Kang, and Hasan Sahin. Octahedrally coordinated single layered CaF_2: robust insulating behaviour. *Phys. Chem. Chem. Phys.*, 22(5):2949–2954, 2020.

[15] Bevin Huang, Genevieve Clark, Efrén Navarro-Moratalla, Dahlia R Klein, Ran Cheng, Kyle L Seyler, Ding Zhong, Emma Schmidgall, Michael A McGuire, David H Cobden, et al. Layer-dependent ferromagnetism in a van der Waals crystal down to the monolayer limit. *Nature*, 546(7657):270–273, 2017.

[16] Wenyu Xing, Yangyang Chen, Patrick M Odenthal, Xiao Zhang, Wei Yuan, Tang Su, Qi Song, Tianyu Wang, Jiangnan Zhong, Shuang Jia, et al. Electric field effect

in multilayer $Cr_2Ge_2Te_6$: a ferromagnetic 2D material. *2D Mater.*, 4(2):024009, 2017.

[17] Fadil Iyikanat, M Yagmurcukardes, Ramazan Tugrul Senger, and H Sahin. Tuning electronic and magnetic properties of monolayer α-$RuCl_3$ by in-plane strain. *J. Mater. Chem. C*, 6(8):2019–2025, 2018.

[18] I Eren, F Iyikanat, and H Sahin. Defect tolerant and dimension dependent ferromagnetism in $MnSe_2$. *Phys. Chem. Chem. Phys.*, 21(30):16718–16725, 2019.

[19] Tai Kong, Karoline Stolze, Erik I Timmons, Jing Tao, Danrui Ni, Shu Guo, Zoë Yang, Ruslan Prozorov, and Robert J Cava. VI_3–a new layered ferromagnetic semiconductor. *Adv. Mater.*, 31(17):1808074, 2019.

[20] M Baskurt, I Eren, M Yagmurcukardes, and H Sahin. Vanadium dopant-and strain-dependent magnetic properties of single-layer VI_3. *Appl. Surf. Sci.*, 508:144937, 2020.

[21] Kin Fai Mak, Changgu Lee, James Hone, Jie Shan, and Tony F. Heinz. Atomically thin MoS_2: A new direct-gap semiconductor. *Phys. Rev. Lett.*, 105:136805, Sep 2010.

[22] Andrea Splendiani, Liang Sun, Yuanbo Zhang, Tianshu Li, Jonghwan Kim, Chi-Yung Chim, Giulia Galli, and Feng Wang. Emerging photoluminescence in monolayer MoS_2. *Nano Lett.*, 10(4):1271–1275, 2010.

[23] Ki Seok Kim, You Jin Ji, Ki Hyun Kim, Seunghyuk Choi, Dong-Ho Kang, Keun Heo, Seongjae Cho, Soonmin Yim, Sungjoo Lee, Jin-Hong Park, et al. Ultrasensitive MoS_2 photodetector by serial nano-bridge multi-heterojunction. *Nat. Commun.*, 10(1):1–10, 2019.

[24] Daria Krasnozhon, Dominik Lembke, Clemens Nyffeler, Yusuf Leblebici, and Andras Kis. Mos_2 transistors operating at gigahertz frequencies. *Nano Lett.*, 14(10):5905–5911, 2014.

[25] Yongmin He, Pengyi Tang, Zhili Hu, Qiyuan He, Chao Zhu, Luqing Wang, Qingsheng Zeng, Prafful Golani, Guanhui Gao, Wei Fu, et al. Engineering grain boundaries at the 2D limit for the hydrogen evolution reaction. *Nat. Commun.*, 11(1):1–12, 2020.

[26] Ling Zhang, Xuqiang Ji, Xiang Ren, Yongjun Ma, Xifeng Shi, Ziqi Tian, Abdullah M Asiri, Liang Chen, Bo Tang, and Xuping Sun. Electrochemical ammonia synthesis via nitrogen reduction reaction on a MoS_2 catalyst: theoretical and experimental studies. *Adv. Mater.*, 30(28):1800191, 2018.

[27] Deblina Sarkar, Wei Liu, Xuejun Xie, Aaron C Anselmo, Samir Mitragotri, and Kaustav Banerjee. MoS_2 field-effect transistor for next-generation label-free biosensors. *ACS Nano*, 8(4):3992–4003, 2014.

[28] Amir Barati Farimani, Kyoungmin Min, and Narayana R Aluru. DNA base detection using a single-layer MoS_2. *ACS Nano*, 8(8):7914–7922, 2014.

[29] F Keith Perkins, Adam L Friedman, Enrique Cobas, PM Campbell, GG Jernigan, and Berend T Jonker. Chemical vapor sensing with monolayer MoS_2. *Nano Lett.*, 13(2):668–673, 2013.

[30] Dattatray J Late, Yi-Kai Huang, Bin Liu, Jagaran Acharya, Sharmila N Shirodkar, Jiajun Luo, Aiming Yan, Daniel Charles, Umesh V Waghmare, Vinayak P Dravid, et al. Sensing behavior of atomically thin-layered MoS_2 transistors. *ACS Nano*, 7(6):4879–4891, 2013.

[31] Jing Xia, Xing Huang, Ling-Zhi Liu, Meng Wang, Lei Wang, Ben Huang, Dan-Dan Zhu, Jun-Jie Li, Chang-Zhi Gu, and Xiang-Min Meng. CVD synthesis of large-area, highly crystalline $MoSe_2$ atomic layers on diverse substrates and application to photodetectors. *Nanoscale*, 6(15):8949–8955, 2014.

[32] Alireza Khataee, Paria Eghbali, Mahsa Haddad Irani-Nezhad, and Aydin Hassani. Sonochemical synthesis of WS_2 nanosheets and its application in sonocatalytic removal of organic dyes from water solution. *Ultrason. Sonochem.*, 48:329–339,

2018.

[33] Chuanqi Feng, Lunfeng Huang, Zaiping Guo, and Huakun Liu. Synthesis of tungsten disulfide (WS_2) nanoflakes for lithium ion battery application. *Electrochem. Commun.*, 9(1):119–122, 2007.

[34] Jing-Kai Huang, Jiang Pu, Chang-Lung Hsu, Ming-Hui Chiu, Zhen-Yu Juang, Yung-Huang Chang, Wen-Hao Chang, Yoshihiro Iwasa, Taishi Takenobu, and Lain-Jong Li. Large-area synthesis of highly crystalline WSe_2 monolayers and device applications. *ACS Nano*, 8(1):923–930, 2014.

[35] Erfu Liu, Yajun Fu, Yaojia Wang, Yanqing Feng, Huimei Liu, Xiangang Wan, Wei Zhou, Baigeng Wang, Lubin Shao, Ching-Hwa Ho, et al. Integrated digital inverters based on two-dimensional anisotropic ReS_2 field-effect transistors. *Nat. Commun.*, 6(1):1–7, 2015.

[36] J Renteria, R Samnakay, C Jiang, TR Pope, P Goli, Z Yan, D Wickramaratne, TT Salguero, AG Khitun, RK Lake, et al. All-metallic electrically gated 2H-$TaSe_2$ thin-film switches and logic circuits. *J. Appl. Phys.*, 115(3):034305, 2014.

[37] Jiangtao Wu, Baolin Wang, Yujie Wei, Ronggui Yang, and Mildred Dresselhaus. Mechanics and mechanically tunable band gap in single-layer hexagonal boron-nitride. *Mater. Res. Lett.*, 1(4):200–206, 2013.

[38] D Usachov, VK Adamchuk, D Haberer, A Grüneis, H Sachdev, AB Preobrajenski, C Laubschat, and DV Vyalikh. Quasifreestanding single-layer hexagonal boron nitride as a substrate for graphene synthesis. *Phys. Rev. B*, 82(7):075415, 2010.

[39] Bevin Huang, Genevieve Clark, Dahlia R Klein, David MacNeill, Efrén Navarro-Moratalla, Kyle L Seyler, Nathan Wilson, Michael A McGuire, David H Cobden, Di Xiao, et al. Electrical control of 2D magnetism in bilayer CrI_3. *Nat. Nanotechnol.*, 13(7):544–548, 2018.

[40] Fawei Zheng, Jize Zhao, Zheng Liu, Menglei Li, Mei Zhou, Shengbai Zhang, and

Ping Zhang. Tunable spin states in the two-dimensional magnet CrI_3. *Nanoscale*, 10(29):14298–14303, 2018.

[41] Alessandro Molle, Carlo Grazianetti, Li Tao, Deepyanti Taneja, Md Hasibul Alam, and Deji Akinwande. Silicene, silicene derivatives, and their device applications. *Chem. Soc. Rev.*, 47(16):6370–6387, 2018.

[42] Jingjing Liu, Yang Yang, Pengbo Lyu, Petr Nachtigall, and Yuxi Xu. Few-layer silicene nanosheets with superior lithium-storage properties. *Adv. Mater.*, 30(26):1800838, 2018.

[43] Nana Liu, Guyue Bo, Yani Liu, Xun Xu, Yi Du, and Shi Xue Dou. Recent progress on germanene and functionalized Germanene: preparation, characterizations, applications, and challenges. *Small*, 15(32):1805147, 2019.

[44] Bobin Xu, Yingying Su, Li Li, Rui Liu, and Yi Lv. Thiol-functionalized single-layered MoS_2 nanosheet as a photoluminescence sensing platform via charge transfer for dopamine detection. *Sens. Actuators B Chem.*, 246:380–388, 2017.

[45] Yingjie Zhou, Aoning Wang, Zhoulu Wang, Miao Chen, Wei Wang, Luyi Sun, and Xiang Liu. Titanium functionalized α-zirconium phosphate single layer nanosheets for photocatalyst applications. *RSC Adv.*, 5(114):93969–93978, 2015.

[46] Qunhong Weng, Xuebin Wang, Xi Wang, Yoshio Bando, and Dmitri Golberg. Functionalized hexagonal boron nitride nanomaterials: emerging properties and applications. *Chem. Soc. Rev.*, 45(14):3989–4012, 2016.

[47] Jyoti Katoch, Søren Ulstrup, Roland J Koch, Simon Moser, Kathleen M McCreary, Simranjeet Singh, Jinsong Xu, Berend T Jonker, Roland K Kawakami, Aaron Bostwick, et al. Giant spin-splitting and gap renormalization driven by trions in single-layer WS_2/h-BN heterostructures. *Nat. Phys.*, 14(4):355–359, 2018.

[48] Hailong Chen, Xiewen Wen, Jing Zhang, Tianmin Wu, Yongji Gong, Xiang Zhang, Jiangtan Yuan, Chongyue Yi, Jun Lou, Pulickel M Ajayan, et al. Ultrafast forma-

tion of interlayer hot excitons in atomically thin MoS_2/WS_2 heterostructures. *Nat. Commun.*, 7(1):1–8, 2016.

[49] Arunabh Mukherjee, Kamran Shayan, Lizhong Li, Jie Shan, Kin Fai Mak, and A Nick Vamivakas. Observation of site-controlled localized charged excitons in CrI_3/WSe_2 heterostructures. *Nat. Commun.*, 11(1):1–8, 2020.

[50] Fredrik Schedin, Andrei Konstantinovich Geim, Sergei Vladimirovich Morozov, EW Hill, Peter Blake, MI Katsnelson, and Kostya Sergeevich Novoselov. Detection of individual gas molecules adsorbed on graphene. *Nat. Mater.*, 6(9):652–655, 2007.

[51] Ranjana Rautela, Samantha Scarfe, Jean-Michel Guay, Petr Lazar, Martin Pykal, Saied Azimi, Cedric Grenapin, Justin Boddison-Chouinard, Alexei Halpin, Weixiang Wang, et al. Mechanistic insight into the limiting factors of graphene-based environmental sensors. *ACS Appl. Mater. Interfaces*, 12(35):39764–39771, 2020.

[52] Mikhail Shekhirev, Alexey Lipatov, Angel Torres, Nataliia S Vorobeva, Ashley Harkleroad, Andrey Lashkov, Victor Sysoev, and Alexander Sinitskii. Highly selective gas sensors based on graphene nanoribbons grown by chemical vapor deposition. *ACS Appl. Mater. Interfaces*, 12(6):7392–7402, 2020.

[53] Priscilla Kailian Ang, Wei Chen, Andrew Thye Shen Wee, and Kian Ping Loh. Solution-gated epitaxial graphene as pH sensor. *J. Am. Chem. Soc.*, 130(44):14392–14393, 2008.

[54] Jun Yang, Dapeng Wei, Linlong Tang, Xuefen Song, Wei Luo, Jin Chu, Tianpeng Gao, Haofei Shi, and Chunlei Du. Wearable temperature sensor based on graphene nanowalls. *RSC Adv.*, 5(32):25609–25615, 2015.

[55] Sergey Rumyantsev, Guanxiong Liu, Michael S Shur, Radislav A Potyrailo, and Alexander A Balandin. Selective gas sensing with a single pristine graphene transistor. *Nano Lett.*, 12(5):2294–2298, 2012.

[56] Eric C Nallon, Vincent P Schnee, Collin Bright, Michael P Polcha, and Qiliang Li. Chemical discrimination with an unmodified graphene chemical sensor. *ACS Sens.*, 1(1):26–31, 2016.

[57] O Leenaerts, B Partoens, and FM Peeters. Adsorption of H_2O, NH_3, CO, NO_2, and NO on graphene: A first-principles study. *Phys. Rev. B*, 77(12):125416, 2008.

[58] Miao Zhou, Yun-Hao Lu, Yong-Qing Cai, Chun Zhang, and Yuan-Ping Feng. Adsorption of gas molecules on transition metal embedded graphene: a search for high-performance graphene-based catalysts and gas sensors. *Nanotechnology*, 22(38):385502, 2011.

[59] Charles W Bauschlicher Jr and Alessandra Ricca. Binding of NH_3 to graphite and to a (9, 0) carbon nanotube. *Phys. Rev. B*, 70(11):115409, 2004.

[60] TS Sreeprasad and Vikas Berry. How do the electrical properties of graphene change with its functionalization? *Small*, 9(3):341–350, 2013.

[61] Ali H Pourasl, Sharifah Hafizah Syed Ariffin, MT Ahmadi, Niayesh Gharaei, Rozeha A Rashid, and Razali Ismail. Quantum capacitance model for graphene FET-based gas sensor. *IEEE Sens. J.*, 19(10):3726–3732, 2019.

[62] Jilin Xia, Fang Chen, Jinghong Li, and Nongjian Tao. Measurement of the quantum capacitance of graphene. *Nature nanotechnology*, 4(8):505–509, 2009.

[63] Victor M Galitski, Shaffique Adam, and S Das Sarma. Statistics of random voltage fluctuations and the low-density residual conductivity of graphene. *Phys. Rev. B*, 76(24):245405, 2007.

[64] Max Born and Robert Oppenheimer. Zur quantentheorie der molekeln. *Ann. Phys.*, 389(20):457–484, 1927.

[65] Douglas R Hartree. The wave mechanics of an atom with a non-coulomb central field. part I. theory and methods. *Collection of articles for the multimedia elec-*

tronic educational-methodical complex on the discipline guillemotleft physics of the atom and atomic phenomena guillemotright / otv. ed. Shundalov MB; BSU, Faculty of Physics, 1928.

[66] Vladimir Fock. N "a method for solving the quantum mechanical multiple ö physical problem. *Zeitschrift fÃ¼r Physik*, 61(1-2):126–148, 1930.

[67] Llewellyn H Thomas. The calculation of atomic fields. In *Mathematical Proceedings of the Cambridge Philosophical Society*, volume 23, pages 542–548. Cambridge University Press, 1927.

[68] Enrico Fermi. Statistical method to determine some properties of atoms. *Rend. Accad. Naz. Lincei*, 6(602-607):5, 1927.

[69] Pierre Hohenberg and Walter Kohn. Inhomogeneous electron gas. *Phys. Rev.*, 136(3B):B864, 1964.

[70] David M Ceperley and Berni J Alder. Ground state of the electron gas by a stochastic method. *Phys. Rev. Lett.*, 45(7):566, 1980.

[71] John P Perdew, Kieron Burke, and Matthias Ernzerhof. Generalized gradient approximation made simple. *Phys. Rev. Lett.*, 77(18):3865, 1996.

[72] Jochen Heyd, Gustavo E Scuseria, and Matthias Ernzerhof. Hybrid functionals based on a screened Coulomb potential. *J. Chem. Phys.*, 118(18):8207–8215, 2003.

[73] Dario Alfe. PHON: A program to calculate phonons using the small displacement method. *Comput. Phys. Commun.*, 180(12):2622–2633, 2009.

[74] Atsushi Togo, Fumiyasu Oba, and Isao Tanaka. First-principles calculations of the ferroelastic transition between rutile-type and $CaCl_2$-type SiO_2 at high pressures. *Phys. Rev. B*, 78:134106, Oct 2008.

[75] Gerd Binnig, Heinrich Rohrer, Ch Gerber, and Eddie Weibel. Tunneling through a

controllable vacuum gap. *Appl. Phys. Lett.*, 40(2):178–180, 1982.

[76] Gerd Binnig, Heinrich Rohrer, Ch Gerber, and Edmund Weibel. Surface studies by scanning tunneling microscopy. *Phys. Rev. Lett.*, 49(1):57, 1982.

[77] Georg Kresse and Jürgen Hafner. Ab initio molecular dynamics for liquid metals. *Phys. Rev. B*, 47(1):558, 1993.

[78] Georg Kresse and Jürgen Furthmüller. Efficient iterative schemes for ab initio total-energy calculations using a plane-wave basis set. *Phys. Rev. B*, 54(16):11169, 1996.

[79] P. E. Blöchl. Projector augmented-wave method. *Phys. Rev. B*, 50:17953–17979, Dec 1994.

[80] Stefan Grimme. Semiempirical GGA-type density functional constructed with a long-range dispersion correction. *J. Comput. Chem.*, 27(15):1787–1799, 2006.

[81] Stefan Grimme, Stephan Ehrlich, and Lars Goerigk. Effect of the damping function in dispersion corrected density functional theory. *Journal of computational chemistry*, 32(7):1456–1465, 2011.

[82] Kyuho Lee, Éamonn D. Murray, Lingzhu Kong, Bengt I. Lundqvist, and David C. Langreth. Higher-accuracy van der Waals density functional. *Phys. Rev. B*, 82:081101, Aug 2010.

[83] Jiří Klimeš, David R Bowler, and Angelos Michaelides. Van der Waals density functionals applied to solids. *Phys. Rev. B*, 83(19):195131, 2011.

[84] Graeme Henkelman, Andri Arnaldsson, and Hannes Jónsson. A fast and robust algorithm for Bader decomposition of charge density. *Comput. Mater. Sci.*, 36(3):354–360, 2006.

[85] Limin Sun and Laurence C Chow. Preparation and properties of nano-sized calcium

fluoride for dental applications. *Dent. Mater.*, 24(1):111–116, 2008.

[86] Hockin HK Xu, Jennifer L Moreau, Limin Sun, and Laurence C Chow. Strength and fluoride release characteristics of a calcium fluoride based dental nanocomposite. *Biomaterials*, 29(32):4261–4267, 2008.

[87] Delia S Brauer, Natalia Karpukhina, Robert V Law, and Robert G Hill. Structure of fluoride-containing bioactive glasses. *J. Mater. Chem.*, 19(31):5629–5636, 2009.

[88] Ahmed Al-Noaman, Simon CF Rawlinson, and Robert G Hill. The influence of CaF_2 content on the physical properties and apatite formation of bioactive glass coatings for dental implants. *J. Non-Cryst. Solids*, 358(15):1850–1858, 2012.

[89] Huayan Yang, Shouning Yang, Jilie Kong, Aichun Dong, and Shaoning Yu. Obtaining information about protein secondary structures in aqueous solution using Fourier transform IR spectroscopy. *Nat. Protoc.*, 10(3):382, 2015.

[90] Ronen Adato and Hatice Altug. In-situ ultra-sensitive infrared absorption spectroscopy of biomolecule interactions in real time with plasmonic nanoantennas. *Nat. Commun.*, 4:2154, 2013.

[91] C Lecaplain, C Javerzac-Galy, ML Gorodetsky, and TJ Kippenberg. Mid-infrared ultra-high-Q resonators based on fluoride crystalline materials. *Nat. Commun.*, 7:13383, 2016.

[92] A Lucca, Mathieu Jacquemet, Frédéric Druon, François Balembois, Patrick Georges, Patrice Camy, Jean-Louis Doualan, and Richard Moncorgé. High-power tunable diode-pumped Yb^{3+}: CaF_2 laser. *Opt. Lett.*, 29(16):1879–1881, 2004.

[93] A Lucca, G Debourg, Mathieu Jacquemet, Frédéric Druon, François Balembois, Patrick Georges, Patrice Camy, Jean-Louis Doualan, and Richard Moncorgé. High-power diode-pumped Yb^{3+}: CaF_2 femtosecond laser. *Opt. Lett.*, 29(23):2767–2769, 2004.

[94] M Siebold, S Bock, U Schramm, B Xu, Jean-Louis Doualan, Patrice Camy, and Richard Moncorgé. Yb: CaF_2–a new old laser crystal. *Appl. Phys. B*, 97(2):327–338, 2009.

[95] P Aubry, A Bensalah, P Gredin, G Patriarche, D Vivien, and M Mortier. Synthesis and optical characterizations of Yb-doped CaF_2 ceramics. *Opt. Mater.*, 31(5):750–753, 2009.

[96] M Sh Akchurin, TT Basiev, AA Demidenko, ME Doroshenko, PP Fedorov, EA Garibin, PE Gusev, SV Kuznetsov, MA Krutov, IA Mironov, V. V. Osiko, and P. A. Popov. CaF_2: Yb laser ceramics. *Opt. Mater.*, 35(3):444–450, 2013.

[97] S E Hatch, W F Parsons, and R J Weagley. Hot-pressed polycrystalline CaF_2:Dy^{2+} laser. *Appl. Phys. Lett.*, 5(8):153–154, 1964.

[98] TP Smith III, Julia M Phillips, WM Augustyniak, and PJ Stiles. Fabrication of metal-epitaxial insulator-semiconductor field-effect transistors using molecular beam epitaxy of CaF_2 on Si. *Appl. Phys. Lett.*, 45(8):907–909, 1984.

[99] Kenji Watanabe, Takashi Taniguchi, and Hisao Kanda. Direct-bandgap properties and evidence for ultraviolet lasing of hexagonal boron nitride single crystal. *Nat. Mater.*, 3(6):404, 2004.

[100] Hyun Jeong, Seungho Bang, Hye Min Oh, Hyeon Jun Jeong, Sung-Jin An, Gang Hee Han, Hyun Kim, Ki Kang Kim, Jin Cheol Park, Young Hee Lee, Lerondel Gilles, and Mun Seok Jeong. Semiconductor–insulator–semiconductor diode consisting of monolayer MoS_2, h-BN, and GaN heterostructure. *Acs Nano*, 9(10):10032–10038, 2015.

[101] Mark P Levendorf, Cheol-Joo Kim, Lola Brown, Pinshane Y Huang, Robin W Havener, David A Muller, and Jiwoong Park. Graphene and boron nitride lateral heterostructures for atomically thin circuitry. *Nature*, 488(7413):627, 2012.

[102] Lu Hua Li and Ying Chen. Atomically thin boron nitride: unique properties and ap-

plications. *Adv. Funct. Mater.*, 26(16):2594–2608, 2016.

[103] Seongjoon Ahn, Gwangwoo Kim, Pramoda K Nayak, Seong In Yoon, Hyunseob Lim, Hyun-Joon Shin, and Hyeon Suk Shin. Prevention of transition metal dichalcogenide photodegradation by encapsulation with h-BN layers. *ACS nano*, 10(9):8973–8979, 2016.

[104] LJ Schowalter, RW Fathauer, RP Goehner, LG Turner, RW DeBlois, S Hashimoto, J-L Peng, WM Gibson, and JP Krusius. Epitaxial growth and characterization of CaF_2 on Si. *J. Appl. Phys*, 58(1):302–308, 1985.

[105] Yury Yu Illarionov, Alexander G Banshchikov, Dmitry K Polyushkin, Stefan Wachter, Theresia Knobloch, Mischa Thesberg, Lukas Mennel, Matthias Paur, Michael Stöger-Pollach, Andreas Steiger-Thirsfeld, Mikhail I. Vexler, Michael Waltl, Nikolai S. Sokolov, Thomas Mueller, and Tibor Grasser. Ultrathin calcium fluoride insulators for two-dimensional field-effect transistors. *Nat. Electron.*, 2:230–235, 2019.

[106] C Ataca, Mehmet Topsakal, E Akturk, and SJTJ Ciraci. A comparative study of lattice dynamics of three-and two-dimensional MoS_2. *J. Phys. Chem. C*, 115(33):16354–16361, 2011.

[107] Hasan Sahin, Seymur Cahangirov, Mehmet Topsakal, E Bekaroglu, E Akturk, Ramazan Tugrul Senger, and Salim Ciraci. Monolayer honeycomb structures of group-IV elements and III-V binary compounds: First-principles calculations. *Phys. Rev. B*, 80(15):155453, 2009.

[108] A Janotti, S-H Wei, and DJ Singh. First-principles study of the stability of BN and C. *Phys. Rev. B*, 64(17):174107, 2001.

[109] J. A. Carlisle, Eric L. Shirley, L. J. Terminello, J. J. Jia, T. A. Callcott, D. L. Ederer, R. C. C. Perera, and F. J. Himpsel. Band-structure and core-hole effects in resonant inelastic soft-x-ray scattering: Experiment and theory. *Phys. Rev. B*, 59:7433–7445, Mar 1999.

[110] M Yagmurcukardes, C Bacaksiz, E Unsal, B Akbali, RT Senger, and H Sahin. Strain mapping in single-layer two-dimensional crystals via Raman activity. *Phys. Rev. B*, 97(11):115427, 2018.

[111] David O Scanlon, Charles W Dunnill, John Buckeridge, Stephen A Shevlin, Andrew J Logsdail, Scott M Woodley, C Richard A Catlow, Michael J Powell, Robert G Palgrave, Ivan P Parkin, Graeme W. Watson, Thomas W. Keal, Paul Sherwood, Aron Walsh, and Alexey A. Sokol. Band alignment of rutile and anatase TiO_2. *Nat. Mater.*, 12(9):798, 2013.

[112] V Ongun Özcelik, Javad G Azadani, Ce Yang, Steven J Koester, and Tony Low. Band alignment of two-dimensional semiconductors for designing heterostructures with momentum space matching. *Phys. Rev. B*, 94(3):035125, 2016.

[113] M Yagmurcukardes, Engin Torun, Ramazan Tugrul Senger, Francois M Peeters, and H Sahin. $Mg(OH)_2$–WS_2 van der Waals heterobilayer: Electric field tunable band-gap crossover. *Phys. Rev. B*, 94(19):195403, 2016.

[114] Z Kahraman, A Kandemir, M Yagmurcukardes, and H Sahin. Single-layer janus-type platinum dichalcogenides and their heterostructures. *J. Phys. Chem. C*, 123(7):4549–4557, 2019.

[115] M Yagmurcukardes, S Ozen, F Iyikanat, FM Peeters, and H Sahin. Raman fingerprint of stacking order in HfS_2–$Ca(OH)_2$ heterobilayer. *Phys. Rev. B*, 99(20):205405, 2019.

[116] Thomas Ihn. *Semiconductor Nanostructures: Quantum States and Electronic Transport*. Oxford University Press, 2010.

[117] M Yagmurcukardes, François M Peeters, Ramazan Tuğrul Senger, and H Sahin. Nanoribbons: From fundamentals to state-of-the-art applications. *Appl. Phys. Rev.*, 3(4):041302, 2016.

[118] Francisco Güller, Ana Maria Llois, J Goniakowski, and Claudine Noguera. Prediction

of structural and metal-to-semiconductor phase transitions in nanoscale MoS_2, WS_2, and other transition metal dichalcogenide zigzag ribbons. *Phys. Rev. B*, 91(7):075407, 2015.

[119] James G Speight. *Environmental organic chemistry for engineers*. Butterworth-Heinemann, 2016.

[120] Lei Cheng, Michael D Weir, Hockin HK Xu, Alison M Kraigsley, Nancy J Lin, Sheng Lin-Gibson, and Xuedong Zhou. Antibacterial and physical properties of calcium-phosphate and calcium-fluoride nanocomposites with chlorhexidine. *Dent. Mater.*, 28(5):573–583, 2012.

[121] R.A. Robinson and R.H. Stokes. *Electrolyte Solutions: Second Revised Edition*. Dover Books on Chemistry Series. Dover Publications, Incorporated, 2012.

[122] Xiao M Wu, Yun S Yu, Chao Y Zhang, Geoff X Wang, and Bo Feng. Identifying the CO_2 capture performance of $CaCl_2$-supported amine adsorbent by the improved field synergy theory. *Ind. Eng. Chem. Res.*, 53(24):10225–10237, 2014.

[123] Xiao M Wu, De L Mu, Yun S Yu, and Zao X Zhang. String to characterize the field synergy during CO_2 capture by $CaCl_2$-supported MEA adsorbent. *J. Phys. Chem. C*, 119(1):473–485, 2014.

[124] Liping Kou, Tianbao Yang, Yaguang Luo, Xianjin Liu, Luhong Huang, and Eton Codling. Pre-harvest calcium application increases biomass and delays senescence of broccoli microgreens. *Postharvest Biol. Technol.*, 87:70–78, 2014.

[125] Jianghao Sun, Liping Kou, Ping Geng, Huilian Huang, Tianbao Yang, Yaguang Luo, and Pei Chen. Metabolomic assessment reveals an elevated level of glucosinolate content in $CaCl_2$ treated broccoli microgreens. *J. Agric. Food Chem.*, 63(6):1863–1868, 2015.

[126] Lijun Wang, Ling Ma, Huifen Xi, Wei Duan, Junfang Wang, and Shaohua Li. Individual and combined effects of $CaCl_2$ and UV–C on the biosynthesis of resveratrols

in grape leaves and berry skins. *J. Agric. Food Chem.*, 61(29):7135–7141, 2013.

[127] Chun Yi Liu and Ken-ichi Aika. Ammonia absorption into alkaline earth metal halide mixtures as an ammonia storage material. *Ind. Eng. Chem. Res.*, 43(23):7484–7491, 2004.

[128] Chun Yi Liu and Ken-ichi Aika. Effect of the cl/br molar ratio of a $CaCl_2$- $CaBr_2$ mixture used as an ammonia storage material. *Ind. Eng. Chem. Res.*, 43(22):6994–7000, 2004.

[129] Sameer Al-Asheh and Fawzi Banat. Isobaric vapor- liquid equilibrium of acetone+ methanol system in the presence of calcium bromide. *J. Chem. Eng. Data*, 50(6):1789–1793, 2005.

[130] Lalit Kumar, Tanu Mahajan, Vivek Sharma, and Dau Dayal Agarwal. Environmentally-benign and rapid bromination of industrially-important aromatics using an aqueous $CaBr_2$- Br_2 system as an instant and renewable brominating reagent. *Ind. Eng. Chem. Res.*, 50(2):705–712, 2010.

[131] Naohiko Kanai, Hiroki Nakayama, Norihiro Tada, and Akichika Itoh. Tandem oxidation/rearrangement of β-ketoesters to tartronic esters with molecular oxygen catalyzed by calcium iodide under visible light irradiation with fluorescent lamp. *Org. Lett.*, 12(9):1948–1951, 2010.

[132] Lars Longwitz, Johannes Steinbauer, Anke Spannenberg, and Thomas Werner. Calcium-based catalytic system for the synthesis of bio-derived cyclic carbonates under mild conditions. *ACS Catal.*, 8(1):665–672, 2017.

[133] Yuya Hu, Johannes Steinbauer, Vivian Stefanow, Anke Spannenberg, and Thomas Werner. Polyethers as complexing agents in calcium catalyzed cyclic carbonate synthesis. *ACS Sustain. Chem. Eng.*, 2019.

[134] Feng Lu, Weichao Wang, Xiaoguang Luo, Xinjian Xie, Yahui Cheng, Hong Dong, Hui Liu, and Wei-Hua Wang. A class of monolayer metal halogenides MX_2: Elec-

tronic structures and band alignments. *Applied Physics Letters*, 108(13):132104, 2016.

[135] Gargee Bhattacharyya, Priyanka Garg, Preeti Bhauriyal, and Biswarup Pathak. Density functional theory study of defect induced ferromagnetism and half-metallicity in CaI_2 based monolayer for spintronics applications. *ACS Appl. Nano Mater.*, 2(10):6152–6161, 2019.

[136] M Baskurt, M Yagmurcukardes, FM Peeters, and H Sahin. Stable single-layers of calcium halides (CaX_2, X= F, Cl, Br, I). *J. Chem. Phys.*, 152(16):164116, 2020.

[137] M Yagmurcukardes, RT Senger, FM Peeters, and H Sahin. Mechanical properties of monolayer GaS and GaSe crystals. *Phys. Rev. B*, 94(24):245407, 2016.

[138] Michael Golor, Stefan Wessel, and Manuel J Schmidt. Quantum nature of edge magnetism in graphene. *Phys. Rev. Lett.*, 112(4):046601, 2014.

[139] Tobias Wassmann, Ari P Seitsonen, A Marco Saitta, Michele Lazzeri, and Francesco Mauri. Structure, stability, edge states, and aromaticity of graphene ribbons. *Phys. Rev. Lett.*, 101(9):096402, 2008.

[140] Jia Zhang, Jia Mei Soon, Kian Ping Loh, Jianhua Yin, Jun Ding, Michael B Sullivian, and Ping Wu. Magnetic molybdenum disulfide nanosheet films. *Nano Lett.*, 7(8):2370–2376, 2007.

[141] AV Krasheninnikov, PO Lehtinen, Adam S Foster, Pekka Pyykkö, and Risto M Nieminen. Embedding transition-metal atoms in graphene: structure, bonding, and magnetism. *Phys. Rev. Lett.*, 102(12):126807, 2009.

[142] Oleg V Yazyev and Lothar Helm. Defect-induced magnetism in graphene. *Phys. Rev. B*, 75(12):125408, 2007.

[143] Miguel M Ugeda, Iván Brihuega, Francisco Guinea, and José M Gómez-Rodríguez. Missing atom as a source of carbon magnetism. *Phys. Rev. Lett.*, 104(9):096804,

2010.

[144] LJ De Jongh. Experiments on simple magnetic model systems. *J. Appl. Phys.*, 49(3):1305–1310, 1978.

[145] D Mauri, HC Siegmann, PS Bagus, and E Kay. Simple model for thin ferromagnetic films exchange coupled to an antiferromagnetic substrate. *J. Appl. Phys.*, 62(7):3047–3049, 1987.

[146] LJ De Jongh. Introduction to low-dimensional magnetic systems. In *Magnetic Properties of Layered Transition Metal Compounds*, pages 1–51. Springer, 1990.

[147] Nitin Samarth. Condensed-matter physics: Magnetism in flatland. *Nature*, 546(7657):216–218, 2017.

[148] M Gibertini, M Koperski, AF Morpurgo, and KS Novoselov. Magnetic 2D materials and heterostructures. *Nat. Nanotechnol.*, 14(5):408–419, 2019.

[149] Michael A McGuire, Hemant Dixit, Valentino R Cooper, and Brian C Sales. Coupling of crystal structure and magnetism in the layered, ferromagnetic insulator CrI_3. *Chem. Mater.*, 27(2):612–620, 2015.

[150] Cheng Gong and Xiang Zhang. Two-dimensional magnetic crystals and emergent heterostructure devices. *Science*, 363(6428), 2019.

[151] Shengwei Jiang, Jie Shan, and Kin Fai Mak. Electric-field switching of two-dimensional van der Waals magnets. *Nat. Mater.*, 17(5):406–410, 2018.

[152] Shengwei Jiang, Lizhong Li, Zefang Wang, Kin Fai Mak, and Jie Shan. Controlling magnetism in 2D CrI_3 by electrostatic doping. *Nat. Nanotechnol.*, 13(7):549–553, 2018.

[153] S Sarikurt, Y Kadioglu, F Ersan, E Vatansever, O Üzengi Aktürk, Y Yüksel, Ü Akıncı, and E Aktürk. Electronic and magnetic properties of monolayer α-$RuCl_3$: a first-

principles and Monte Carlo study. *Phys. Chem. Chem. Phys.*, 20(2):997–1004, 2018.

[154] Manuel Bonilla, Sadhu Kolekar, Yujing Ma, Horacio Coy Diaz, Vijaysankar Kalappattil, Raja Das, Tatiana Eggers, Humberto R Gutierrez, Manh-Huong Phan, and Matthias Batzill. Strong room-temperature ferromagnetism in VSe_2 monolayers on van der Waals substrates. *Nat. Nanotechnol.*, 13(4):289–293, 2018.

[155] Paula Mariel Coelho, Kien Nguyen Cong, Manuel Bonilla, Sadhu Kolekar, Manh-Huong Phan, Jose Avila, Maria C Asensio, Ivan I Oleynik, and Matthias Batzill. Charge density wave state suppresses ferromagnetic ordering in VSe_2 monolayers. *J. Phys. Chem. C*, 123(22):14089–14096, 2019.

[156] Engin Torun, H Sahin, SK Singh, and FM Peeters. Stable half-metallic monolayers of $FeCl_2$. *Appl. Phys. Lett.*, 106(19):192404, 2015.

[157] Junjie He, Shuangying Ma, Pengbo Lyu, and Petr Nachtigall. Unusual Dirac half-metallicity with intrinsic ferromagnetism in vanadium trihalide monolayers. *J. Mater. Chem. C*, 4(13):2518–2526, 2016.

[158] KO Berry, RR Smardzewski, and RE McCarley. Vaporization reactions of vanadium iodides and evidence for gaseous vanadium (IV) iodide. *Inorg. Chem.*, 8(9):1994–1997, 1969.

[159] Dirk Juza, Dieter Giegling, and Harald Schäfer. Über die vanadinjodide VJ_2 und VJ_3. *Z. Anorg. Allg. Chem.*, 366(3-4):121–129, 1969.

[160] Shangjie Tian, Jian-Feng Zhang, Chenghe Li, Tianping Ying, Shiyan Li, Xiao Zhang, Kai Liu, and Hechang Lei. Ferromagnetic van der Waals crystal VI_3. *J. Am. Chem. Soc.*, 141(13):5326–5333, 2019.

[161] Suhan Son, Matthew J Coak, Nahyun Lee, Jonghyeon Kim, Tae Yun Kim, Hayrullo Hamidov, Hwanbeom Cho, Cheng Liu, David M Jarvis, Philip AC Brown, et al. Bulk properties of the van der Waals hard ferromagnet VI_3. *Phys. Rev. B*,

99(4):041402, 2019.

[162] Fadil Iyikanat, H Sahin, Ramazan Tugrul Senger, and Francois M Peeters. Vacancy formation and oxidation characteristics of single layer TiS_3. *J. Phys. Chem. C*, 119(19):10709–10715, 2015.

[163] E Torun, H Sahin, S Cahangirov, Angel Rubio, and FM Peeters. Anisotropic electronic, mechanical, and optical properties of monolayer WTe_2. *J. Appl. Phys.*, 119(7):074307, 2016.

[164] Santu Baidya, Jaejun Yu, and Choong H Kim. Tunable magnetic topological insulating phases in monolayer CrI_3. *Phys. Rev. B*, 98(15):155148, 2018.

[165] Lingling Ren, Qian Liu, Pengxiang Xu, Zhicheng Zhong, Li Yang, Zhe Yuan, and Ke Xia. Noncollinearity-modulated electronic properties of monolayer CrI_3. *Phys. Rev. Appl.*, 11(5):054042, 2019.

[166] Lucas Webster and Jia-An Yan. Strain-tunable magnetic anisotropy in monolayer $CrCl_3$, $CrBr_3$, and CrI_3. *Phys. Rev. B*, 98(14):144411, 2018.

[167] Yandong Ma, Ying Dai, Meng Guo, Chengwang Niu, Yingtao Zhu, and Baibiao Huang. Evidence of the existence of magnetism in pristine VX_2 monolayers (X= S, Se) and their strain-induced tunable magnetic properties. *ACS Nano*, 6(2):1695–1701, 2012.

[168] Hang Wu, Weifeng Zhao, and Guohua Chen. One-pot in situ ball milling preparation of polymer/graphene nanocomposites. *J. Appl. Polym. Sci.*, 125(5):3899–3903, 2012.

[169] Alexandre Abhervé, Samuel Manas-Valero, Miguel Clemente-León, and Eugenio Coronado. Graphene related magnetic materials: micromechanical exfoliation of 2d layered magnets based on bimetallic anilate complexes with inserted $[Fe^{III}$ $(acac_2\text{-trien})]^+$ and $[Fe^{III}$ $(sal_2\text{-trien})]^+$ molecules. *Chem. Sci.*, 6(8):4665–4673, 2015.

[170] Robert C Sinclair, James L Suter, and Peter V Coveney. Micromechanical exfoliation of graphene on the atomistic scale. *Phys. Chem. Chem. Phys.*, 21(10):5716–5722, 2019.

[171] Xuesong Li, Weiwei Cai, Jinho An, Seyoung Kim, Junghyo Nah, Dongxing Yang, Richard Piner, Aruna Velamakanni, Inhwa Jung, Emanuel Tutuc, et al. Large-area synthesis of high-quality and uniform graphene films on copper foils. *Science*, 324(5932):1312–1314, 2009.

[172] Sukang Bae, Hyeongkeun Kim, Youngbin Lee, Xiangfan Xu, Jae-Sung Park, Yi Zheng, Jayakumar Balakrishnan, Tian Lei, Hye Ri Kim, Young Il Song, et al. Roll-to-roll production of 30-inch graphene films for transparent electrodes. *Nat. Nanotechnol.*, 5(8):574, 2010.

[173] Yongjie Zhan, Zheng Liu, Sina Najmaei, Pulickel M Ajayan, and Jun Lou. Large-area vapor-phase growth and characterization of MoS_2 atomic layers on a SiO_2 substrate. *Small*, 8(7):966–971, 2012.

[174] Feng-feng Zhu, Wei-jiong Chen, Yong Xu, Chun-lei Gao, Dan-dan Guan, Can-hua Liu, Dong Qian, Shou-Cheng Zhang, and Jin-feng Jia. Epitaxial growth of two-dimensional stanene. *Nat. Mater.*, 14(10):1020, 2015.

[175] ME Dávila, Lede Xian, Seymur Cahangirov, Angel Rubio, and Guy Le Lay. Germanene: a novel two-dimensional germanium allotrope akin to graphene and silicene. *New J. Phys.*, 16(9):095002, 2014.

[176] Jinfeng Chen, Miao Duan, and Guohua Chen. Continuous mechanical exfoliation of graphene sheets via three-roll mill. *J. Mater. Chem.*, 22(37):19625–19628, 2012.

[177] Vishnu Sreepal, Mehmet Yagmurcukardes, Kalangi S Vasu, Daniel J Kelly, Sarah FR Taylor, Vasyl G Kravets, Zakhar Kudrynskyi, Zakhar D Kovalyuk, Amalia Patanè, Alexander N Grigorenko, Sarah J. Haigh, Christopher Hardacre, Laurence Eaves, Hasan Sahin, Andre K. Geim, Francois M. Peeters, and Rahul R. Nair. Two-dimensional covalent crystals by chemical conversion of thin van der Waals ma-

terials. *Nano Lett.*, 19(9):6475–6481, 2019.

[178] Z Mazej. Room temperature syntheses of MnF_3, MnF_4 and hexafluoromanganete (IV) salts of alkali cations. *J. Fluor. Chem.*, 114(1):75–80, 2002.

[179] R Fowler, H Anderson, J Hamilton, Jr, W Burford III, A Spadetti, S Bitterlich, and I Litant. Metallic fluorides in fluorocarbon synthesis-manganese trifuoride, cericfluoride, etc., as alternates for cobalt trifuoride. *Ind. Eng. Chem. Res.*, 39(3):343–345, 1947.

[180] Yalong Jiao, Fengxian Ma, Chunmei Zhang, John Bell, Stefano Sanvito, and Aijun Du. First-principles prediction of spin-polarized multiple Dirac rings in manganese fluoride. *Phys. Rev. Lett.*, 119(1):016403, 2017.

[181] Padmabati Mondal and Wolfgang Domcke. Infrared absorption spectra of Jahn–Teller systems: application to the transition-metal trifluorides MnF_3 and NiF_3. *J. Phys. Chem. A*, 118(21):3726–3734, 2014.

[182] Marcel Poulain. Halide glasses. *J. Non-Cryst. Solids*, 56(1-3):1–14, 1983.

[183] Jacques Lucas. Fluoride glasses. *J. Mater. Sci.*, 24(1):1–13, 1989.

[184] Kun Rui, Zhaoyin Wen, Yan Lu, Jun Jin, and Chen Shen. One-step solvothermal synthesis of nanostructured manganese fluoride as an anode for rechargeable lithium-ion batteries and insights into the conversion mechanism. *Adv. Energy Mater.*, 5(7):1401716, 2015.

[185] Antonin Grenier, Ana-Gabriela Porras-Gutierrez, Antoine Desrues, Sandrine Leclerc, Olaf J Borkiewicz, Henri Groult, and Damien Dambournet. Synthesis and optimized formulation for high-capacity manganese fluoride (MnF_2) electrodes for lithium-ion batteries. *J. Fluor. Chem.*, 224:45–51, 2019.

[186] Taiju Tsuboi, P Silfsten, and R Laiho. Fast luminescence observed in MnF_2 crystals. *Phys. Rev. B*, 43(1):1135, 1991.

[187] I Hernández, Fernando Rodríguez, and HD Hochheimer. Pressure-induced two-color photoluminescence in MnF_2 at room temperature. *Phys. Rev. Lett.*, 99(2):027403, 2007.

[188] Can Ataca, Hasan Sahin, and Salim Ciraci. Stable, single-layer MX_2 transition-metal oxides and dichalcogenides in a honeycomb-like structure. *J. Phys. Chem. C*, 116(16):8983–8999, 2012.

[189] Wei Chen, Jian-Min Zhang, Yao-Zhuang Nie, Qing-Lin Xia, and Guang-Hua Guo. Tuning magnetic properties of single-layer $MnTe_2$ via strain engineering. *J. Phys. Chem. Solids*, 143:109489, 2020.

[190] Mohammad Rahman, Kenneth Davey, and Shi-Zhang Qiao. Advent of 2D rhenium disulfide (ReS_2): fundamentals to applications. *Adv. Func. Mater.*, 27(10):1606129, 2017.

[191] H-J Lamfers, A Meetsma, GA Wiegers, and JL De Boer. The crystal structure of some rhenium and technetium dichalcogenides. *J. Alloys Compd.*, 241(1-2):34–39, 1996.

[192] HH Murray, SP Kelty, RR Chianelli, and CS Day. Structure of rhenium disulfide. *Inorg. Chem.*, 33(19):4418–4420, 1994.

[193] Dmitry Ovchinnikov, Fernando Gargiulo, Adrien Allain, Diego José Pasquier, Dumitru Dumcenco, Ching-Hwa Ho, Oleg V Yazyev, and Andras Kis. Disorder engineering and conductivity dome in ReS_2 with electrolyte gating. *Nat. Commun.*, 7(1):1–7, 2016.

[194] Daniel A Chenet, O Burak Aslan, Pinshane Y Huang, Chris Fan, Arend M van der Zande, Tony F Heinz, and James C Hone. In-plane anisotropy in mono-and few-layer ReS_2 probed by Raman spectroscopy and scanning transmission electron microscopy. *Nano Lett.*, 15(9):5667–5672, 2015.

[195] Ozgur Burak Aslan, Daniel A Chenet, Arend M Van Der Zande, James C Hone, and

Tony F Heinz. Linearly polarized excitons in single-and few-layer ReS_2 crystals. *ACS Photonics*, 3(1):96–101, 2016.

[196] CH Ho, YS Huang, Kwong-Kau Tiong, and PC Liao. Absorption-edge anisotropy in ReS_2 and $ReSe_2$ layered semiconductors. *Phys. Rev. B*, 58(24):16130, 1998.

[197] Sangwan Sim, Doeon Lee, Artur V Trifonov, Taeyoung Kim, Soonyoung Cha, Ji Ho Sung, Sungjun Cho, Wooyoung Shim, Moon-Ho Jo, and Hyunyong Choi. Ultrafast quantum beats of anisotropic excitons in atomically thin ReS_2. *Nat. Commun.*, 9(1):1–7, 2018.

[198] Sheng Yu, Hao Zhu, Kwesi Eshun, Chen Shi, Min Zeng, and Qiliang Li. Strain-engineering the anisotropic electrical conductance in ReS_2 monolayer. *Appl. Phys. Lett.*, 108(19):191901, 2016.

[199] Bhakti Jariwala, Damien Voiry, Apoorv Jindal, Bhagyashree A Chalke, Rudheer Bapat, Arumugam Thamizhavel, Manish Chhowalla, Mandar Deshmukh, and Arnab Bhattacharya. Synthesis and characterization of ReS_2 and $ReSe_2$ layered chalcogenide single crystals. *Chem. Mater.*, 28(10):3352–3359, 2016.

[200] Yung-Chang Lin, Hannu-Pekka Komsa, Chao-Hui Yeh, Torbjorn Bjorkman, Zheng-Yong Liang, Ching-Hwa Ho, Ying-Sheng Huang, Po-Wen Chiu, Arkady V Krasheninnikov, and Kazu Suenaga. Single-layer ReS_2: two-dimensional semiconductor with tunable in-plane anisotropy. *ACS Nano*, 9(11):11249–11257, 2015.

[201] Stephen P Kelty, Albert F Ruppert, Russell R Chianelli, JINGQING Ren, and M-H Whangbo. Scanning probe microscopy study of layered dichalcogenide ReS_2. *J. Am. Chem. Soc.*, 116(17):7857–7863, 1994.

[202] K Friemelt, S Akari, M-Ch Lux-Steiner, T Schill, E Bucher, and K Dransfeld. Scanning tunneling microscopy with atomic resolution on ReS_2 single crystals grown by vapor phase transport. *Ann. Phys.*, 504(4):248–253, 1992.

[203] Seong Jun Jung, Taehwan Jeong, Jaewoo Shim, Sangwoo Park, Jin-hong Park, Bong Gyu Shin, and Young Jae Song. Atomic-registry-dependent electronic structures of sulfur vacancies in ReS_2 studied by scanning tunneling microscopy/spectroscopy. *Curr. Appl. Phys.*, 19(3):224–229, 2019.

[204] Fucai Liu, Shoujun Zheng, Xuexia He, Apoorva Chaturvedi, Junfeng He, Wai Leong Chow, Thomas R Mion, Xingli Wang, Jiadong Zhou, Qundong Fu, et al. Highly sensitive detection of polarized light using anisotropic 2D ReS_2. *Adv. Func. Mater.*, 26(8):1169–1177, 2016.

[205] Sajedeh Manzeli, Dmitry Ovchinnikov, Diego Pasquier, Oleg V Yazyev, and Andras Kis. 2D transition metal dichalcogenides. *Nat. Rev. Mater.*, 2(8):17033, 2017.

[206] Zhong Lin, Bruno R Carvalho, Ethan Kahn, Ruitao Lv, Rahul Rao, Humberto Terrones, Marcos A Pimenta, and Mauricio Terrones. Defect engineering of two-dimensional transition metal dichalcogenides. *2D Mater.*, 3(2):022002, 2016.

[207] Adina Luican-Mayer, Jose E Barrios-Vargas, Jesper Toft Falkenberg, Gabriel Autès, Aron W Cummings, David Soriano, Guohong Li, Mads Brandbyge, Oleg V Yazyev, Stephan Roche, et al. Localized electronic states at grain boundaries on the surface of graphene and graphite. *2D Mater.*, 3(3):031005, 2016.

[208] Adina Luican-Mayer, Guohong Li, and Eva Y Andrei. Atomic scale characterization of mismatched graphene layers. *J. Electron Spectros. and Relat. Phenomena*, 219:92–98, 2017.

[209] Hao Qiu, Tao Xu, Zilu Wang, Wei Ren, Haiyan Nan, Zhenhua Ni, Qian Chen, Shijun Yuan, Feng Miao, Fengqi Song, et al. Hopping transport through defect-induced localized states in molybdenum disulphide. *Nat. Commun.*, 4(1):1–6, 2013.

[210] Jaewoo Shim, Seyong Oh, Dong-Ho Kang, Seo-Hyeon Jo, Muhammad Hasnain Ali, Woo-Young Choi, Keun Heo, Jaeho Jeon, Sungjoo Lee, Minwoo Kim, et al. Phosphorene/rhenium disulfide heterojunction-based negative differential resistance device for multi-valued logic. *Nat. Commun.*, 7(1):1–8, 2016.

[211] Sefaattin Tongay, Joonki Suh, Can Ataca, Wen Fan, Alexander Luce, Jeong Seuk Kang, Jonathan Liu, Changhyun Ko, Rajamani Raghunathanan, Jian Zhou, et al. Defects activated photoluminescence in two-dimensional semiconductors: interplay between bound, charged and free excitons. *Sci. Rep.*, 3(1):1–5, 2013.

[212] Mete Atatüre, Dirk Englund, Nick Vamivakas, Sang-Yun Lee, and Joerg Wrachtrup. Material platforms for spin-based photonic quantum technologies. *Nat. Rev. Mater.*, 3(5):38–51, 2018.

[213] Gabriele Grosso, Hyowon Moon, Benjamin Lienhard, Sajid Ali, Dmitri K Efetov, Marco M Furchi, Pablo Jarillo-Herrero, Michael J Ford, Igor Aharonovich, and Dirk Englund. Tunable and high-purity room temperature single-photon emission from atomic defects in hexagonal boron nitride. *Nat. Commun.*, 8(1):1–8, 2017.

[214] Sara Barja, Sivan Refaely-Abramson, Bruno Schuler, Diana Y Qiu, Artem Pulkin, Sebastian Wickenburg, Hyejin Ryu, Miguel M Ugeda, Christoph Kastl, Christopher Chen, et al. Identifying substitutional oxygen as a prolific point defect in monolayer transition metal dichalcogenides. *Nat. Commun.*, 10(1):1–8, 2019.

[215] Bruno Schuler, Diana Y Qiu, Sivan Refaely-Abramson, Christoph Kastl, Christopher T Chen, Sara Barja, Roland J Koch, D Frank Ogletree, Shaul Aloni, Adam M Schwartzberg, et al. Large spin-orbit splitting of deep in-gap defect states of engineered sulfur vacancies in monolayer WS_2. *Phys. Rev. Lett.*, 123(7):076801, 2019.

[216] Ryan Plumadore, Mehmet Baskurt, Justin Boddison-Chouinard, Gregory Lopinski, Mohsen Modarresi, Pawel Potasz, Pawel Hawrylak, Hasan Sahin, Francois M Peeters, and Adina Luican-Mayer. Prevalence of oxygen defects in an in-plane anisotropic transition metal dichalcogenide. *Phys. Rev. B*, 102(20):205408, 2020.

[217] James L Webb, Lewis S Hart, Daniel Wolverson, Chaoyu Chen, Jose Avila, and Maria C Asensio. Electronic band structure of ReS_2 by high-resolution angle-resolved photoemission spectroscopy. *Phys. Rev. B*, 96(11):115205, 2017.

[218] Hong-Xia Zhong, Shiyuan Gao, Jun-Jie Shi, and Li Yang. Quasiparticle band gaps, excitonic effects, and anisotropic optical properties of the monolayer distorted 1t diamond-chain structures ReS_2 and $ReSe_2$. *Phys. Rev. B*, 92(11):115438, 2015.

[219] Ignacio Gutiérrez-Lezama, Bojja Aditya Reddy, Nicolas Ubrig, and Alberto F Morpurgo. Electroluminescence from indirect band gap semiconductor ReS_2. *2D Mater.*, 3(4):045016, 2016.

[220] Mathias Gehlmann, Irene Aguilera, Gustav Bihlmayer, Slavomir Nemsak, Philipp Nagler, Pika Gospodaric, Giovanni Zamborlini, Markus Eschbach, Vitaliy Feyer, Florian Kronast, et al. Direct observation of the band gap transition in atomically thin ReS_2. *Nano Lett.*, 17(9):5187–5192, 2017.

[221] K Dileep, R Sahu, Sumanta Sarkar, Sebastian C Peter, and Ranjan Datta. Layer specific optical band gap measurement at nanoscale in MoS_2 and ReS_2 van der Waals compounds by high resolution electron energy loss spectroscopy. *J. Appl. Phys.*, 119(11):114309, 2016.

[222] CH Ho, PC Liao, YS Huang, Tzuen-Rong Yang, and KK Tiong. Optical absorption of ReS_2 and $ReSe_2$ single crystals. *J. Appl. Phys.*, 81(9):6380–6383, 1997.

[223] Deniz Cakir, Hasan Sahin, and Francois M Peeters. Doping of rhenium disulfide monolayers: a systematic first principles study. *Phys. Chem. Chem. Phys.*, 16(31):16771–16779, 2014.

[224] Zhi Gen Yu, Yongqing Cai, and Yong-Wei Zhang. Robust direct bandgap characteristics of one-and two-dimensional ReS_2. *Sci. Rep.*, 5:13783, 2015.

[225] Xi Ling, Han Wang, Shengxi Huang, Fengnian Xia, and Mildred S Dresselhaus. The renaissance of black phosphorus. *Proc. Natl. Acad. Sci.*, 112(15):4523–4530, 2015.

[226] James V Marzik, Robert Kershaw, Kirby Dwight, and Aaron Wold. Photoelectronic properties of ReS_2 and $ReSe_2$ single crystals. *J. Solid State Chem.*, 51(2):170–175,

1984.

[227] Jl A Wilson and AD Yoffe. The transition metal dichalcogenides discussion and interpretation of the observed optical, electrical and structural properties. *Adv. Phys.*, 18(73):193–335, 1969.

[228] Jun Dai and Xiao Cheng Zeng. Titanium trisulfide monolayer: theoretical prediction of a new direct-gap semiconductor with high and anisotropic carrier mobility. *Angew. Chem.*, 127(26):7682–7686, 2015.

[229] Miguel M Ugeda, Aaron J Bradley, Su-Fei Shi, H Felipe, Yi Zhang, Diana Y Qiu, Wei Ruan, Sung-Kwan Mo, Zahid Hussain, Zhi-Xun Shen, et al. Giant bandgap renormalization and excitonic effects in a monolayer transition metal dichalcogenide semiconductor. *Nat. Mater.*, 13(12):1091–1095, 2014.

[230] R áM Feenstra. Tunneling spectroscopy of the (110) surface of direct-gap III-V semiconductors. *Phys. Rev. B*, 50(7):4561, 1994.

[231] Chih-Pin Lu, Guohong Li, Jinhai Mao, Li-Min Wang, and Eva Y Andrei. Bandgap, mid-gap states, and gating effects in MoS_2. *Nano Lett.*, 14(8):4628–4633, 2014.

[232] Ryan Plumadore, Mohammed M Al Ezzi, Shaffique Adam, and Adina Luican-Mayer. Moiré patterns in graphene–rhenium disulfide vertical heterostructures. *J. Appl. Phys.*, 128(4):044303, 2020.

[233] Brian Kiraly, Nadine Hauptmann, Alexander N Rudenko, Mikhail I Katsnelson, and Alexander A Khajetoorians. Probing single vacancies in black phosphorus at the atomic level. *Nano Lett.*, 17(6):3607–3612, 2017.

[234] Zhizhan Qiu, Hanyan Fang, Alexandra Carvalho, AS Rodin, Yanpeng Liu, Sherman JR Tan, Mykola Telychko, Pin Lv, Jie Su, Yewu Wang, et al. Resolving the spatial structures of bound hole states in black phosphorus. *Nano Lett.*, 17(11):6935–6940, 2017.

[235] Dillon Wong, Jairo Velasco, Long Ju, Juwon Lee, Salman Kahn, Hsin-Zon Tsai, Chad Germany, Takashi Taniguchi, Kenji Watanabe, Alex Zettl, et al. Characterization and manipulation of individual defects in insulating hexagonal boron nitride using scanning tunnelling microscopy. *Nat. Nanotechnol.*, 10(11):949–953, 2015.

[236] Rafik Addou, Luigi Colombo, and Robert M Wallace. Surface defects on natural MoS_2. *ACS Appl. Mater. Interfaces*, 7(22):11921–11929, 2015.

[237] Ava Khosravi, Rafik Addou, Massimo Catalano, Jiyoung Kim, and Robert M Wallace. High-κ dielectric on ReS_2: In-situ thermal versus plasma-enhanced atomic layer deposition of Al_2O_3. *Materials*, 12(7):1056, 2019.

[238] Takeshi Fujita, Yoshikazu Ito, Yongwen Tan, Hisato Yamaguchi, Daisuke Hojo, Akihiko Hirata, Damien Voiry, Manish Chhowalla, and Mingwei Chen. Chemically exfoliated ReS_2 nanosheets. *Nanoscale*, 6(21):12458–12462, 2014.

[239] JA Kruse. Methanol poisoning. *Intensive Care Med.*, 18(7):391–397, 1992.

[240] Anjali A Athawale, SV Bhagwat, and Prachi P Katre. Nanocomposite of Pd–polyaniline as a selective methanol sensor. *Sens. Actuators B Chem.*, 114(1):263–267, 2006.

[241] D Acharyya, KY Huang, PP Chattopadhyay, MS Ho, H-J Fecht, and P Bhattacharyya. Hybrid 3d structures of ZnO nanoflowers and PdO nanoparticles as a highly selective methanol sensor. *Analyst*, 141(10):2977–2989, 2016.

[242] Qian Rong, Yumin Zhang, Chao Wang, Zhongqi Zhu, Jin Zhang, and Qingju Liu. A high selective methanol gas sensor based on molecular imprinted Ag-$LaFeO_3$ fibers. *Sci. Rep.*, 7(1):1–10, 2017.

[243] Cosimo Anichini, Włodzimierz Czepa, Dawid Pakulski, Alessandro Aliprandi, Artur Ciesielski, and Paolo Samorì. Chemical sensing with 2D materials. *Chem. Soc. Rev.*, 47(13):4860–4908, 2018.

[244] Cecilia A Zito, Tarcísio M Perfecto, and Diogo P Volanti. Impact of reduced graphene oxide on the ethanol sensing performance of hollow SnO_2 nanoparticles under humid atmosphere. *Sens. and Actuators B Chem.*, 244:466–474, 2017.

[245] Katesara Phasuksom, Walaiporn Prissanaroon-Ouajai, and Anuvat Sirivat. A highly responsive methanol sensor based on graphene oxide/polyindole composites. *RSC Adv.*, 10(26):15206–15220, 2020.

[246] Wenjing Yuan, Anran Liu, Liang Huang, Chun Li, and Gaoquan Shi. High-performance NO_2 sensors based on chemically modified graphene. *Adv. Mater.*, 25(5):766–771, 2013.

[247] Jian Sun, Manoharan Muruganathan, and Hiroshi Mizuta. Room temperature detection of individual molecular physisorption using suspended bilayer graphene. *Sci. Adv.*, 2(4):e1501518, 2016.

[248] TO Wehling, KS Novoselov, SV Morozov, EE Vdovin, MI Katsnelson, AK Geim, and AI Lichtenstein. Molecular doping of graphene. *Nano Lett.*, 8(1):173–177, 2008.

[249] Fazel Yavari, Eduardo Castillo, Hemtej Gullapalli, Pulickel M Ajayan, and Nikhil Koratkar. High sensitivity detection of NO_2 and NH_3 in air using chemical vapor deposition grown graphene. *Appl. Phys. Lett.*, 100(20):203120, 2012.

[250] V Nagarajan and R Chandiramouli. Interaction of alcohols on monolayer stanane nanosheet: a first-principles investigation. *Appl. Surf. Sci.*, 419:9–15, 2017.

[251] V Nagarajan and R Chandiramouli. Adsorption behavior of NH_3 and NO_2 molecules on stanene and stanane nanosheets–a density functional theory study. *Chem. Phys. Lett.*, 695:162–169, 2018.

[252] Branimir Radisavljevic, Aleksandra Radenovic, Jacopo Brivio, Valentina Giacometti, and Andras Kis. Single-layer MoS_2 transistors. *Nat. Nanotechnol.*, 6(3):147, 2011.

[253] V Nagarajan and R Chandiramouli. $MoSe_2$ nanosheets for detection of methanol and ethanol vapors: a DFT study. *J. Mol. Graph. Model*, 81:97–105, 2018.

[254] Yeonhoo Kim, Ki Chang Kwon, Sungwoo Kang, Changyeon Kim, Tae Hoon Kim, Seung-Pyo Hong, Seo Yun Park, Jun Min Suh, Min-Ju Choi, Seungwu Han, et al. Two-dimensional NbS_2 gas sensors for selective and reversible NO_2 detection at room temperature. *ACS Sens.*, 4(9):2395–2402, 2019.

[255] V Nagarajan and R Chandiramouli. Sensing properties of monolayer borophane nanosheet towards alcohol vapors: a first-principles study. *J. Mol. Graph. Model*, 73:208–216, 2017.

[256] Cansu Akyol, Mehmet Baskurt, and Hasan Sahin. Novel ultra-thin two-dimensional structures of strontium chloride. *J. Mater. Chem. C*, 8(36):12527–12532, 2020.

[257] King Cheong Lam, Bolong Huang, and San-Qiang Shi. Room-temperature methane gas sensing properties based on in situ reduced graphene oxide incorporated with tin dioxide. *J. Mater. Chem. A*, 5(22):11131–11142, 2017.

[258] Yeon Hoo Kim, Ji Soo Park, You-Rim Choi, Seo Yun Park, Seon Yong Lee, Woonbae Sohn, Young-Seok Shim, Jong-Heun Lee, Chong Rae Park, Yong Seok Choi, et al. Chemically fluorinated graphene oxide for room temperature ammonia detection at ppb levels. *J. Mater. Chem. A*, 5(36):19116–19125, 2017.

[259] Miao Zhou, Yun-Hao Lu, Yong-Qing Cai, Chun Zhang, and Yuan-Ping Feng. Adsorption of gas molecules on transition metal embedded graphene: a search for high-performance graphene-based catalysts and gas sensors. *Nanotechnology*, 22(38):385502, 2011.

[260] Nuala M Caffrey, Rickard Armiento, Rositsa Yakimova, and Igor A Abrikosov. Changes in work function due to NO_2 adsorption on monolayer and bilayer epitaxial graphene on SiC (0001). *Phys. Rev. B*, 94(20):205411, 2016.

[261] Geonyeop Lee, Gwangseok Yang, Ara Cho, Jeong Woo Han, and Jihyun Kim. Defect-

engineered graphene chemical sensors with ultrahigh sensitivity. *Phys. Chem. Chem. Phys.*, 18(21):14198–14204, 2016.

[262] QG Jiang, ZM Ao, WT Zheng, S Li, and Q Jiang. Enhanced hydrogen sensing properties of graphene by introducing a mono-atom-vacancy. *Phys. Chem. Chem. Phys.*, 15(48):21016–21022, 2013.

[263] Poya Yasaei, Bijandra Kumar, Reza Hantehzadeh, Morteza Kayyalha, Artem Baskin, Nikita Repnin, Canhui Wang, Robert F Klie, Yong P Chen, Petr Král, et al. Chemical sensing with switchable transport channels in graphene grain boundaries. *Nat. Commun.*, 5(1):1–8, 2014.

[264] Delwin Perera and Jochen Rohrer. Structure sensitivity of electronic transport across graphene grain boundaries. *Phys. Rev. B*, 98(15):155432, 2018.